University of Louisville

ThinkIR: The University of Louisville's Institutional Repository

12-2021

Development and applications of in-vitro and in-silico models of the cardiovascular system to study the effects of mechanical circulatory support.

Moustafa Meki
University of Louisville

Follow this and additional works at: https://ir.library.louisville.edu/etd

Part of the Biomedical Devices and Instrumentation Commons, and the Molecular, Cellular, and Tissue Engineering Commons

DEVELOPMENT AND APPLICATIONS OF IN-VITRO AND IN-SILICO MODELS

OF THE CARDIOVASCULAR SYSTEM TO STUDY THE EFFECTS OF

MECHANICAL CIRCULATORY SUPPORT

By

Moustafa Meki

B.Sc., Alexandria University, 2014

A Dissertation

Submitted to the Graduate School,

the University of Louisville, In Partial

Fulfillment of the Requirements For the

Degree of

Doctor of Philosophy

in Interdisciplinary Studies, Specialization in Translational Bioengineering

Interdisciplinary Studies

University of Louisville

Louisville, KY

December 2021

DEVELOPMENT AND APPLICATIONS OF IN-VITRO AND IN-SILICO MODELS

OF THE CARDIOVASCULAR SYSTEM TO STUDY THE EFFECTS OF

MECHANICAL CIRCULATORY SUPPORT

By

Moustafa Hassan Meki

B.Sc. Alexandria University

A Dissertation Approved on

11/15/2021

By the following Dissertation Committee:

_____
Dr. Guruprasad Giridharan, Director

_____
Dr. Tamer Mohamed

_____
Dr. Thomas Roussel

_____
Dr. Stuart Williams

_____
Dr. Ayman El-Baz

DEDICATION

This dissertation is dedicated to my parents

my mother Hanaa Elabsy

and

my father Hassen Maky,

who have sacrificed everything for me.

ACKNOWLEDGMENTS

ABSTRACT

DEVELOPMENT AND APPLICATIONS OF IN-VITRO AND IN-SILICO MODELS

OF THE CARDIOVASCULAR SYSTEM TO STUDY THE EFFECTS OF

MECHANICAL CIRCULATORY SUPPORT

Moustafa H. Meki

November 15, 2021

Cardiovascular diseases (CVDs) are the leading cause of mortality globally. With ongoing interest in CVDs treatment, preclinical models for drug/therapeutic development that allow for fast iterative research are needed. Owing to the inherent complexity of the cardiovascular system, current in-vitro models of the cardiovascular system fail to replicate many of the physiological aspects of the cardiovascular system. In this dissertation, the main concern is with heart failure (HF). In advanced HF, patients may receive Left Ventricular Assist Devices (LVADs) as a bridge to transplant or destination therapy. However, LVADs have many limitations, including inability to adapt to varying tissue demand conditions, risk of ventricular suction, and diminished arterial pulsatility. To address these issues, this dissertation aims to use and develop computer, cellular, and tissue models of the cardiovascular system. 1) Use an *in-silico* model of the cardiovascular system to develop a novel control algorithm for LVADs. The control system was rigorously tested and showed adequate perfusion during rest and exercise,

protect against ventricular suction under reduced heart preload, and augment arterial pulsatility through pulse modulation without requiring sensor implantation or model-based estimations.

2) While pulsatility augmentation was feasible through the developed control algorithm, the pulse waveform that could normalize the vascular phenotype is unknown. To address this, an endothelial cell-smooth muscle cell microfluidic coculture model was developed to recreate the physiological mechanical stimulants in the vascular wall. The results demonstrated different effects of pulsatile shear stress and stretch on endothelial cells and may indicate that a pulse pressure of at least 30 mmHg is needed to maintain normal endothelial morphology.

3) In order to study the effects of mechanical unloading on the native ventricle, a novel cardiac tissue culture model (CTCM) was developed. CTCM provided physiological electromechanical and humoral stimulation with 25% preload stretch and thyroid and glucocorticoid treatment maintained the cardiac phenotype for 12 days. The device was thoroughly characterized and tested. Results demonstrated improved viability, energy utilization, fibrotic remodeling, and structural integrity compared to available culture systems. The system was also used to reproduce ventricular volume-overload and the results demonstrated hypertrophic and fibrotic remodeling, typical of volume-overload pathology.

TABLE OF CONTENTS

LIST OF TABLES

LIST OF FIGURES

CHAPTER 1: INTRODUCTION[1]

The cardiovascular system is composed of three main components: 1) the heart, 2) the blood vessels, and 3) the blood. Blood is circulated by the heart through the lungs and carries dissolved oxygen and nutrients through the arterial circulation to the whole body via a vast network of micro capillary circulation. At the tissue level, oxygen and nutrients are delivered to the tissue, while carbon dioxide and metabolic waste are removed and circulated d back to the lung through the venous circulation.

1.1 Heart Function and Cellular Organization

1.1.1 Gross Anatomy of the Heart

The heart serves as a pump to circulate blood throughout the body and provide oxygenated, nutrient-rich blood to the tissue. A schematic view of the heart structure is shown in *Figure 1-1-A.* Anatomically, the heart is composed of two pumps: a right heart that pumps blood through the lungs, and a left heart that pumps blood through the peripheral organs. Each of the two pumps is composed an atrium and a ventricle. The right atrium receives deoxygenated blood from the venous circulation through the vena cavae and passes it to the right ventricle through the tricuspid valve. The right ventricle pumps the blood across the pulmonary valve to the pulmonary arteries and into the

---

pulmonary circulation where gas exchange takes place. Oxygenated blood is drawn into the left atrium through pulmonary veins and passed through the mitral valve to the left ventricle. The left ventricle pumps oxygen-rich blood to the systemic circulation to all the end organs. As shown in *Figure 1-1-A*, the right ventricular wall is thinner than the left ventricular wall. This is because the hydraulic vascular resistance of the pulmonary circulation is folds less than the systemic circulation, and therefore cardiomyocyte size (active contractile cells of the myocardium) is on average less than the right ventricle than the left ventricle. [2]

1.1.2   Cellular Organization of the heart

The heart is composed of three types of cardiac muscles: atrial muscle, ventricular muscle, and electrical excitatory and conductive muscle fibers. Like skeletal muscles, the myocardium is striated and contracts using myofibrils containing actin and myosin filaments that will slide over each other in response to electrical stimulation [3]. Unlike skeletal muscles, however, cardiac muscles have intercalated disks that separate each cardiomyocyte from one another. The intercalated disks are fusion points for the cell membrane to allow for ion diffusion from one cell to the other. At each intercalated disk, the cell membranes fuse. This allows action potentials to freely travel from one cardiomyocyte to the other in syncytium through a latticework of interconnections as show in *Figure 1-1-B*. Therefore, functionally, ions can move easily in the intracellular fluid along the longitudinal axis of the cardiac muscle fibers and from one cardiomyocyte to the next. That being said, there are two syncytia in the heart: 1) the atrial syncytium which includes the left and right atrial walls, and 2) the ventricular syncytium which

includes the left and right ventricular walls. The two syncytia can only communicate through a conductive path of specialized cells, A-V bundle.

Structurally, the ventricular wall is composed of three layers, as shown in *Figure 1-1-C*: 1) A fibrous outer pericardium, 2) Contractile myocardium and 3) inner layer endocardium. Endocardium consists of loose connective tissue and epithelium [2, 4] and is similar in structure to the endothelium. The majority of the myocardium is composed of cardiomyocyte that are responsible for the heart contraction. The epicardium is composed of fatty and connective tissue that helps aid the heart structurally as well as produce a lubricating fluid into the pericardial cavity. [2]
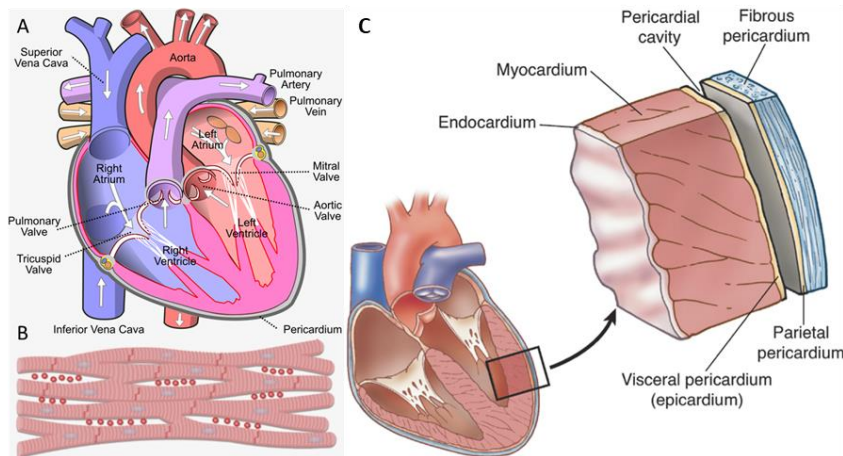
Figure 1-1 A- Gross anatomy of the heart: The heart is composed of 4 chambers. The left ventricle pumps oxygenated blood from the lungs to various organs. The right ventricle pumps blood from the venous circulation to the lungs, B- representative image of myocardial tissue, showing the latticework structure of cardiomyocytes with intercalated disks as darker lines, C- The ventricular wall is composed of three layers. The middle myocardial layer contains the contractile cardiomyocytes that will actively contract and pump blood in the body.

1.1.3 The Cardiac Cycle

Each cycle is initiated by the generation of an action potential from the sinus node. The sinus node is located in the upper portion of the right atrium. The action potential travels through the atria and to the A-V bundle into the ventricles after a brief $100\ ms$ delay. This delay allows the atrial contraction to occur briefly before the ventricular contraction which permits enough time for the atrium to act as a priming pump to fill the ventricles. As shown in *Figure 1-2*, the heart cycle consists of a ventricular relaxation period where the ventricles are relaxing and being filled with blood while the atria are contracting to boost the blood flow into the ventricle (ventricular diastole). This period is followed by a contraction phase where the right and left ventricles contract to eject blood through the pulmonary and aortic valves respectively and the atria are relaxing (ventricular systole). Ventricular contraction can be divided into two portions: an isovolumetric contraction phase where the ventricular pressure rises rapidly with no change in volume, and an active contraction phase where the pulmonary and aortic valves open, and blood is ejected. Similarly, during ventricular relaxation there is a duration where the ventricular pressure is falls rapidly with no change in volume, followed by a period where the mitral and tricuspid valves open, and blood fills the ventricles. While the cardiac cycle can change significantly during different physical conditions, the systolic duration accounts for ~40% of the cardiac cycle while the diastolic duration represents ~60% . [5] The pulmonary and aortic valves are differential pressure operated. This means that when the aortic/ pulmonary artery pressure is lower than the ventricular

4

pressure, the valves open and will remain closed otherwise. The normal arterial pressure peak is ~120 mmHg, and the lowest pressure during diastole is ~80 mmHg.
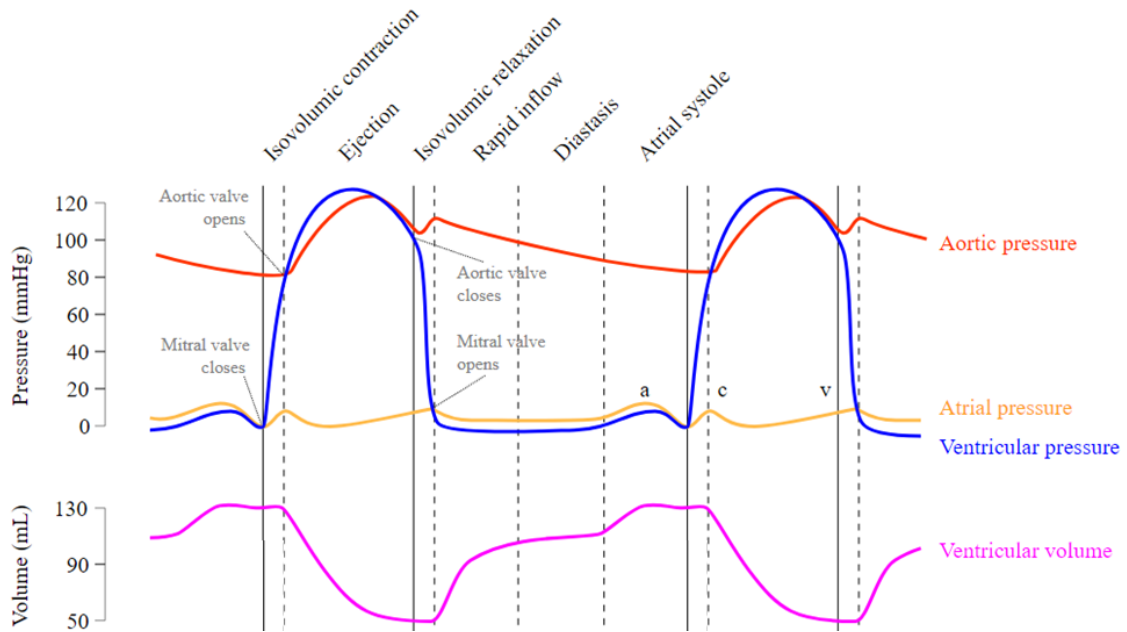
Figure 1-2 Wiggers diagram showing the ventricular volume, ventricular, atrial, and arterial pressures as function of time. Adapted from Wikimedia Commons: Wiggers Diagram.svg.

Hemodynamic loading is very important in the regulation of cardiac morphogenesis. The heart experiences two types of loads: preload and afterload. Preload refers to the initial stretching of the myocardium prior to contraction. Therefore, preload is related to the sarcomere length. The degree of stretch that is experienced by the tissue depends on the amount of blood that is being returned to the heart from the venous system, known as venous return. [6] When venous return to the heart increases, the pressure at the end of diastole also increases and the sarcomere is stretched which is increases preload. In contrast, a decrease in blood volume due to blood loss leads to decreased venous return

and decreased preload. Heart stroke volume and cardiac output are closely related to preload through the Frank-Starling mechanism which states that an increase in preload will lead to an increased stroke volume and a decrease in preload will lead to a decrease in stroke volume. [6, 7] Afterload is thought of as the load that the heart has to overcome to eject blood. Thus, it can also be thought of in terms of the ventricular wall stress. Afterload is ultimately dependent on the aortic pressure. In a simplified spherical representation of the ventricle (*Figure 1-3*), Wall stress can be expressed as

$$\sigma_\theta = \frac{p_i a^2 - p_o b^2}{b^2 - a^2} \tag{1}$$

Where σ_θ is the average wall stress, p_i is the ventricular pressure, p_o is the pericardial pressure, $a,$ and b are the inner and outer ventricular diameters, respectively. From equitation 1 it is easy to see that the maximum wall stress happens when p_i is at a maximum. It should also be noted that any enlargement in the heart that increases the heart radius will increase myocardial wall stress to the second power.

Under increased afterload, the myocardium will respond by increasing contractile protein as well as RNA and DNA synthesis. [8] Indeed, the mechanical cues in the native heart play an essential role in steering physiological or pathological remodeling such as dilated or hypertrophic cardiomyopathy. [9] *In-vitro* studies using cardiomyocytes in culture have shown the importance of mechanical stimuli to maintain and promote phenotypic characteristic of mature cardiomyocytes. [10, 11] During heart development, the heart is very responsive to mechanical cues, and it will not develop properly if blood flow is absent. Hence, any alterations to the normal hemodynamics stresses experienced

by the developing tissue will result in cardiac malformations and congenital heart defects.
[12, 13]
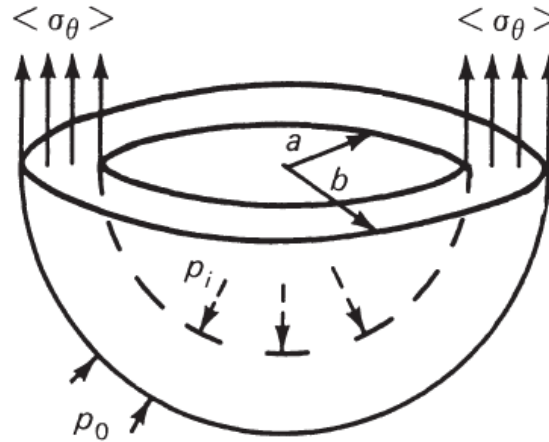
Figure 1-3 Simplified model of the ventricular wall as a thick-walled sphere. Balance of pressure forces shows the dependence of afterload and wall stress on ventricular diameter and pressure.

1.2 Vascular Function and Cellular Organization

1.2.1 Anatomy of the Vasculature

The vasculature consists of arteries, arterioles, capillaries, venules, and veins. Any cell in the body is on average 40 μm away from a capillary and all tissue is fully infused with an intricate network of capillaries. Typically, the human body contains ~5 liters of blood .[14] The vascular system can be divided into two parts: the pulmonary circulation and the systemic circulation. The pulmonary circulation loops from the right heart, through the lungs, and back into the left heart. The systemic circulation loops from the left heart, through the entire body and back to the right heart. Generally, for both circulations blood is supplied by the heart to large arteries which branch into smaller arteries and end with arterioles and capillaries. The capillary bed gradually joins together

to form larger veins to return blood to the heart. For humans, the aorta which is the largest blood vessel varies between 2.5 cm to 3.4 cm in diameter. [15] The vascular system must fulfill three primary functions [16]: 1) Enable efficient mass transfer to the tissue. This function is readily achieved by the capillaries which are a monolayer of endothelial cells (ECs) and have an enormous surface area ~ 300 m^2, 2) regulate blood distribution in response to metabolic needs of the perfused tissue. The majority of the hydraulic resistance of the vasculature is generated through the arterioles and capillaries. Smooth muscles that surround the inner endothelial wall of the blood vessels will relax and contract in response to neural or humoral stimuli. Thus, blood flow can be directed to areas where it is needed and away from where it is not. 3) Maintain a blood reservoir. The veins contain almost two thirds of the blood content of an adult human. This is important in case of blood loss, so the body does not immediately go into hemorrhagic shock.

1.2.2 Arterial Wall Structure

The wall of the artery consists of three layers, as shown in *Figure 1-4-A*. The innermost layer is called tunica intima which consists of a monolayer of endothelial cells and a basal membrane. The basal membrane contains type IV collagen, fibronectin, and laminin. Tunica media consists of Smooth Muscle cells (SMCs) and is separated from the intima by thin elastin layer. The outermost layer is known as tunica adventitia and is composed of loose connective tissue containing type I collagen, fibroblasts, and a lower amount of elastin fibers. The vascular smooth muscles are circumferentially oriented and play an important role in regulating the vascular tone and arterial stiffness.
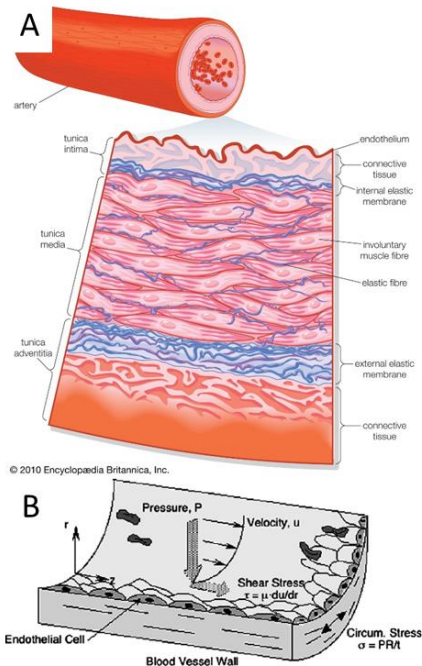
Figure 1-4 **A** Typical anatomical structure of the artery. The figure shows three layers: tunica intima, tunica media, and tunica adventitia, source: Encyclopædia Britannica , **B-**Inner endothelial wall is in contact with the blood flow and is the first responder to the mechanical cues within the vessel lumen including, hydraulic pressure, shear stress ,and stretch, adapted from [17].

The endothelial layer on the inside is in constant contact with the inner blood flow and will thus react to the mechanical forces generated by the pulsatile flow through the vessel lumen. Endothelial cells can communicate these stimuli to promote or repress vasodilatation, inflammation, tissue remodeling, proliferation, apoptosis, or cell migration, (e.g., [18-20]). This is graphically represented in as shown in ***Figure 1-4-B.*** However, the components of the vascular wall vary drastically along the vascular tree. While the large arteries have a thick media with obvious multi smooth muscle layers, the veins have a much thinner media, while the capillaries are only composed of an

endothelial monolayer. This can be understood by noting at the mean blood pressure

along the vascular tree. As shown in *Figure 1-5*, The mean pressure is ~ 100mmHg at

the aorta with a 40mmHg pulse pressure ($P_{systolic} - P_{diastolic}$). However, as the blood

flows through the systemic circulation, the pulse pressure is greatly reduced (almost 0

mmHg at the capillaries) and the mean pressure is also reduced, especially across the

arterioles. The high blood pressure in the large arteries require the vessel wall to be

structurally stronger, with a higher expression of elastin fibers and smooth muscle layer

thickness compared to small arteries and arterioles.
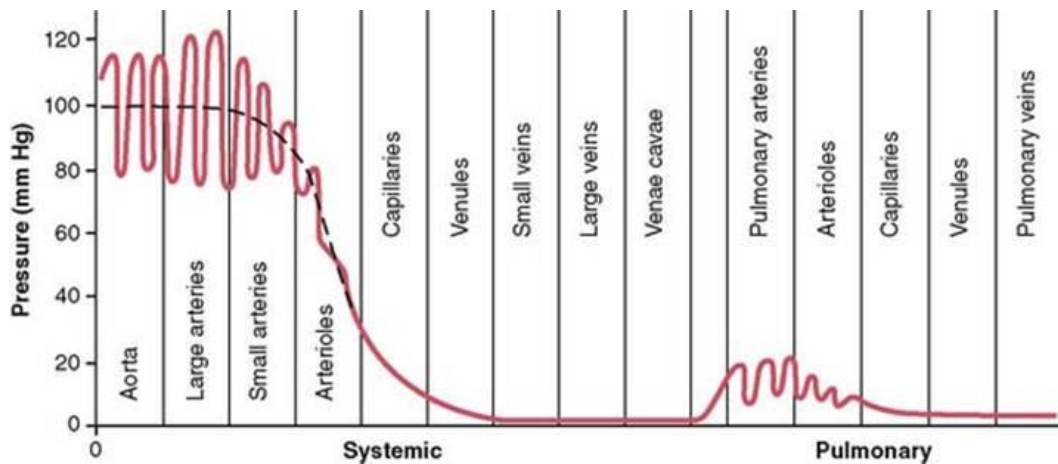
Figure 1-5 Changes in blood pressure and pulsatility along the vascular tree. The mean

pressure and pulse pressure are the highest at the aorta and values drop as blood moves

along the branches, adapted from [2]

1.2.3   Regulation and function of ECs and SMCs in the vascular wall

ECs form a continuous barrier between blood and tissue. In addition to allowing diffusion

of biological substrates, ECs work as a non-thrombogenic surface, and can regulate

leukocyte entry into tissue. Healthy endothelium secretes tissue factor pathway inhibitor

and expresses anticoagulant proteins on their cell membrane such as heparin sulfate and

ADPase, thereby inhibit platelet deposition and blood clots formation. [21] Importantly, ECs have been shown to respond to shear stresses induced by blood flow. Physiological levels of shear stresses cause ECs to align in flow direction, inhibit angiogenesis, and reduce inflammatory response markers. [22] In contrast, low levels of shear stress have been shown to induce vasoconstriction, cellular misalignment, and expression of proinflammatory and oxidative stress genes. [22, 23]

SMCs are in a quiescent state in the adult blood vessels and express high level of contractile protein to regulate the vascular tone. However, SMCs can shift to a proliferative phenotype in response to injury or in culture, where they release growth factors that stimulation of SMC migration, growth, and ECM synthesis. [24] SMCs have been shown to respond to cyclic stretch that is associated with pulsatile flow domains. [25]SMCs regulate the diameter of arterioles and small arteries in response to blood pressure changes, and any increase in blood pressure above normal level will stretch SMCs and induce the contraction of SMCs to maintain the vessel diameter within a narrow range. This response is largely communicated through the stretch signal and ECs secretion in response to shear stress changes[26]

1.3   Modeling of the cardiovascular system

Various models of the cardiovascular system have been developed at different degrees of complexities. The choice of the appropriate model is solely up to the research question at hand. These models can provide critical guidance in preclinical and translational research and may be limited to certain parts of the cardiovascular system (e.g, heart tissue or cardiomyocyte) or may model the entirety of the cardiovascular system as in hemodynamical modeling. Such models can include animal, cellular, tissue, and

computer models. Herein, hemodynamical modeling, vascular modelling, and heart modeling are reviewed.

1.3.1 Hemodynamical Modeling of the Cardiovascular System

In order to better understand the cardiovascular system, the use of mathematical models and numerical simulations has proven to be a powerful tool in understanding the mechanisms that mediate its function in both normal and pathological conditions. Such models vary drastically in complexity and thus the selection of the appropriate complexity depends on the aims and the accuracy necessary for the research study. [27] Linearized mathematical models of the Cardiovascular system can be broadly classified based on dimensionality into lumped parameter (zero dimensional, 0D), or distributed parameter (1D, 2D, and 3D). Lumped parameter models assume a uniform distribution of pressure, flow, and volume within each block at any time. Distributed parameters models, however, can detect the variations of these parameters in space, as illustrated in *Figure 1-6-A*. Lumped parameter models are usually based on the Windkessel model [28] which is most widely used. Here, the vascular system is lumped in to single or multiple compartments, each of which is comprised of two elements: a resistance and a compliance element. [29, 30] Other elements can be added to account for inertance or characteristic impedance, which gives rise to the three and four element Windkessel model [28, 30]. Windkessel models are attractive because of their low computational costs and ability to reproduce pulse wave propagation in time domain. [31] In distributed models, however, the pulse waveform depends on both time and space. Additionally, in multicompartment model heart valves can be incorporated to add discontinuities to the flow and simulate transient effects all while still using numerical solutions of ordinary

differential equations. An example of this is shown in *Figure 1-6-B*. [32] 1D models use simplified Navier-Stokes equation to recreate the flow pressure and velocity along the vascular tree. [33] 3D models are usually used to simulate local flow regimes in a limited area of interest. A 3D model of appropriate accuracy can capture the interaction between the flow with the vessel wall using Fluid-Structure-Interaction. Indeed, such simulations are of high complexities and cannot be used to simulate gross effects within the arterial tree and are thus limited to local hemodynamics in an area of interest.
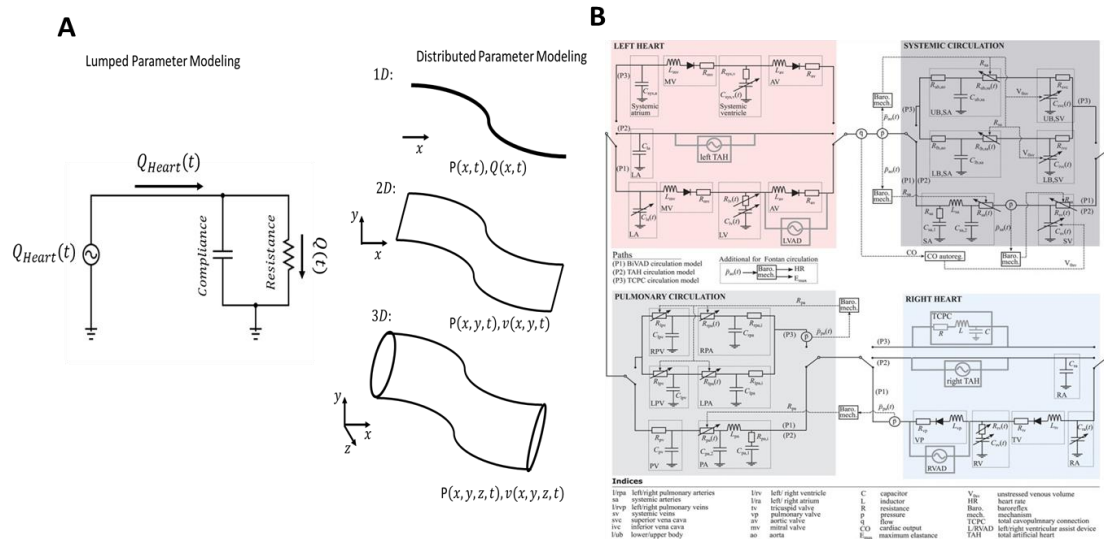
Figure 1-6, **A**- Comparison between lumped parameter models and distributed models. A Windkessel lumped parameter model represents the vascular system as two elements with a compliance and a resistance. Higher order distributed models can provide spatial description of the pressure and flow velocity, but are computationally expensive, **B**- Adapted from [34], example of a sophisticated multicompartment lumped parameter model where different elements of the pulmonary and systemic circulation are modeled.

1.3.2 *In-vitro* modeling of vascular physiology

Over the past decade, cell culture technology and microfluidics have advanced

significantly and have thus enabled the development of culture systems that can more

accurately represent the native *in-vivo* physiology. [35] In cardiovascular research, such

systems are highly desirable due to the innate complexity of cardiovascular diseases and

the subsequent difficulty in studying drugs that target both key risk factors and the

manifestations of cardiovascular diseases.[35] Several cellular models have been

developed to model the vascular physiology and pathophysiology. These models have

mainly incorporated endothelial cells (ECs) and to a lower extent smooth muscle cell

(SMCs), being the major cellular components of arteries and veins.

1.3.2.1 Advancements in vascular modeling

Recent advancements in microfluidics and organ-on-a-chip research have brought 3-D

cultures of primary human cells to create biomimetic models of organs and tissue. Such

models incorporate many of the physiological phenomenon of the native organ and

tissue. Most microfluidic devices for vascular modeling are fabricated using poly-

dimethylsiloxane (PDMS) to create structures and channels using soft lithography from a

mold or template. The small dimensions (<1 mm) of these microchannels ensure a

laminar flow regime throughout the model. Fluid mechanics of laminar, low Reynold's

number (Re) flows are well defined and understood which allows for precisely modulated

flow environments as well as high resolution complex geometries. Moreover, the small

footprint of microfluidic devices allows for high throughput experimentation.

Microfluidic devices have been used to study the hemodynamics of the large arteries. [36,

37] More involved systems were developed to study the microcirculation and was able to

reproduce red blood cell (RBC) deformation at the capillary level. [38]Other groups have also developed microchannel systems to study the effects of shear stress on the endothelial phenotype. [39-41]

1.3.2.2   Current state of EC-SMC co-cultures to model vascular wall

As previously discussed, the interaction between ECs and SMCs in-vivo are vast and several co-culture models of ECs and SMCs have been used to model the normal [42] and diseased vessel wall. [43] ECs and SMCs can be co-cultured in 3 variations, as shown in *Figure 1-7* [35] 1) ECs and SMCs on opposite sides of a membrane[44-46], 2) ECs are cultured on gels with embedded SMCs (e.g., collagen containing SMCs) [47, 48], and 3) ECs are directly cultured above SMCs [49, 50]

The advantage of having a porous membrane to separate the two cell types is to permit the easy separation of the two cell lines for further analysis and limit overgrowth. However, the introduction of a stiff synthetic substrate, much stiffer than *in-vivo,* can also greatly affect the SMCs proliferation and upregulate VEGF,PDGF and TGF-B1 expression in culture. [[[40,54]]] Indeed, the coculture of ECs and SMCs together in the presence of a porous membrane promoted a more physiological, elongated EC phenotype in contrast to the more polygonal ECs morphology seen with ECs alone in *in-vitro* cultures. [47] Additionally, the presence of SMCs promoted EC expression of TF, VEGF, and adhesion molecules [44, 51, 52]

The separation ECs and SMCs when they are directly cocultured is laborious and can be achieved using coated magnetic beads, specific to one of the cell lines (usually ECs) [53]

The closeness of ECs and SMCs in direct co-culture increases contact and decreases the diffusion distance. This has been shown to promote physiological ECM synthesis and protein expression. [54] In the absence of SMCs, ECs will rapidly migrate into collagen and fibrin gels. However, the presence of SMCs inhibits EC proliferation, allowing such cultures to be stable for longer. The use of collagen gels containing SMCs instead of directly culturing layers of ECs and SMCs together has been used to better mimic the *in-vivo* intima. This is needed because although ECs can produce several basal proteins such as collagen II and IV, there has not been much success in creating a well-formed intima *in-vitro*. [55, 56] Nonetheless, direct cocultures methods can best mimic the physiological structure of the vessel wall and use fewer cells than other types of culture.
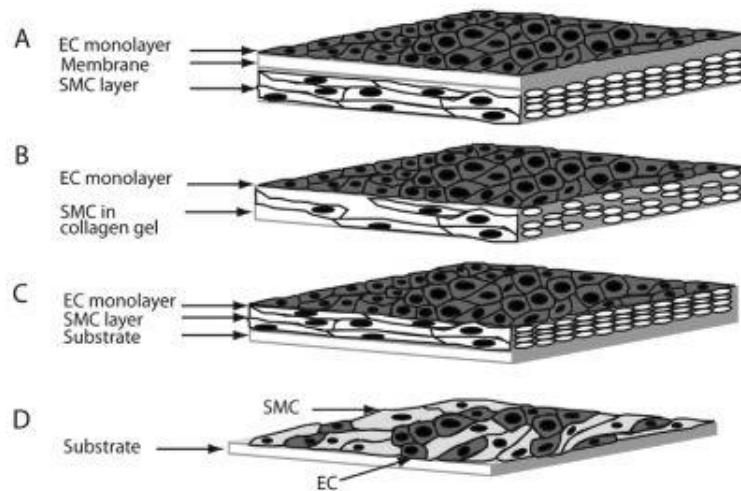
Figure 1-7 Schematic representation of different variations of EC-SMC cocultures arrangements from literature. (A) ECs and SMCs are cultured on both sides of a porous membrane to facilitate cell separation. B) ECs are cultured on top of SMCs embedded in a collagen matrix, C) ECs are directly cultured on top of SMCs similar to physiology, and D) A mixed culture of ECs and SMCs. Figure adapted from [35]

1.3.3 *In-vitro* cellular modeling of cardiac physiology

Before clinical studies, there is a need for reliable experimental systems that can accurately replicate the human heart's physiological environment. Such systems should model altered mechanical loading, heart rate, and electrophysiological properties. The most prevalently used cardiac physiology screening platform are animal models and those have limited reliability in mirroring the effects of drugs in human hearts [57, 58]. Additionally, the use of animal models to create a pharmacokinetic profile of drugs is relatively expensive at the early development stage since large amounts of the drugs are used [59]. Ultimately, the ideal cardiac model is one that demonstrates high sensitivity and specificity towards various therapeutic and pharmacological interventions while accurately replicating the physiology and pathophysiology of the human heart [60].

1.3.3.1 *In-vitro* modeling of the human myocardium

In-vitro systems using a controlled culture environment have the unique advantage of quantitatively characterizing drug-related changes at the cellular level with relatively lower cost. These systems' success depends on how much clinically relevant information can be detected through them. This includes contractility measurements, protein expression (e.g., gap junction proteins and contractile proteins), accurate transcriptional profile, calcium homeostasis, and electrophysiology. Additionally, the applicability of the system to human cells is of paramount importance. Guth et al. [59] summarized the most relevant features and considerations for *in-vivo* drug testing platforms. Nonetheless, 28% of drug withdrawals are owed to unanticipated cardiotoxicity [61]. This only shows that current cardiac models are unsuitable for

preclinical drug testing and development. To this end, there have been many efforts to develop reliable preclinical models to mimic the human heart tissue.

Thin heart slices are a relatively new technology that has emerged in recent years and has shown promise in providing a system of adequate complexity and viability to allow for drug screening [62]. They retain the adult phenotype, including the adult heart's multicellularity and extracellular structure, and have been produced from human cardiac tissue and large mammals.

While each *in-vitro* model has its advantages, each model has shortcomings in modeling the physiology/pathophysiology of an adult human heart. This is owed to the heart tissue's complex environment where multiple cell types interact under chronic neurohormonal stimulation to maintain normal heart homeostasis. It is thus understandable that there are many challenges in reproducing this complexity in culture.

Historically, there are a few *in-vitro* models that have been instrumental in our cellular level understanding of the cardiac system: 1) Isolated adult cardiomyocytes, 2) human-induced pluripotent stem cell derived cardiomyocytes (hiPSC-CMs), and 3) arterially perfused ventricular wedge preparations. We describe each of these systems herein and introduce their advantages and disadvantages compared to heart slice preparations.

1.3.3.2   Animal/Human isolated adult cardiomyocyte

One of the oldest and simplest cardiac models is the use of isolated human cardiomyocytes. The first isolated cardiomyocyte from adult hearts failed to last for a reasonable time in culture and lacked proper phenotypic characteristics [63-65].

Successful isolation and culture of adult cardiomyocytes were performed first by Powell and Twist in 1976 [66]. Since then, cultured adult isolated cardiomyocytes have been primarily used to study cardiac electrophysiology [67, 68], response to sepsis [69], Ca^{+2} dynamics [70, 71], gene transfer [72] , and contractile function [73, 74]. Indeed, the simplistic unicellularity of isolated primary cardiomyocytes provides experimental strength by avoiding extraneous influences from other tissue components [75]. Moreover, when cultured adhering to a coated plastic surface, they will retain many adult cardiomyocyte phenotype characteristics including cell-cell coupling, T-tubule organization, and rod-shaped morphology [76]. While having been instrumental to cellular level research, adult isolated cardiomyocytes' appropriateness for predicting cardiotoxicity and macrolevel response to drugs and therapies is restricted. Although isolated cardiomyocytes can survive for weeks, the single cell-type culture will rapidly dedifferentiate and lose function within 48 hours of culture [77]. Additionally, the low cell yield with currently used enzymatic isolation protocols and cellular damage limit their use in high throughput screening [78-80]. Adult isolated primary cardiomyocytes may be unsuitable for long-term drug screening due to their limited life span in culture and its nature of replicating only a single cell type. Nevertheless, recent efforts have focused on improving isolation protocols to improve cell yield and lowered the damage to the cardiac tissue [81]. Notably, Callaghan et al. [82] have shown that Geltrex and blebbistatin using adult mouse cardiomyocytes enhanced survival in culture with maintained cellular function. However, the inhibition of cardiomyocyte contraction using blebbistatin may limit the model's use to study cardiomyocyte contractility.

1.3.3.3 Human-Induced Pluripotent Stem Cell-derived Cardiomyocytes

Human-induced pluripotent stem cells (hiPSC) reprogramming was first demonstrated in 2007 [83], and hiPSC derived cardiomyocytes (hiPSC-CMs) have since been extensively used to determine drug cardiotoxicity, arrhythmogenicity [84-86], and cardiac disease modeling [87, 88] due to the relative simplicity of hiPSC-CMs generation and culture process [89]. However, it is well known that hiPSC-CMs are structurally and functionally similar to fetal cardiomyocytes due to their lack of cell-cell coupling, under-developed sarcoplasmic reticulum, and no T-tubules; hence slow excitation-contraction coupling [89].

With these apparent limitations in mind, several efforts have been conducted to promote their maturation, discussed in detail in Ahmed et al. review [90]. These studies aim to mimic certain cardiac milieu stimuli using integrated heart-on-chip systems to include extracellular matrix [91], 3-D structure [92, 93], electrical [94, 95], and electro-mechanical stimulation [96-98]. Notably, Kroll et al., [99] developed a force stretch system that can apply synchronized mechanical stress and electrical stimulation on hiPSC-CMs cultured on a flexible PDMS membrane. They have shown enhanced N-cadherin signal, stress fiber formation, sarcomere shortening, and contractile protein expression with hiPSC-CMs conditioning, indicating a trend towards maturation, as thoroughly reviewed here. [100-103] These advancements allow the hiPS-CMs to become the most widely used platform for drug screening due to their stability in culture for a long time and their physiological resemblance to the human heart.

1.3.3.4 Animal-derived arterially perfused left ventricular wedge preparations

Arterially perfused left ventricular wedges were developed by Yan and Antzelevitch in 1996 [104, 105] using canine hearts. Since then, ventricular wedge

20

preparations have been expanded to other animal models, including humans, and have been extensively used in studying heart electrophysiology, conduction velocity, and the development of arrhythmia [106-109]. The advantage of this model is producing 3-dimensional tissue-level insight into cardiac physiology and pathophysiology.

However, where ventricular wedges fall short is the relatively low throughput of the preparation due to the coronary system's complexity and, therefore, low sample yield per heart, [110] limiting their use in drug testing. Furthermore, the preparations can only remain viable for a few hours in perfusion before suffering a similar fate to isolated cardiomyocytes [111] restricting their use in subacute and chronic studies. Such a system as a drug screening platform would be challenging due to the short life in culture and the low throughput.

1.3.3.5 Animal/human-derived heart slices to model cardiac physiology

The first thin (<400 μm) heart slices were developed in 1992 [112] in the advent of tissue slicing technology with relatively high precision and reproducible slice thicknesses. In this study, rat ventricular heart slices were cultured for 24 hours with maintained viability and metabolism [112]. The key feature was the use of continuously oxygenated media while rotating the culture within a cylinder. Brandenburger et al., [113] 10 years later developed a more simplistic approach to overcome the inadequacies with isolated cardiomyocytes and ventricular wedge preparations by using a transwell to allow for a liquid-air interface.

Thin heart tissue slices (300 μm) have since been shown to achieve high viability, retain typical tissue architecture, contractility, calcium handling, and conduction velocity

for 24 hours [111, 114]. Additionally, heart slices maintain a 3-dimensional structure with the multi cell-type environment and the presence of extracellular matrix (ECM). This allows for other cellular components in the heart slices and ECM to interact with the cardiomyocytes through direct cellular contact or paracrine secretion, which is essential to maintain a mature cardiomyocyte phenotype [115, 116]. It is important to note that heart slices and ventricular wedge preparations are different. Thin heart slices could remain viable and functional in culture for 24 hours, do not require external perfusion, and obtain oxygen and nutrients directly from culture media. These unique advantages make them adequate for medium to high throughput systems for drug discovery.

Since their inception, heart slices have been prepared from several animals as well as human hearts. Detailed protocols for preparing heart slices have been described here [113, 114, 117, 118]. While multiple factors control the maturation and regulation of the adult cardiac phenotype, the structural fidelity of heart slices provides cell-cell interactions, transmembrane regulation and maintains standard tissue stiffness. These heart slices' thinness simplifies nutrient and oxygen diffusion through the tissue and provides a "pseudo" 3-dimensional model that can allow for multiplexed cellular-level studies. Pseudo-3-dimensional model refers to the large surface area to thickness ratio of the heart tissue slices, which does not compromise the tissue's 3-D structure while maintaining proper substrate exchange.

1.3.3.6   Recent advancements in heart slices

Early transwell culture of cardiac slices by Brandenburger et al. maintained viability, ß-adrenergic response, and many electrophysiological properties for 28 days [113]. However, the prolonged culture of heart slices in transwell systems produced an

observable loss in the tissue's structural and functional integrity after 24 hours in culture shown by a >90% drop in contractility. The observed tissue remodeling reaffirmed this with a dedifferentiated cardiomyocyte phenotype and a significant reduction in mRNA expression of MLC2 and α-actin [113]. Subsequent efforts used the same transwell system to culture heart slices 24 hours using human and other vertebrate hearts [111, 114]. Indeed, the heterogeneous heart slice preparation incorporates many organotypic characteristics of the myocardium, but they will undergo dedifferentiation due to the non-physiological environment in culture [112, 113, 119].

The native heart experiences several hemodynamic and neurohormonal factors which precisely compose its ideal environment for functional integrity [9]. Disruption of this balance in culture will ultimately promote some level of adaptive remodeling within the heart. This highlights the importance of incorporating biomimetic stimulants to maintain cardiac phenotype properly. But given the cardiovascular system's complexity, it is difficult to define all the cardiac milieu constituents responsible for this balance.

In 2019, several efforts were taken to prolong the functional viability of the heart slices in culture. The most relevant factors addressed in these efforts are biophysical stimulation through electrical pacing, mechanical loading (preload and afterload), and proper oxygenation and nutrient support [110, 117, 120, 121].

Electrical impulse propagation in the heart is regulated through the gap junctions, which synchronize action potential progress and contraction [122]. The disruption of the gap junction protein connexin 43 localization, or expression can trigger arrhythmias. Continuous electrical stimulation of hiPSC-CMs has been shown to improve connexin abundance and improve sarcomere ultrastructure [123]. The other side of the coin is the

mechanical loading condition in culture. Mechanical cues in the native heart play an essential role in steering physiological/pathological remodeling such as dilated or hypertrophic cardiomyopathy [9]. The absence of electrical stimulation, preload, and afterload in static transwell culture may partially explain the loss of contractility and contractile protein expression after 24 hours in culture [113]. Furthermore, the high metabolic demand of the myocardium necessitates the incorporation of rich nutrient media. Several media supplements have been previously used to support hiPSC-CMs in culture [124-126]. Likewise, oxygenation of the media has proven crucial to prevent tissue hypoxia since the slice thickness (300-400 μm) approaches the diffusion limit of oxygen of the myocardium and can heavily impact cardiac gene expression [127].

1.3.3.7   Recent efforts in creating physiological heart slice culture

In this context there have been several efforts to emulate the cardiac milieu in culture. Watson et al. [117], investigated the application of simultaneous electrical stimulation and preload on rat, rabbit, and failing human heart slices. The system used a hand-operated screw and nut post to progressively stretch the tissue to different sarcomeric lengths and achieved sub-micrometer resolution. The study compared this system to static transwell culture and fresh tissue. Rat heart slices cultured for 24 hours with an increased sarcomeric length of 2.2 μm showed maintained contractile function, normal electrophysiology, conduction velocity, calcium handling, and action potential compared to fresh tissue. Interestingly, this model showed an upregulation of hypertrophic genes and increased calcium transient amplitude within 24 h in culture compared to fresh heart slices. At the same time, cardiomyocyte size did not vary for all preloading conditions tested. Five days culture with rabbit heart showed no deterioration

in contractile function. Heart failure slices from human hearts showed some degree of preserved contractility after 24 hours in culture.

There are obvious limitations when using slices from rat hearts since their high metabolic rates make them more susceptible to dedifferentiation. Moreover, the short culture time leaves unanswered questions regarding the long-term performance of static preload. However, the improvement in functionality with stretching heart slices underlined the undeniable mechanical stimulation role in regulating the cardiac phenotype *in-vitro*. Additionally, the upregulation seen in some hypertrophic genes may be related to the isometric contraction of the tissue slices with theoretically infinite afterload. [128]

A reasonably similar system was developed by Fischer et al. [121] In this system, slices from normal and failing human hearts were stretched between two posts in culture with electrical stimulation. The heart slice was fixed at one end, while the other end was connected to a spring cantilever to provide a linear mechanical afterload. A small magnet coupled with a magnetic field sensor was used to detect the movement of the free end of the tissue slice, and the contractile force was calculated in real-time using the spring constant. While using a low stimulation frequency (0.2 Hz) for up to 4 months, the study showed preserved contractility, preserved tissue elasticity, connexin localization, and α-actinin. But there is severe downregulation of cardiac gene expression at the first assessed time point (8 days). Unlike the culture system by Watson et al. [117], this system allowed for active tissue contraction and shortening. Nevertheless, as noted by Pitoulis et al. [128] this mode of contraction is still short of the physiological force-length loop where relaxation and contraction are separated by periods of isometric relaxation and

contraction. Ou et al. have shown that through optimized proprietary culture media, frequent oxygenation, and electrical stimulation, tissue slices can preserve viability, functionality, and cardiomyocyte structure for up to 6 days. [118, 120] The 300 µm human and pig heart slices were cultured at a physiological rate (1.2 Hz, 72 beats/min) and showed normal viability, gene expression profile, calcium homeostasis, contractility, twitch force generation, and response to ß-adrenergic stimulation over the first six days. However, by day 10, dedifferentiation was evident by the disruption of gene expression of more than 500 genes, connexin-43 delocalization, and loss of contractility. Nonetheless, prolonging functionality and maintaining cardiac phenotype for six days is a significant advancement compared to the early transwell culture systems. However, the critical element missing is the addition of synchronized mechanical loading of the heart tissue.

1.4   Cardiovascular Disease

The American Heart Association (AHA) annual report on Cardiovascular Disease (CVD) reports a 49.1% prevalence of CVD in the United States (126.9 million in 2018) for adults > 20 years of age. [129] Mortality due to CVD was 868,662 in 2018 and represented a $363.4 billion financial burden between 2016 and 2017. [129, 130] The term CVD encompasses a wide range of pathologies that affect both the heart and the vasculature. Heart diseases include Coronary Heart Diseases (CHD), heart valve diseases, cardiomyopathies, and Heart Failure (HF). Vascular diseases include all atherosclerotic diseases where large and medium-sized arteries are completely or partially occluded due to the buildup of cell debris and other components to form a thrombus. [131] The reduction or stop of blood flow may lead to end-organ failure or loss of limbs. It should

be noted, however, that heart and vascular diseases are closely related. For example, elevated blood pressure or hypertension can be caused by valvular as well as vascular diseases. In turn, high arterial pressure can lead to pathological adaptation and remodeling of the heart in order to cope with the high ventricular wall stress. The same can happen with other types of CVD where what starts as a valvular disease (e.g., mitral, or aortic insufficiency) or coronary blockage may lead to eventual HF.

1.4.1   Heart Failure

As discussed, the compensatory mechanisms of the body can lead to a gradual worsening of the heart's ability to efficiently pump blood throughout the circulation leading to a vicious cycle of HF, as shown in *Figure 1-8*. HF can be defined as a pathological state where a heart dysfunction diminishes the heart's ability to pump blood at a level that meets tissue and organ needs. [132, 133] Hemodynamically, HF is characterized by the accumulation of blood in the atria and the venous circulation as well as the in adequate perfusion of the end organs and kidneys, leading to water and sodium retention.

Progression of heart failure is always associated with left ventricular remodeling, which manifests as a gradual increase in left ventricular end-diastolic and end-systolic volumes, wall thinning, and a change in chamber geometry to a more spherical, less elongated shape. [134]. The subsequent heart dilation leads to increased ventricular wall stresses that in turn cause more dilation. Myocardial infarction leads to the deposit of collagen to compensate for myocardial death and subsequently causes ventricular hypertrophy. In any such process, it is usually associated with a continuous decline in ejection fraction. Additionally, sympathetic neural stimulation and the activation of the

Renin-Angiotensin-Aldosterone System (RAAS) also lead to higher fluid retention,

increased myocardial ejection load, and ultimately further exacerbation of HF. [135]

Chronic HF affects 11% of the population aged 60-80. [129] The underlying causes

for cardiomyopathies are vast and include vascular diseases, hypertension, arrhythmias,

coronary heart diseases (ischemic cardiomyopathies), hypertrophic or dilated

cardiomyopathy, and myocarditis.[136] Therefore, the optimal therapy and preventative

approaches for HF are heavily dependent on understanding the disease etiology.

Clinically, HF manifests itself by dyspnea, shortness of breath under rest or exertion,

peripheral edema, and heart rhythm irregularities. [137] HF is classified broadly

according to left ventricular ejection fraction (LVEF) in to three categories 1) HF with

preserved ejection fraction HFpEF, (LVEF > 50%), 2) HF with midrange ejection

fraction (LVEF 41%-49%), and 3) HF with reduced ejection fraction (HFrEF), (LVEF <

40%) [138] The severity of HFrEF symptoms is commonly graded based on the New

York Heart Association (NYHA). NYHA classifies HF into four subclasses as shown in

Table **1-1**. [139] The degree to which symptoms are presented directly affects the

optimal treatment option for HF patients. NYHA III and IV are considered advanced HF.
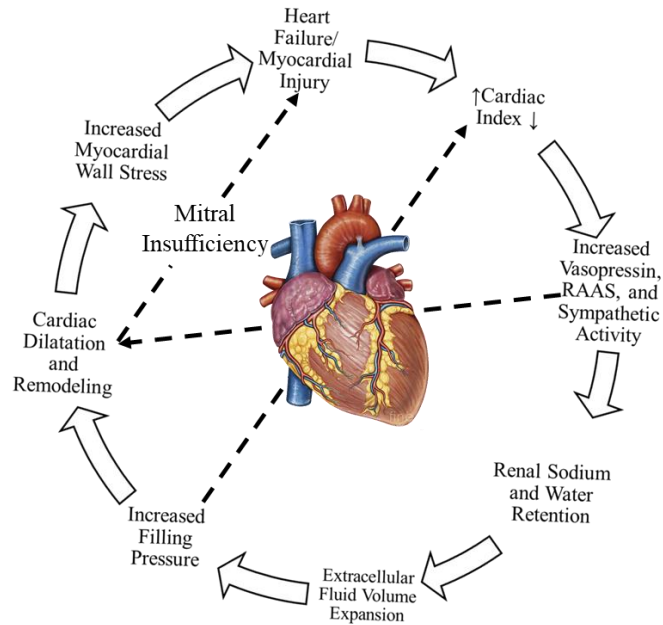
Figure 1-8 The vicious cycle of HF reproduced from. [135] Initial injury to the heart lead to decrease in cardiac index, and sodium and water retention. This leads to an increased cardiac filling pressure which leads to further dilatation and remodeling of the ventricle. Myocardial dilatation increases ventricular wall stress and remodeling which can lead to mitral insufficiency causing decreased cardiac output and deteriorated HF condition.

1.4.2   Treatment of Heart Failure

The management of HF requires extraneous changes in life habits (e.g., limiting daily fluid intake, changing traveling, dietary, and social habits), and drug therapies are usually helpful during the initial stages. Angiotensin Converting Enzyme Inhibitor (ACE-I) is the most recommended treatment for early-stage HF. Depending on patient-specific factors, they can be combined with beta-adrenergic receptor blockers, diuretics, and inotropic drugs. [13,1,2,3] In other cases, cardiac resynchronization therapy and cardioverter defibrillators are indicated for patients with reduced ventricular function showing abnormal sinus rhythm, AV-block and are not responding to pharmacological therapy.

[140] The adequacy of HF treatment is obviously depending on the stage of HF as shown in *Figure 1-9*. Advanced HF patients who no longer respond pharmaceutical management and therapies are candidates for heart transplant or mechanical circulatory support using Left Ventricular Assist Devices (LVADs) either as a bridge to transplant or a destination therapy.

NYHA Class		Clinical symptoms
I		No limitation of physical activity. Ordinary physical activity does not cause undue fatigue, palpitation, dyspnea (shortness of breath).
II		Slight limitation of physical activity. Comfortable at rest. Ordinary physical activity results in fatigue, palpitation, dyspnea (shortness of breath).
III		Marked limitation of physical activity. Comfortable at rest. Less than ordinary activity causes fatigue, palpitation, or dyspnea.
IV		Unable to carry on any physical activity without discomfort. Symptoms of heart failure at rest. If any physical activity is undertaken, discomfort increases.

Table 1-1 Clinical symptoms presented by patients suffering HF. NYHA I do not present any evidence of cardiovascular disease. There are no symptoms and limitation in ordinary physical activity. NYHA II show mild symptoms of HF and slight limitations to their day-to-day physical activity. NYHA III patients show more severe symptoms with limitations to ordinary activities due to symptoms with less-than-ordinary activity. Only comfortable at rest. NYHA IV show evidence of sever cardiovascular disease with sever limitation and experience symptoms even while at rest. NYHA III and NYHA IV are considered advanced HF and may be candidate for heart transplant or mechanical circulatory support.

1.5 Advanced Heart Failure Treatment

1.5.1 Mechanical Circulatory Support for advanced HF patients

For advanced HF patients with compromised cardiac function, heart transplantation remains the only option to improve exercise capacity and survival. [26] but it is restricted to select patients based on multiple factors including age, co-morbidities, and end-organ function [141]. Further, the number of available donor organs (~2000/year in the USA) cannot meet the growing demand (up to 30,000 per year). Mechanical circulatory support using left ventricular assist devices (LVAD) has emerged as standard clinical therapy for advanced heart failure due to the paucity of donor organs either as a bridge to transplant or destination therapy. LVADs are mechanical pumps that are implanted in patients to pump the blood from native left ventricle to the aorta to reduce ventricular workload and augment end-organ perfusion.
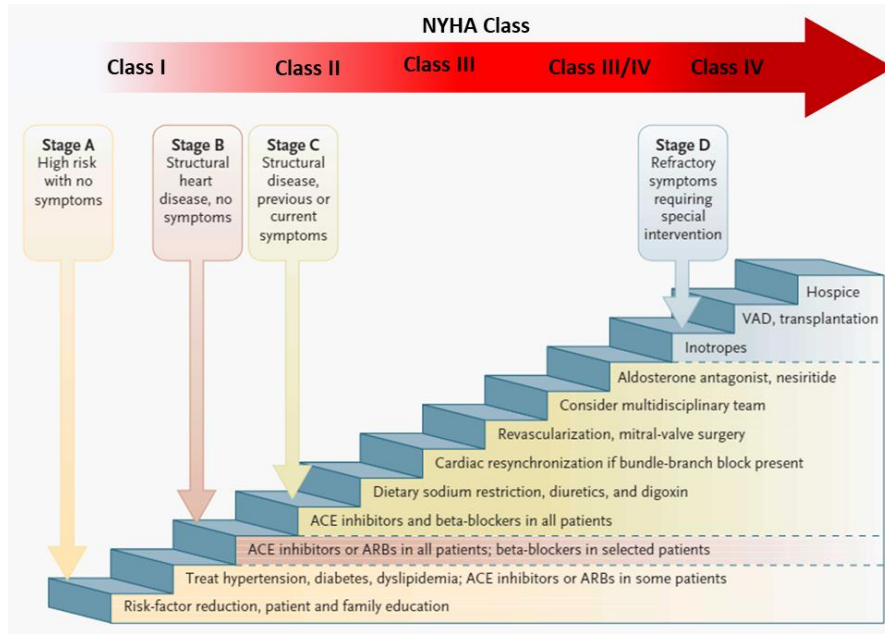
Figure 1-9 NYHA class representing different stages of HF. The recommended treatment is shown at each stage. When all options have failed, heart transplantation or LVAD implants are the only viable option for advanced HF. Recreated from [142]

1.5.2 Continuous Flow LVADs vs. Pulsatile Flow LVADs

Early LVADs were Pulsatile Flow (PF) LVADs. PFLVADs will preload and deliver blood in a manner that is similar to the native ventricle. However, they suffered a high failure rate due to the presence of mechanical valve, were bulky, and lead to longer post-operation hospitalization . [143, 144] Continuous Flow (CF) LVADs are smaller in size, simpler in design, have higher durability and lower thrombosis rate. [143] It thus comes as no surprise that CFLVADs are preferred over PFLVAD with over 95% of total LVAD implants, 80% 1 year survival rate and 70% 2 years survival. [145] Moreover, new generation of CFLVADs (e.g., HeartMate III, Abbott Labs, Chicago, IL) use centrifugal pumps instead of axial flow or mixed flow impellers and magnetically levitated bearings. The smaller size of third generation pumps obviates the need for extensive tissue

dissection or abdominal pockets leading to simpler operation and lower reoperation rate. [146, 147] Additionally, the non-contact nature of magnetic impeller levitation significantly improved pump thrombosis over axial flow pumps. [146]

1.5.3 Diminished Pulsatility with CFLVAD support

Despite these positive clinical outcomes, the non-pulsatile nature of CFLVAD flow has raised concerns over their chronic use. Multiple adverse events have been reported with CFLVAD support, such as chronic closure of the aortic valve, abnormal physiologic profile of myocardial and vascular energy utilization, gastrointestinal bleeding, hemorrhagic strokes, arteriovenous malformations, valve fusion, and end organ failure. [148, 149] Moreover, other studies have reported reduction in coronary flow and elevated inflammatory response. [150, 151] For example, in a 2009 trial, the Heartmate II CFLVAD was compared to first generation pulsatile HeartMate XVE in 200 patients. While the survival rate was improved, 81% of patients receiving CFLVAD suffered from organ bleeding compared to 76% with PFLVAD. [152]

These adverse vascular events, attributed to diminished pulsatility, are thought to be caused by dysfunction of arterial endothelial cells, the primary transducers of pulsatility in the circulatory system. [153] This body of evidence has reestablished interest in the effects of pulsatile energy of blood flow and to explore whether it is possible to introduce pulsatile flow modes using CFLVADs, without reverting back to unreliable, bulky PFLVADs. Indeed, new third generation CFLVADs such as HeartMate III and HeartWare HVAD incorporate some pulsatile mode of operation to augment arterial pulsatility and potentially mitigate some of the adverse events seen with CFLVAD flow. [154]

1.5.4 Physiological control of LVADs

At any rate, the goal of chronic LVAD therapy is for the patient to become independent on clinical management of their device, thus allowing improved quality of life and home return. To achieve this, the pump must be able to adapt to the physiological requirements of the cardiovascular system and changes in the patient's state. [155] This infers that the pump and pump controllers need to be sensitive to the native heart's preload, afterload, heartrate…, etc. The collection of this information at high fidelity, however, is not straight forward. Implantation of pressure, flow or ventricular volume sensors is highly undesirable because they can cause thrombus formation and are subject to failure and sensor drift. [156, 157] Additionally, the choice of control parameters that reflect changes in tissue metabolic demand is highly critical. In chapter 2, we develop a sensorless control algorithm based on the pump speed to achieve physiological control of a CFVLAD and investigate its applicability in safely producing pulse flow modulation by ramping up and down the speed to create artificial arterial pulse.

CHAPTER 2: SENSORLESS CONTROL OF CFLVAD USING A MODEL OF THE CARDIOVASCULAR SYSTEM [2]

2.1 Current State of LVAD Control

Heart failure (HF) is a progressive disease that affects 6.5 million Americans and is the leading cause of death. Prevalence of HF is expected to rise by 46% by 2030 to an estimated 8 million patients. The only long-term survival option for advanced heart failure is heart transplantation, which, however, is restricted by the lack of donor organs and the absence of comorbid conditions.[141] To bridge the supply demand gap, CFLVADs have been used to provide mechanical circulatory support. To avoid ventricular suction, LVADs must provide adequate blood flow and meet the cardiac demand, which often changes with clinical and physical activity conditions (physiologic perfusion). When pump flow does not match cardiac demand, hypoperfusion of end-organs, ventricular volume overload, pulmonary edema, and tissue hypoxia may result. On the other hand, Over-pumping can result in ventricular suction. Ventricular suction is caused by a reduction in pump preload, which can lead to reduced pressure in the

---

ventricle. This causes the LVAD inlet cannula to become occluded, causing myocardial damage, pump failure, or ventricular arrhythmias that can cause adverse events or death. With CFLVADs, physiological perfusion and suction prevention is difficult due to: (1) nonlinearity of the circulatory system, (2) discontinuity in flows due to the valves, and (3) increased afterload and lower preload sensitivity compared to the native heart. [160, 161], and (4) lack of biological sensors such as baroreceptors and biological feedback mechanisms such as sympathetic and parasympathetic response, Frank Starling mechanism, etc. Clinically, LVADs currently do not incorporate physiologic control mechanisms. Clinicians manually set LVAD speed setpoints based on oxygen saturation, clinical symptoms, echocardiography, or estimated flows. [162-164]-Suction detection algorithms based on analysis of pump speed or pump current morphology are incorporated clinically, but these algorithms can only detect suction after it has occurred and cannot prevent suction. [165-167] Physiologic control and suction prevention have been addressed with multiple approaches, but these require direct measurement of pressure, flow, and ventricular volume, which requires the implantation of sensors. [168-170] Sensors are prone to drift, can form thrombus, septicemia, fail and are therefore undesirable because they increase the overall system complexity and reduce reliability. Other approaches employ model-based parameter estimation using various of techniques such as autoregressive exogenous modeling and Extended Kalman Filters [171-176] Model-based methods, however, are susceptible to changes in blood viscosity, friction forces, and impeller inertia, and are computationally expensive. Clinical studies have shown that flow estimators have significant errors [177] and may require pressure sensors for higher accuracy. [178] Additionally, the model parameters have to be recalculated and

36

validated for different pumps and small changes in pump geometry can lead to larger changes in pressure-flow relationship. [179] A recent study by Petrou et al. [180] looked into the potential use of machine learning to predict blood viscosity for CFLVAD support, but the method lacked in-vivo validation, was prone to learning error, and increased controller complexity. A number of approaches to increase the pressure sensitivity of rotary pumps have been proposed [181-183], but these modifications require FDA approval and may not be applicable universally. To overcome these limitations, this chapter introduces a simple and novel control algorithm based on the intrinsic pump speed which can be measured using phase currents or hall effect sensors and does not deteriorate. The control algorithm requires only maintaining the differential pump speed (ΔRPM) at a user-defined value and does not require any parameter estimation.

2.2 *In-silico* modeling of the cardiovascular system

The Windkessel lumped parameter representation of the cardiovascular system models the arterial circulation as two elements: resistance element, R and a compliance element C. To achieve a more involved and accurate representation of the cardiovascular system, it may be modeled as multiple RC blocks, each representing different regions of the vascular tree. For this study, we used a network-type model which subdivides the human circulatory system into a number of lumped parameter blocks with each block characterized by its own resistance and compliance. [32] This model has been extensively used and validated in literature [168, 184-187] and has been previously used for developing timing algorithms and control systems for LVAD and BiVAD. Four boundary conditions are defined at each block: inlet pressure, inlet flowrate, outlet

pressure, and outlet flowrate. A schematic representation of the mathematical model is shown in Figure 2-1.
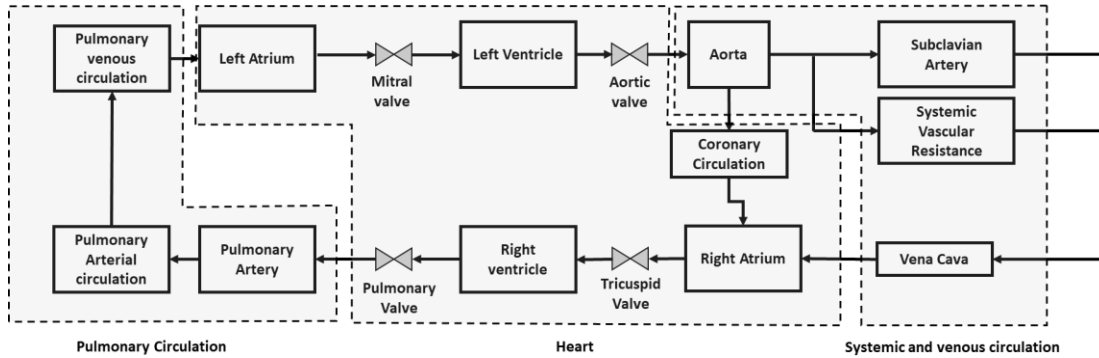
Figure 2-1 Schematic representation of the nonlinear mathematical model used. The cardiovascular system is simulated using twelve lumped blocks, each is defined by a resistance and a compliance. The instantaneous volume is calculated using differential equation (3).

Here, the divides the circulatory system into twelve blocks (left ventricle, aorta, coronary circulation, innominate and right subclavian artery, systemic circulation, vena cava, right atrium, right ventricle, pulmonary artery, pulmonary arterial circulation, pulmonary venous circulation, and left atrium) and four heart valves. The model contains 5 active elements: left ventricle, right ventricle, left atrium, right atrium, and coronary circulation whose compliances or resistances are non-linear and are a function of time within the cardiac cycle. The four heart valves are differential pressure operated, and the opening and closing of the valves causes a discontinuity in blood flow. Each block consists of a storage element or compliance, (C) and a resistive element, (R) which can predict the block's volume (V) and pressure (P) using the following equations:

$$\frac{dV_n}{dt} = F_n{}^{in} - F_n{}^{out} \tag{2}$$

$Substituting\ \ C_n = \frac{V_n}{P_n}, and\ F_n{}^{in} = \frac{P_{n-1}-P_n}{R_{n-1}}, and\ F_n{}^{out} = \frac{P_n-P_{n+1}}{R_n}\ \ into\ (2)\ we\ get$

$$\frac{dV_n}{dt} = \frac{V_{n-1}}{C_n R_{n-1}} - \frac{V_n}{C_n}\left(\frac{1}{R_{n-1}} - \frac{1}{R_n}\right) + \frac{V_{n+1}}{C_{n+1} R_n} \tag{3}$$

Where $\frac{dV_n}{dt}$ is the rate of change of the volume in block n, $F_n{}^{in}$ and $F_n{}^{out}$ are the

blood flow rate in and out of block n respectively, P_n is the pressure in block n. The

active compliance of the right and left ventricles are a function of time. The periodically

changing compliance introduces a change in block volume and pressure according to

$C_n = \frac{V_n}{P_n}$; hence creating flow.
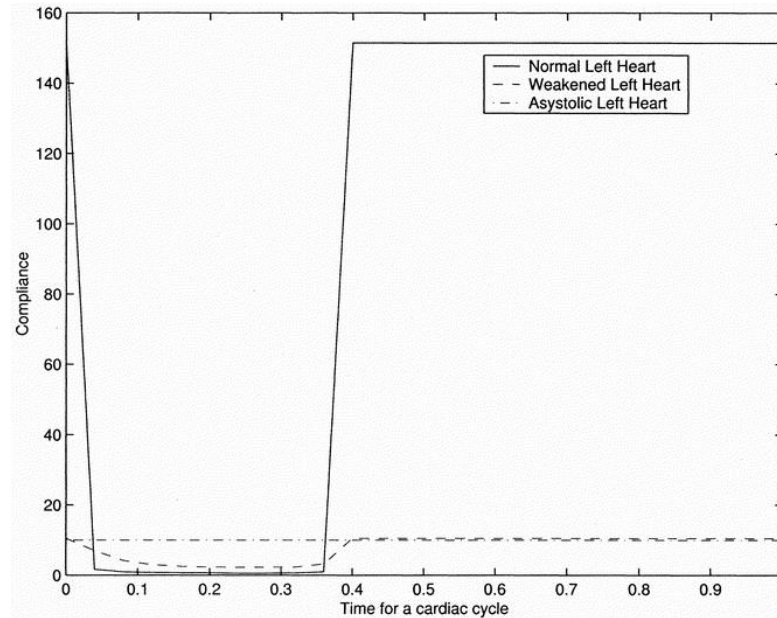
Figure 2-2 Adapted from [32] . Example of active compliance element in the cardiovascular model

used. Typical left ventricular compliance is shown as a function of time. Different compliance

waveforms can be used to model the failing heart (in dotted line).

2.3 Sensorless Speed-Based control of CFLVAD

2.3.1 Study Hypothesis

To avoid unreliable sensor implantation or complicated or inaccurate model-based estimations, a sensorless controller for CFLVAD that is based solely on the intrinsic pump speed was developed. The hypothesis is based on the observation that the pulsatility in the pump speed signal is a measure of the degree of ventricular preload. As shown in *Figure 2-3*, At low pump flow, the differential pump speed ($RPM_{max} - RPM_{min}$) is increased. This is because the heart filling volume increases which leads to more blood being pushed out by the ventricle through the pump inlet. The opposite effect takes place when the pump speed is increased and the amount of blood inside the ventricle is reduced. This in turn reduces the blood that is being pushed by the ventricle contraction to the pump inlet. Based on this observation, it may be possible to use the differential pump speed, ΔRPM as a marker for ventricular preload and tissue demand and thus adjust flow accordingly.
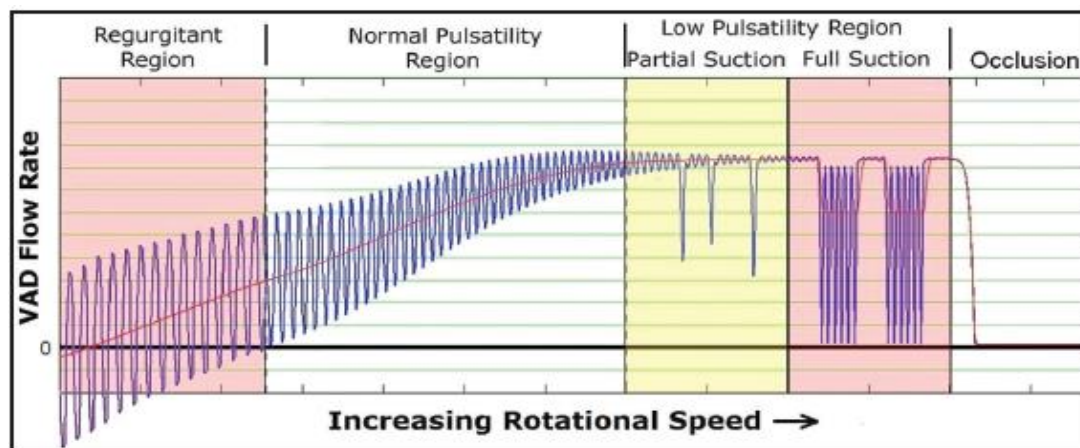
Figure 2-3 Pump flowrate pulsatility at different rotational speeds. As the pump speed increases the pulsatility(i.e., ΔRPM) of the VAD flowrate and VAD speed (not shown)

decreases and the pump approaches suction. When the pump speed decreases, the VAD flowrate and speed pulsatility will increases. Source: HeartWare HVAD training manual.

2.3.2 Controller structure and objectives

The controller objective to maintain a fixed differential pump speed (ΔRPM) to avoid suction events during reduced preload, while producing sufficient perfusion at exercise and rest. The control system relies solely on noisy measurements of pump speed ΔRPM_n, which can be measured using phase currents or hall effect sensors. For model-independent control, a moving average filter (window size =8 data points) was used to filter the rotor speed measurement. Using PI controllers, the differential pump speed setpoint was maintained using the following equation:

$$ I = -K_p\big(\Delta\text{RPM}_{ref} - \Delta\text{RPM}_f\big) - \frac{K_p}{\tau}\int_0^t \big(\Delta\text{RPM}_{ref} - \Delta\text{RPM}_f\big)dt \qquad (4) $$

where I is the pump current, ΔRPM_{ref} is the reference differential pump speed and ΔRPM_f is the filtered differential pump speed at any instant, K_P and τ are the proportional and integral gains, respectively. It is important to note that the (4) is due to the inverse relation between pump speed pulsatility and ventricular loading. High pump speed pulsatility implies low ventricular unloading and low pulsatility implies a high ventricular unloading. The PI-controller gains were tuned a priori using a direct numerical search approach [188]. K_P was set to 0.00025, and τ was set to 5. ΔRPM_n was calculated as the difference between the maximum and minimum noisy RPM values during a moving time window of the preceding two seconds. ΔRPM_{ref} was set to 800 RPM. The control schematic is shown in *Figure 2-4*.
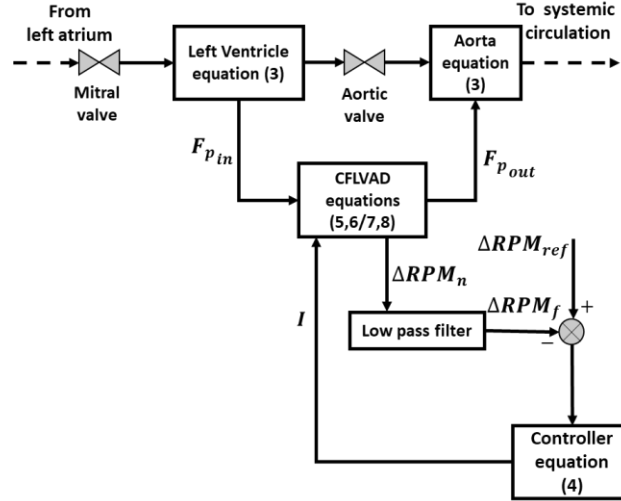
Figure 2-4 *Published in [159]* Control schematic for the proposed ΔRPM controller. Measured of the noisy pump speed are filtered and the filtered ΔRPM is fed to the PI controller in equation (4) which work to maintain a physiologically relevant pump speed differential.

2.4 Benchmark Testing and Study Methods

2.4.1 Mathematical model of CFLVAD

In order to incorporate the CFLVAD controller in-silico, models developed by Choi et al. [189] and Krishnan [190] were used to simulate the CFLVAD. In this model, a dynamic axial flow pump is driven by a brushless dc motor and the model for the brushless dc motor is given by

$$J\frac{d\omega}{dt} = \frac{3}{2}K_B I - B\omega - a_0\omega^3 - a_1 F_P \omega^2 \qquad (5)$$

Where J is the rotor inertia, ω is the rotor speed in rad/s, K_B is the back electromotive force constant, I is the phase current, B is the damping coefficient, a_0 and a_1 are

correlation constants, and F_P is the pump flow in ml/s. The brushless DC motor is couple with a model for the axial flow pump, which is given by

$$\frac{dF_P}{dt} = -\frac{b_0}{b_1}F_P - \frac{b_2}{b_1}\omega^2 + \frac{1}{b_1}\Delta P \tag{6}$$

b_0, b_1, and b_2 are experimental constants and F_P is the pump flow rate. The equation parameters are experimentally characterized and given as:

$J = 9.16 \times 10^{-7} Kg.m^2$, $K_B = 0.003 Kg.\frac{m^2}{A.s^2}$, $a_0 = 7.38 \times 10^{-13} Kg.m^2.\frac{s}{ml^3}$, $B =$

$6.6 \times 10^{-7} Kg.\frac{m^2}{s}$, $a_1 = 1.98 \times 10^{-11} Kg.m^2.\frac{s}{ml}$, $b_0 = -0.296\ mmHg.\frac{s}{ml}$, $b_1 =$

$-0.027\ mmHg.\frac{s^2}{ml}$, and $b_2 = 9.33 \times 10^{-5} mmHg.s^2$.

In the context of the lumped parameter model of the cardiovascular system , the CFLVAD is incorportated flow path from the left ventricle to the aorta as shown in *Figure 2-4*. In order to demonstrate pump independency, we have implemented the ΔRPM controller using Deltastream mixed flow Pump (DP2), Medos AG,Stolberg, Germany. For the DP2 pump, we used the pump model developed by Petrou et al. [191]. The pump equations for the DP2 pump

are:

$$\frac{d\omega}{dt} = \frac{1}{J(\omega)}\left(K_T I - g_1(\omega) + g_2\omega - g_3\omega^2 - g_4 F_P\omega\right) \tag{7}$$

and

$$\frac{dF_P}{dt} = -\frac{1}{F}\left(-\Delta P + f_1\omega^2 - f_2 F_P - f_3 F_P{}^2\right) \tag{8}$$

Where $f_1, f_2, f_3, K_T, g_1(\omega), g_2, g_3\ g_4, J(\omega),$ and F are coefficients adapted from [191] are given as

$$f_1 = \quad 6.572 \times 10^{-6} \qquad mmHg/RPM^2$$

$$f_2 = \quad 2.071 \qquad mmHg/L/min$$

$$f_3 = \quad 1.043 \qquad mmHg/(L/min)^2$$

$$K_T = \quad 13 \times 10^{-3} \qquad N.m.A^{-1}$$

$$g_1 = \quad \begin{bmatrix} RPM & Nm \times 10^{-3} \\ 2000 & 3.563 \\ 3000 & 3.447 \\ 4000 & 3.480 \\ 5000 & 3.317 \\ 6000 & 3.264 \end{bmatrix} \qquad N.m \times 10^{-3}$$

$$g_2 = \quad 1.087 \times 10^{-6} \qquad N.m/RPM$$

$$g_3 = \quad 3.280 \times 10^{-10} \qquad N.m/RPM^2$$

$$g_4 = \quad 2.629 \times 10^{-7} \qquad mmHg/(\frac{L}{min}.RPM)$$

$$F = \quad 0.8596 \qquad mmHg/\frac{L}{min}/s$$

$$J = \quad \begin{bmatrix} RPM & \frac{Nm}{RPM/s} \times 10^{-6} \\ 2000 & 1.444 \\ 3000 & 1.498 \\ 4000 & 1.560 \\ 5000 & 1.615 \\ 6000 & 1.723 \end{bmatrix} \qquad \frac{Nm}{RPM/s} \times 10^{-6}$$

2.4.2 Comparison with Sensorless Control Algorithms

The robustness analysis was performed by introducing different levels of normally distributed noise (1%-10%) to the pump speed at 100-Hz sampling frequency. Two sensorless algorithms previously proposed were compared to the ΔRPM algorithm: (1) a constant speed algorithm and (2) a constant differential pressure algorithm, ΔP_d (pressure difference between left ventricle and aorta). Constant speed control is the current clinical standard. This control mode was achieved by setting the pump speed to 10700 RPM set point using PI controller ($K_P = 0.0028$, $\tau = 5$). The constant speed controller is referred

to as the constant RPM controller. In differential pressure controller, ΔP_d was estimated using the method described in [174]. ΔP_d was estimated using the measured pump speed, the estimated pump flow F_P, a Golay-Savitzky (GS) filter and an extended Kalman filter (EKF). ΔP_d reference set point was set to 87 mmHg. The differential pressure controller had a gain, $K_P = 0.003$, time constant, $\tau = 5$, and used a low-pass Butterworth filter with a 5-Hz cutoff frequency. The differential pressure controller will be referenced as, ΔP control.

2.4.3 Comparison with Sensor-Based Control Algorithms

In addition to other sensorless controllers, ΔRPM control algorithm was compared to the following sensor-based LVAD control algorithms proposed in literature: (1) control based on left ventricular end diastolic pressure (LVEDP) [192] and (2) control based on mean aortic pressure (MAOP)[193]. Mean aortic pressure control was achieved by setting the reference MAOP to 100 mmHg at which the pump flow was 5 l/min at rest. The gain, K_P was set to 0.04, and time constant, $\tau = 5$. T Controlling left ventricular end diastolic pressure used a constant reference pressure of 7 mmHg at which the pump provided approximately 5 l/min at rest and used a constant reference pressure system and used $K_P = 0.05$, $\tau = 5$. Efficacy and robustness of all algorithms were tested in-silico using (1) rest and exercise conditions, (2) a rapid eight- fold increase in pulmonary vascular resistance (PVR) under rest and exercise, (3) transitions from rest to exercise and exercise to rest, (4) safe mode during left heart fibrillation, and (5) 1% to 10% RPM measurement noise through (1) to (4). (4) and (5) were only applied to the proposed ΔRPM control.

2.4.4 Safe Mode

ΔRPM control is based on the pulsatility of the pump speed which is caused by the reserve native contractility of the left ventricle. In the event of an asystolic heart, the ΔRPM controller was designed to switch to a safe mode which will switch to a constant RPM when the mean pump speed drops below a certain threshold (8000 RPM) for longer than 10 seconds. Asystolic heart will diminish the pump speed pulsatility and the ΔRPM controller will work to reduce pump speed. This can lead to hypoperfusion, mortality and pump thrombosis. The safe mode maintains the mean pump speed at 8500 RPM to prevent pump stoppage and thrombosis in dangerous conditions.

2.4.5 Introducing a pulse flow modulation mode to augment arterial pulsatility using ΔRPM control algorithm

The small size, easier implantation, and low failure rate of CFLVADs made them the favorable option over first generation PFLVADs. However, as discussed in *1.5.3*, the adverse events associated with diminished pulsatility during CFLVADs chronic use have prompted pump manufacturers to incorporate pulsatile modes of operation to augment arterial pulsatility. Without proper control, these modes are vulnerable to the same disadvantages of constant speed pump control. To show the versatility of the ΔRPM controller, a flow modulation mode was developed that was based on the measurement of ΔRPM during pump operation. The control scheme is shown in *Figure 2-5* below. The goal of the algorithm is to safely incorporate artificial pulsatility in the ΔRPM controller while avoiding ventricular suction and providing adequate perfusion. Here, ΔRPM was modulated between 900 RPM and 1800 RPM. This was achieved by ramping the pump speed up and down between 12000 and 7500 RPM at rate of 1800 RPM/s^2. This was

thought to be sufficient to achieve a pulse frequency >10 beat/min at rest. It is important to note that the algorithm will switch the pulse primarily based on the measured ΔRPM signal. In that way, the pump is protected against excessive suction or reduced perfusion. The asynchronous pulse flow modulation strategy was tested 1) during rest, 2) during exercise, 3) 5x PVR during rest and exercise, and 4) 1%-5% noise during all conditions.
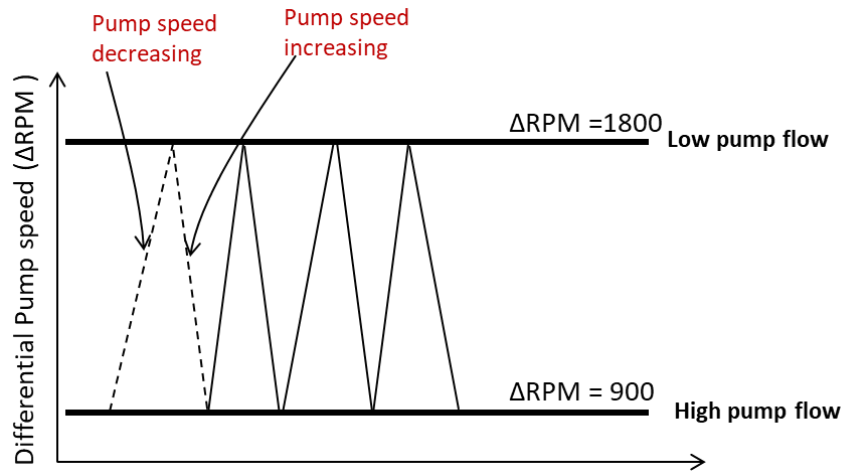
Figure 2-5 [194] *ΔRPM* pulse flow modulation mode developed. The pump speed is ramped between two limits using a PI control structure. An upper and lower *ΔRPM* limits are put to ensure safe pulsatile operation which avoids ventricular suction, low perfusion, and diminished pulsatility.

2.4.6 Data Analysis

MATLAB (MathWorks, Natick, MA, USA) was used to calculate the hemodynamics and CFLVAD parameters. Aortic systolic, diastolic, and mean pressures, end systolic and end diastolic pressures, and aortic flow rate were computed as part of the data analysis. In clinical practice, the left ventricular end diastolic diameter or pressure is used to define

suction [195]. Consequently, a suction event occurs when the ventricular end diastolic pressure is less than 2 mmHg.

2.5 Results

2.5.1 The proposed controller (ΔRPM control)

		LTO (L/min)	AoP (mmHg)	LVEDP (mmHg)	LVV (ml)	min LVP (mmHg)	Suction
Rest	NH baseline	5.0	122/78	8	85/147	5	No
	FH baseline	3.7	96/63	16	181/229	9.5	No
	ΔRPM ctrl	5.0	104/100	5.6	40/65	3.5	No
	CS ctrl	5.0	104/100	5.4	36/63	3.3	No
	ΔP ctrl	4.9	103/98	6.6	49/77	4.4	No
	EDP ctrl	5.0	102/97	7	53/82	4.8	No
	MAOP ctrl	5.0	103/98	6.3	46/74	4.1	No
Exercise	NH baseline	8.2	129/84	6.4	45/112	3.0	No
	FH baseline	6.1	102/65	21	190/242	16.4	No
	ΔRPM ctrl	8.0	108/104	7.4	58/94	5.2	No
	CS ctrl	7.6	103/98	10	88/12	7.8	No
	ΔP ctrl	7.9	106/102	8.2	68/104	6.0	No
	EDP ctrl	8.1	108/105	7.0	54/89	4.9	No
	MAOP ctrl	7.6	104/98	10.2	89/126	7.8	No
Rest- 8xPVR	ΔRPM ctrl	5.0	104/100	5.6	40/65	3.51 (3.1)	No
	CS ctrl	4.7	95/94	0.9(-0.2)	2/11	0.37 (-0.7)	Yes
	ctrl	4.6	93/91	2.5(0.8)	14/34	1.5 (0.4)	Yes (IS)
	EDP ctrl	4.3	90/85	7(4.4)	55/82	4.8 (3.7)	No
	MAOP ctrl	-*	100/99.9	-3.7(-3.7)	-*	-4.4 (-4.4)	Yes
Exercise 8x PVR	ΔRPM ctrl	7.0	96/92	7.2(4.6)	58/91	5.2 (3.1)	No
	CS ctrl	7.14	96/93	6.2(5.0)	49/80	4.5 (3.5)	No
	ΔP ctrl	7.3	98/95	4.8(3.0)	32/63	3.3 (1.8)	No
	EDP ctrl	7.1	96/92	7(5.1)	56/89	5.0 (3.5)	No
	MAOP ctrl	7.6	101/100	2.0(2.8)	9.3/32	1.4 (1.9)	Yes

Table 2-1 Published in [159] Control outcomes during multiple test conditions using the proposed controller as compared to four different controllers from literature. **LTO**: Left Total Output, **AoP**: Aortic pressure, **LVEDP**: Left ventricular end diastolic pressure, **LVV**: Left ventricular volume. **LVP**: Left ventricular pressure, **IS**: Intermittent suction. Values

in parenthesis are the minimum transitional values during 8x PVR. **ΔRPM ctrl**: speed pulsatility control, **ΔP ctrl**: differential pressure control **CS ctrl**: constant speed control, **EDP ctrl**: end diastolic pressure control, **MAOP ctrl**: mean aortic pressure control. * Note that during high levels of ventricular suction as in the MAOP control with reduced preload, the pump flow rate and ventricular volumes are variable and thus are not included in the table.

Compared to other controllers tested, *ΔRPM* control provided physiologic perfusion and prevented ventricular suction in all test conditions. During rest *ΔRPM* control provided 5 l/min and 8 l/min during exercise. As shown in ***Table 2-1*** and ***Figure 2-6***, *ΔRPM* algorithm prevented ventricular suction during a rapid 8x increase in pulmonary vascular resistance (PVR). During 8x PVR, the end diastolic pressures were 5.6 mmHg and 7.4 mmHg at rest and exercise respectively.

The controller adapted well to instantaneous transitions from rest to exercise and exercise to rest, ***Figure 2-8***. It only took less than 60 seconds for the controllers to reach 95% of the steady state values in all tested cases. The *ΔRPM* control algorithm achieved similar results with the DP2 pump during rest and exercise, and prevented ventricular suction with 8x PVR, ***Figure 2-9***.
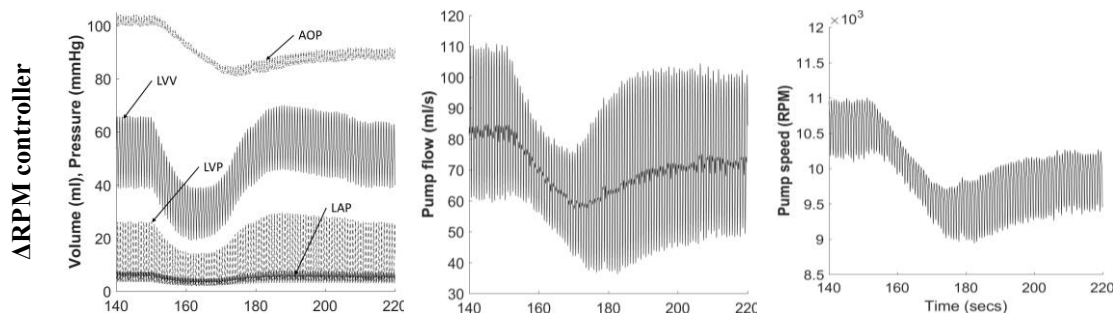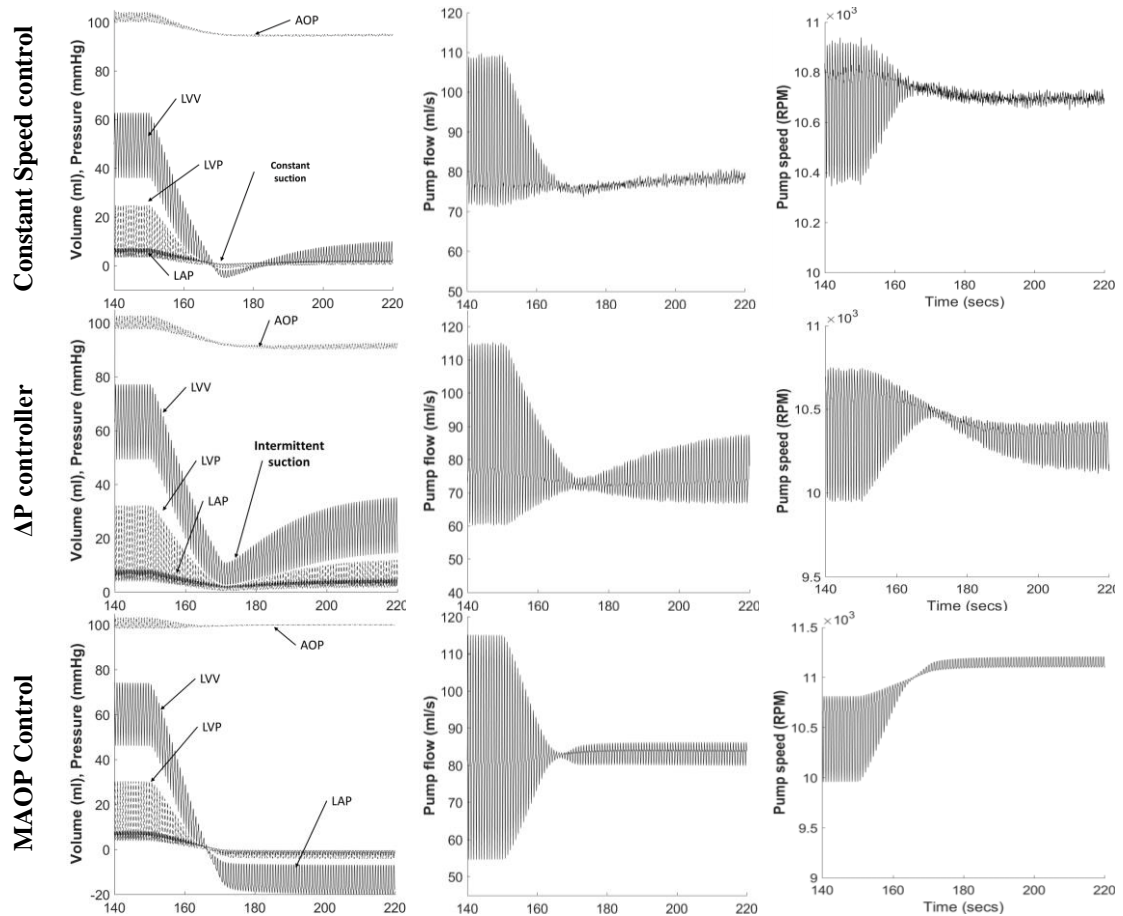
Figure 2-6 Published in [159] Controller response comparison during rapid

reduction in preload (8x PVR). The preload reduction was introduced at t=150s for

the ΔRPM, constant RPM, ΔP, and MAOP controllers. Constant suction is evident

in constant speed control with end diastolic pressures below 1mmhg at steady state.

ΔP control caused intermittent suction during transition, but soon recovered

afterwards. MAOP control, cause excessive constant suction. The proposed ΔRPM

controller maintained the highest safety margin at steady state and during transition

as seen with ventricular volume and pressure waveforms. **AoP**: Aortic pressure,

LVP: Left ventricular end diastolic pressure, **LVV**: Left ventricular volume, **LAP**:

Left atrial pressure, **MAOP**: Mean Aortic Pressure.

50

2.5.2 Constant RPM control (Clinical standard)

During rest, constant RPM control provided mechanical unloading of the heart and provided (5.0 l/min) without suction events and maintained LVEDP at 5.4 mmHg. During exercise, the constant RPM control slightly augmented the pump flow (7.6 l/min) but to a lower degree than the normal heart and ΔRPM control flow augmentation. Significantly, during the rapid increase in PVR, constant RPM control caused suction at rest (steady state LVEDP = 0.9 mmHg, with a LVEDP as low as -0.2 mmHg during transition), *Figure 2-6*. Suction did not occur during exercise with an eight-fold increase in PVR with a minimum ventricular pressure of 3.1 mmHg. Transitions from rest to exercise and exercise to rest also did not trigger ventricular suction.

2.5.3 *ΔP* control (model-based estimation)

While *ΔP* control supplied adequate perfusion during rest (4.93 l/min) and exercise (7.9 l/min), intermittent suction (IS) happened during 8x PVR increase at rest (0.8 mmHg LVEDP during transition), *Figure 2-6*, and soon recovered to 2.5 mmHg at steady state.

ΔP controller adapted well to instant transitions from exercise to rest and rest to exercise without any suction events.

		Actual ΔRPM	Filtered ΔRPM	LVEDP (mmHg)	LTO (l/min)	Suction
1%	Rest	798	793	5.6	5.0	No
	Exercise	818	766	7.4	8.0	No
	Rest 8x PVR	817	764	7.1(4.6)	4.4	No
4%	Rest	667	711	4.8	5.0	No
	Exercise	622	684	6.3	8.1	No
	Rest 8x PVR	596	665	3(1.5)	4.3	No
6%	Rest	398	745	3.2	5.3	No
	Exercise	455	667	4.8	8.2	No
	Rest 8x PVR	513	723	2.8(-0.2)	4.5	Yes (IS)

Table 2-2 Published in [159] Noise tolerance of the proposed ΔRPM control algorithm with 1%, 4%, 6% normally distributed noise. Values in parenthesis are the minimum transitional values during 8x PVR. After 6% noise, control deteriorated, and intermittent or constant suction events occurred.

2.5.4 MAOP control (sensor-based control)

MAOP control with as set point at (100 mmHg) led to adequate perfusion during rest (5.0 l/min) but could not provide adequate perfusion during exercise (7.6 l/min). The MAOP control failed to adapt during reduced preload condition (8x PVR) with the onset of constant suction and negative LVEDP as shown in *Table 2-1*.

2.5.1 EDP control (sensor-based preload control)

EDP control led to adequate perfusion during rest (5 l/min) and exercise (8.1 l/min) as well as protection against suction during reduced preload and instantaneous transition from exercise to rest and rest to exercise. This is expected since a control based on preload is effectively mimicking the natural Frank-Starling mechanism. However, EDP control performance deteriorated with the introduction of sensor drift as low as 5 mmHg (with zero measurement noise), which is below the reported drift for similar inlet/outlet sensors[156, 157], and intermittent suction occurred when using 8x PVR. Higher levels of sensor drift caused constant suction, as shown in *Figure 2-7*.
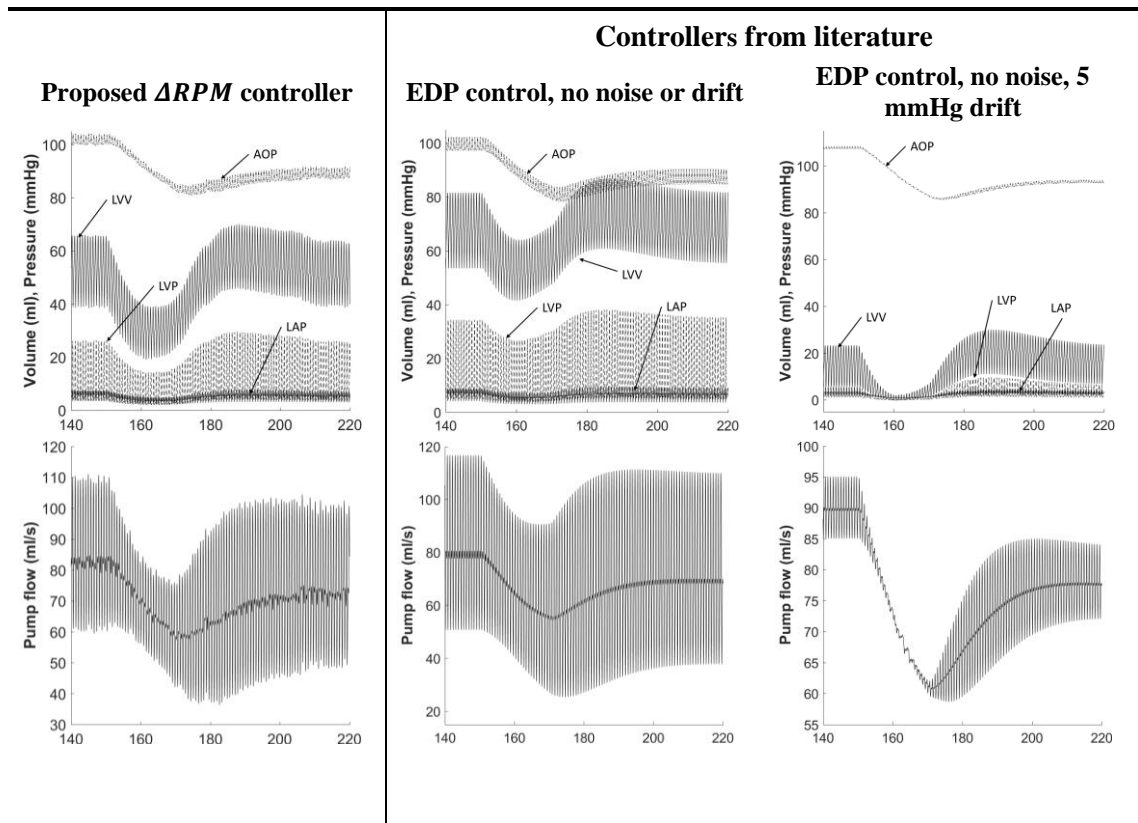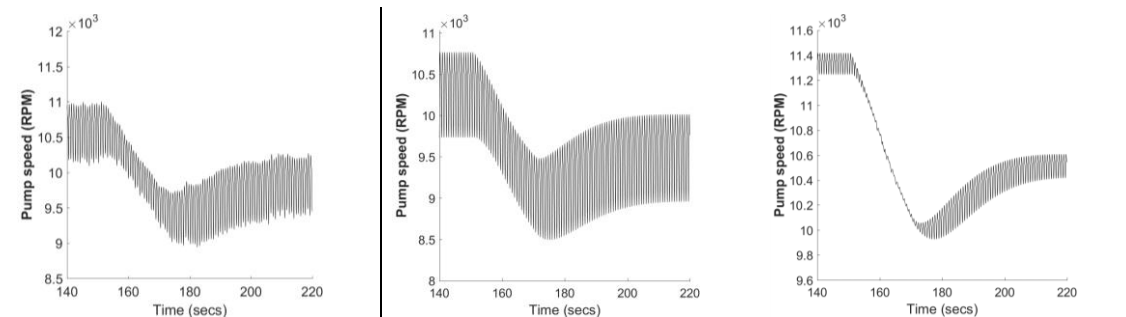
Figure 2-7 *Published in [159]* Control comparison using EDP control with and without a 5mmHg inlet pressure sensor drift during 8x PVR. Intermittent suction is seen transitionally as the left ventricular volume and pressure fall rapidly but soon recover. Current implantable pressure sensor technologies have reported >4x higher sensor drifts in 1 year. It is important to note that for EDP control was used with a single EDP reference point.

2.5.2 Noise tolerance

To illustrate the noise tolerance of the proposed algorithm, ΔRPM control tested with different levels of measurement noise. The controller was able to provide physiologic perfusion and suction prevention with eight-fold PVR at rest with up to 6% noise while only using a moving average filter, as shown in *Table 2-2*. The controller caused intermittent suction with 7%, 8% and the control quality deteriorated completely with 10% noise. Any noise level greater than 6% caused some degree of suction or intermittent suction.
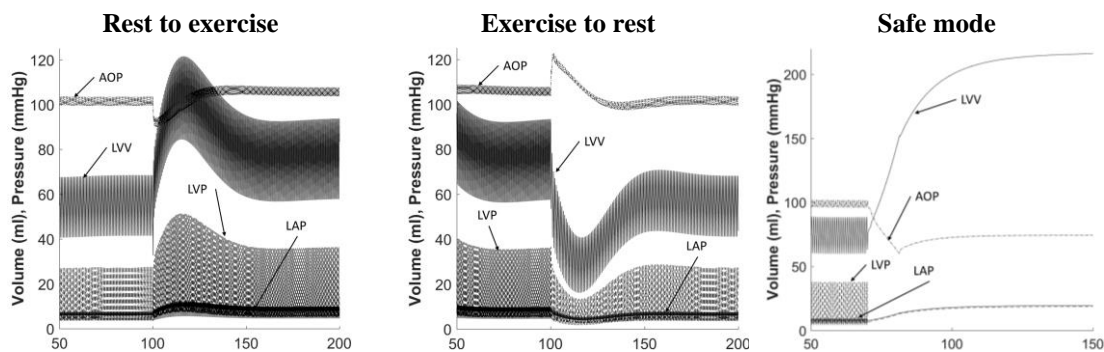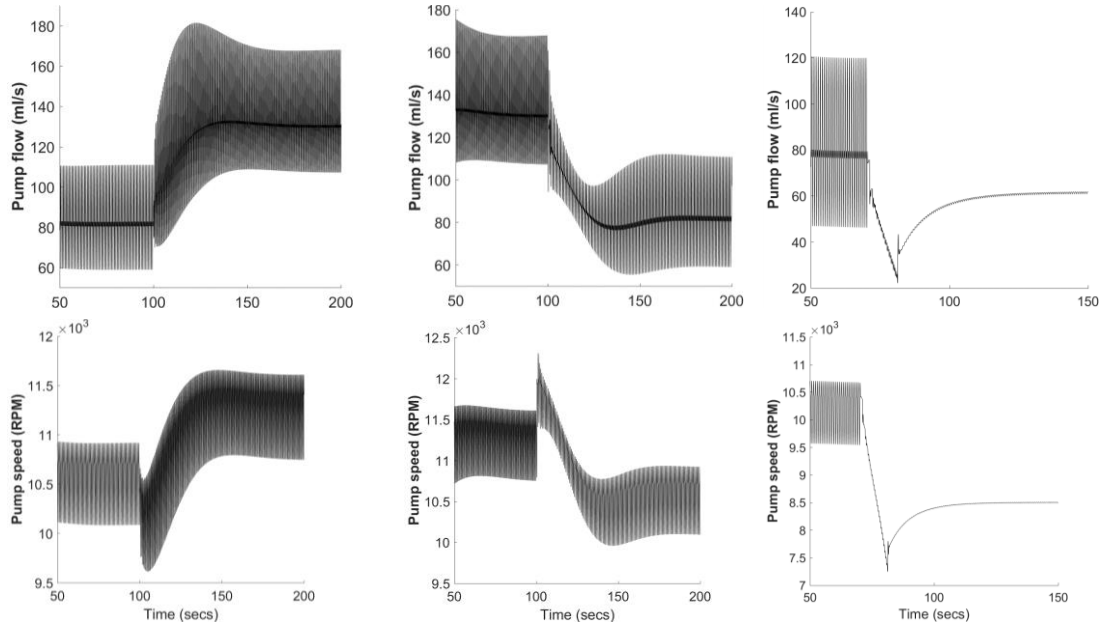
Figure 2-8, *Published in [159]* hemodynamic results using the proposed controller (ΔRPM controller) during transition from rest to exercise and exercise to rest at t=100s, and during asystole (t=70s). The safe mode is triggered when the pump speed drops below 8000 RPM for longer than 10s. A constant speed control then maintains the pump speed at 8500 RPM which reverts the heart to HF baseline.

2.5.3 Safe mode

When the pump speed dropped below 8000 RPM for more than ten seconds, the safe mode detected the onset of asystole. Automatically, the controller switched to a constant speed control and maintained the pump flow rate at 3.7 l/min, which is equivalent to the output of an unassisted failing heart (see ***Table 2-1***) and caused no suction at rest. **Figure 2-8** shows the safe mode in which left heart asystole is induced at t=70s and the controller maintains at rest a mean pump speed of 8500 RPM.

2.5.4 Pulsatile mode using *ΔRPM* control

Axial Flow Pump
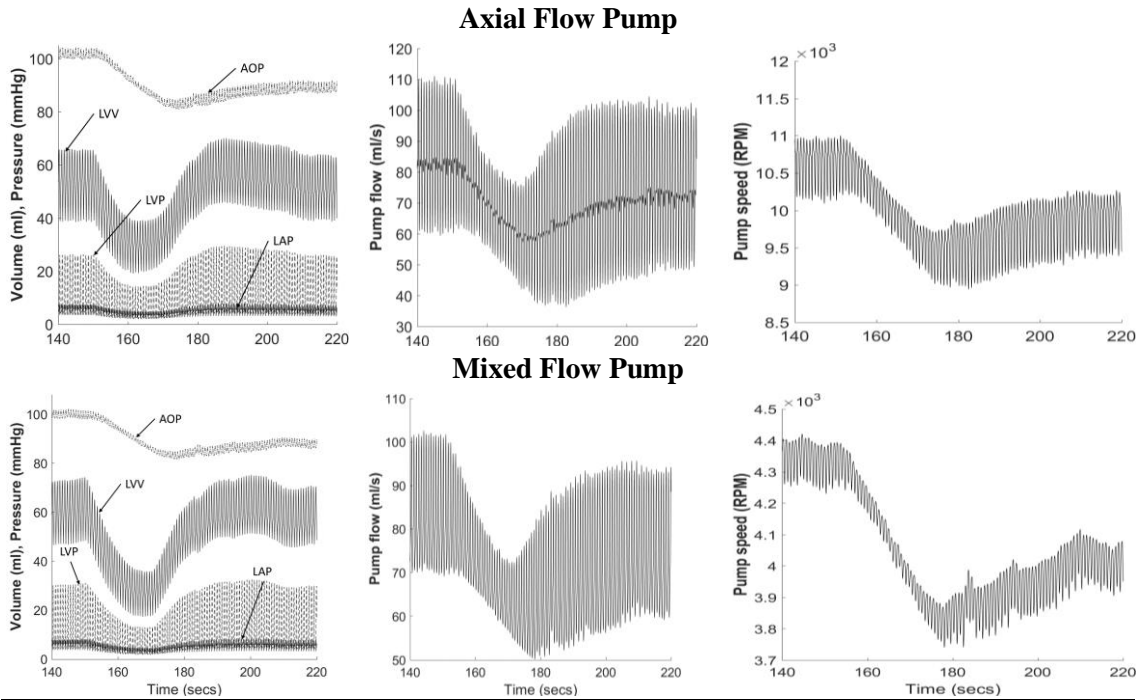
Mixed Flow Pump

Figure 2-9   Published in [159] Suction prevention during reduced preload (8X PVR) with an axial flow pump and mixed flow pump. Increased PVR was initiated at t=150 s. The controller successfully prevented suction for both pumps with 1% normally distributed noise.

Pulse flow modulation provided adequate perfusion at rest (5.1 L/min) and prevented ventricular suction with 5x PVR increases. The dynamic modulation strategy resulted in ~30 mmHg of arterial pulse pressure (115/85 mmHg) and 10 beats/min pulse frequency, *Figure 2-10*. At 5x PVR, no intermittent suction was noticed transiently, and the minimum ventricular pressure did not drop below 1 mmHg as shown in Figure .

Similarly, during exercise, the CFLVAD augmented blood flow and provided 8.0 L/min, 28 mmHg pulse pressure at 7 beats per minute (*Figure 2-10)*, and prevented ventricular suction at 5x PVR, *Figure 2-11*. The pulsatile mode was able to provide normal,

physiological perfusion at rest with up to 3% noise. However, at 4% speed measurement

noise, intermittent suction was seen with 5x PVR transitionally, and was persistent with

5% noise.
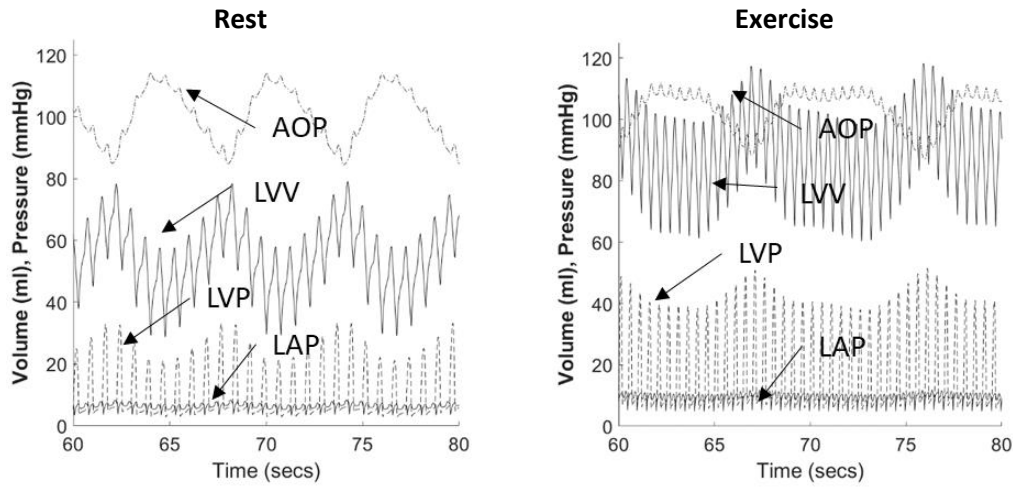
Figure 2-10 [194]Pulsatility augmentation mode using ΔRPM control algorithm

during rest and exercise. Pulse pressure was increased to 30 mmHg at rest and 28

during exercise.
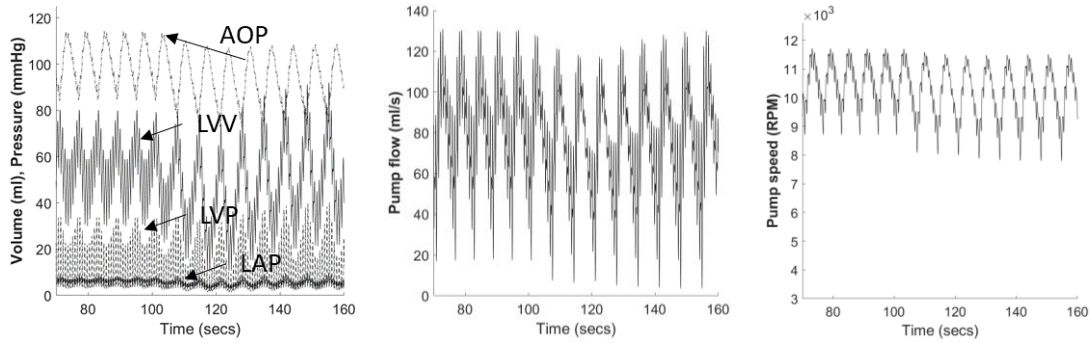
Figure 2-11 [194] 5-fold rapid increase in PVR during rest with pulsatility

augmentation did not result in suction event. 5x-PVR increase was simulated at t =

100s.
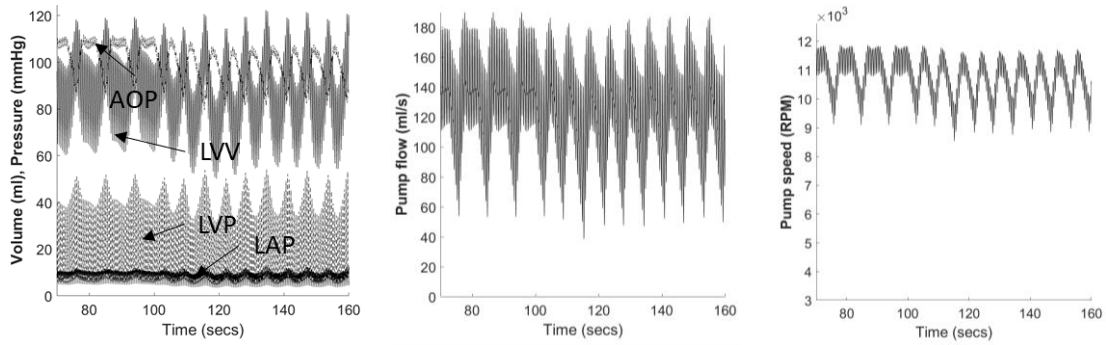
Figure 2-12 [194] 5-fold rapid increase in PVR during exercise did not cause

ventricular suction with pulsatile mode turned on. The onset of PVR increase was

initiated at t =100.

2.6   Discussion

2.6.1   Novelty and significance of the ΔRPM Control Algorithm

A set of in silico experiments demonstrated the feasibility of adapting pump flow

to physiologic demand and preventing ventricular suction when the proposed ΔRPM

control algorithm is employed. One of the novel aspects of the proposed algorithm is the

choice of the control variable (ΔRPM) that, even with a simple PI controller, can produce

physiological control and suction prevention with only a single constant ΔRPM setpoint. It is important to note that the ΔRPM control achieved adequate perfusion both at rest and during exercise and prevented suction both during rapid changes in preload (eightfold increase in PVR) as occurs with the Valsalva maneuver or during coughing but to a lesser extent. The proposed control algorithm demonstrated superior performance over the current clinical standard using constant speed control, where ΔRPM control provided greater flow or equivalent resistance to suction. Adding to that, we implemented the proposed algorithm using a mixed flow pump (DP2) and achieved similar results and adequate perfusion suction prevention, demonstrating that the algorithm is independent of the pump design., *Figure 2-9*.

Effectively, the ΔRPM control synchronizes the ventricular assist provided by the LVAD with the natural control mechanisms of the body. For instance, increased venous return during exercise will increase preload and ventricular contractility due to the Frank-Starling mechanism. An increase in ventricular contractility leads to an increase in ΔRPM, which will cause the controller to increase the pump speed and flow in order to maintain the desired ΔRPM setpoint. Reduced perfusion demand would reduce contractility, causing the controller to reduce the pump speed and flow, preventing over pumping and suction. Accordingly, the control algorithm uses the body's own sympathetic and parasympathetic control mechanisms to match perfusion demand and avoid suction.

2.6.2 Comparison with Novel Physiological Controllers in Literature

Preload control has been proposed in the literature (e.g., [196, 197]). These systematic approaches have included direct measurements of preload (end diastolic pressure [196], end diastolic volume [197]), combined ventricular pressure and afterload

impedance estimation [198], or heart rate and aortic pressure estimations. [192] In these controllers, A single reference point can be sufficient in preventing ventricular suction and ensuring adequate perfusion in these controllers [199]. However, direct measurement requires pressure or ventricular volume sensors, which have low long-term reliability and drift [156, 157]. As a result, these sensors have not been chronically tested in vivo. In our study, even when a 5mmHg drift was introduced to the measurement, EDP control resulted in intermittent suction, *Figure 2-7*.

Based on the measurement of aortic pressure, Wu et al. attempted to achieve physiologic control by measuring only afterload [200]. The strategy of maintaining a reference mean aortic pressure provided adequate perfusion at rest and during exercise, but did not prevent suction because it does not allow for ventricular filling and causes suction (*Figure 2-6*, *Table 2-1*). Several control schemes have modified such control to account for both preload and after load (e.g. [201]and [198]).

Salamonsen et al. [202] have shown that the relationship between pump speed and pump speed pulsatility is linear when the aortic valve is closed. In partial support, this linearity is lost. Specifically, they chose flow pulsatility over pump speed pulsatility as a measure of preload because flow pulsatility maintained a more linear relationship during partial support. However, pump speed pulsatility is readily available whereas pump flow must be estimated. Furthermore, parametric, and model-based methods used to estimate pump flow are reported to be unreliable and inaccurate, as well as being susceptible to changes in blood viscosity [203].

2.6.3 Introduction of Pulsatility augmentation

Pulse flow modulation strategies have been proposed as a possible solution to the lack of pulsatility in CFLVAD flow regime. The advantages of CFLVADs use make reverting to older PFLVAD undesirable, and therefore modulating CFLVAD speed is a possible compromise to stop the adverse events associated with diminished pulsatility. Pulsatility augmentation can be performed either synchronously, or asynchronously. In synchronous pulse flow modulation, sensors have to be implanted to identify the cardiac timing in order to increase the pump flow in synchrony with the native heart ejection. The disadvantage of this method is 1) it requires sensor implantation or sophisticated ejection estimation algorithm, and 2) the pulsatility augmentation with synchronized flow modulation will inherently be limited because the peak pump flow in commercial CFLVAD is ~10 L/min, while the peak instantaneous flowrate in the healthy heart is ~30 L/min. Alternatively, asynchronous pulse modulation can provide higher levels of pulsatility, regardless of the heart state at a lower frequency.

Here, we show the feasibility of achieving pulse flow modulation using the ΔRPM algorithm. We also demonstrate its robustness with up to 3% and sudden decrease in preload (5x increase in PVR). The advantage of using ΔRPM as the control objective is that while it allows variation of the pump speed to induce arterial pulsatility, it provides inherent protection against ventricular suction and reduced end organ perfusion. Altogether, the ΔRPM control algorithm can simultaneously meet 3 goals 1) Provide physiological perfusion that is responsive to tissue demand, 2) prevent ventricular suction during reduced preload, and 3) augment arterial pulsatility to potentially prevent the adverse events associated with CFLVAD flow.

2.6.4 Advantages of the proposed Algorithm

In order for the proposed controller to perform adequately, it is essential to select an appropriate setpoint for the ΔRPM. Having a high ΔRPM setpoint may result in reduced perfusion, while a low ΔRPM setpoint may result in ventricular suction. In our simulations, however, we have demonstrated that the appropriate choice of a single ΔRPM setpoint can simultaneously meet both physiologic control and suction prevention objectives. As the control algorithm requires only measurement of pump speed, which is an intrinsic pump parameter, it is unnecessary to install unreliable pressure or flow sensors. Furthermore, it does not require frequent adjustments to setpoints (e.g., pump speed). Moreover, apriori estimation of pump models is not required, which eliminates errors arising from the patient's blood viscosity fluctuations or circadian variations. It is important to note that the proposed algorithm does not detect suction. Rather, it detects the approach of suction and reduces the pump speed accordingly. Additionally, the algorithm does not require any modifications to the design of blood pumps, and it can be readily incorporated into existing systems.

It is possible to measure the speed of the rotor using phase currents or hall effect sensors, which typically have a noise level of no more than 1%. In spite of up to 6% noise, the controller maintained physiologic perfusion, demonstrating its robustness (**Table 2-2**). The simplicity of the control structure is directly related to its control objective, which is based on pump speed pulsatility. When the differential pump speed is controlled, there are no limits to the mean pump speed, which ensures adequate pump flow and perfusion during rest and exercise or during vascular changes, provided that no suction is generated. Thus, the controller can cope with the temporal variations associated

with the cardiovascular system (for example, circadian variation and intra-patient variations). While pump speed pulsatility was used in this study, other intrinsic pump parameters that are sensitive to pressure head changes across the pump (e.g., changes in pump current) may also be used for physiologic control and suction prevention.

2.7   Alternative method to use pump speed pulsatility

In the previous sections, pump speed pulsatility was used directly and was quantified as the difference between the maximum and minimum pump speed over the past 2 seconds ($\Delta RPM = PS_{max} - PS_{min}|_{\Delta t=2s}$). Where PS is the pump speed in RPM. The limitation is that ΔRPM as calculated here is susceptible to noise spikes and measurement error. Alternatively, different quantifications of pulsatility can be used. To postulate that, an effective Suction Index (SI) that can be extracted from the noisy pump speed measurement is introduced. A 5-second moving window can be used to calculate the suction index as

$$SI = \frac{max\left[dPS/dt\right]}{mean[PS]}\Bigg|_{\Delta t=5s} \tag{9}$$

Similar to the ΔRPM control structure, the same control structure (equation 4) can be adapted to SI control using a gain scheduled PI controller, which enables the use of a

fixed control configuration, and it only needs selection of the controller coefficients and setpoints. The control equation becomes

$$I = K_p\big(\mathrm{SI}_{ref} - \mathrm{SI}_f\big) + \frac{K_p}{\tau}\int_0^t \big(\mathrm{SI}_{ref} - \mathrm{SI}_f\big)dt \qquad (10)$$

To illustrate the feasibility and versatility of pulsatility control, SI control was implemented in Heart Mate II axial flow pump. SI reference point was set to 0.8, $K_p = 0.55$, $\tau = 5$, and was tuned a priori with a direct numerical search approach. [204]

As shown in *Figure 2-13*, SI was extracted from the noisy pump measurement. The SI control variable was tested during rest and exercise with up to 8x-PVR, and during sudden transitions from rest to exercise. The control algorithm performed similar to *ΔRPM* control and augmented flow from 5.0 L/min during rest to 8.5 L/min during exercise as shown in *Table 2-3* which is slightly superior to ΔRPM . *Figure 2-14* demonstrated that the controller was able to prevent LV suction during a rapid eight-fold increase in PVR. The controller also effectively achieved rapid transitions from exercise to rest *Figure 2-15* without inducing suction.
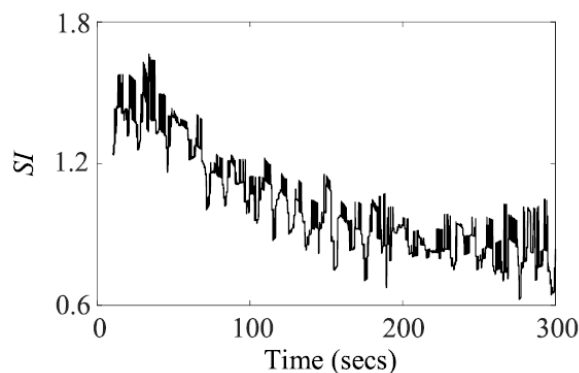
Figure 2-13 Published in [158] The suction index (SI) extracted from the noisy pump speed measurement. Under SI control, mean Suction Index is kept at 0.8 ± 0.2.

64

		LTO (L/min)	AoP (mmHg)	LVEDP (mmHg)	LVV (ml)	Suction
Rest	NH baseline	5.0	122/78	8	85/147	No
	FH baseline	3.7	96/63	16	181/229	No
	ΔRPM ctrl	5.0	104/100	5.6	40/65	No
	IS ctrl	5.0	104/100	5.4	36/63	No
Exercise	NH baseline	8.6	121/74	6.6	42/114	No
	FH baseline	6.7	95/58	20.1	178/234	No
	ΔRPM ctrl	8.0	108/104	7.4	58/94	
	SI ctrl	8.5	97/94	7.0	53/82	No
Rest,8x-PVR	ΔRPM ctrl	5.0	104/100	5.6	40/65	No
	SI ctrl	4.4	91/86	5.5	42/65	No
Exercise, 8x-PVR	ΔRPM ctrl	7.0	96/92	7.2	58/91	No
	SI ctrl	7.2	84/80	6.6	53/77	No

Table 2-3 Published in [158] Control outcomes during multiple test conditions comparing results from $\varDelta RPM$ and IS control. The results show comparable control outcome from both algorithms. **AoP**: Aortic pressure, **LVEDP**: Left ventricular end diastolic pressure, **LVV**: Left ventricular volume. **ΔRPM ctrl**: pump speed pulsatility control, **IS ctrl**: Suction Index control.
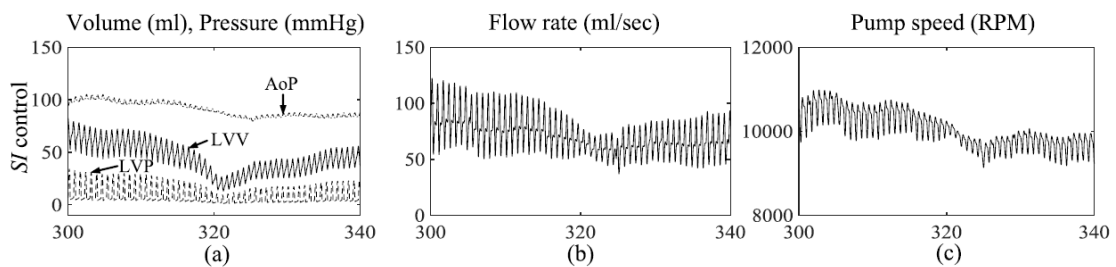
Figure 2-14 Published in [158] SI control performance during 8x-PVR. The rapid increase in PVR was initiated at t= 300s. The controller responded by quickly decreasing the pump current to maintain the set reference SI (SI = 0.8) and prevented ventricular

suction. **AoP**: Aortic pressure, **LVP**: Left ventricular pressure, **LVV**: Left ventricular volume.
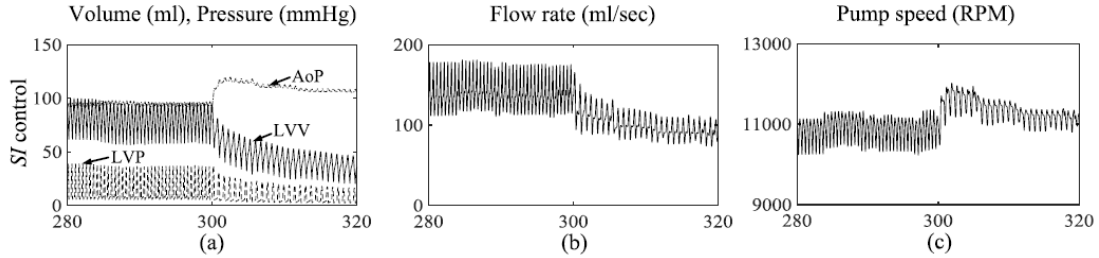
Figure 2-15 Published in [158] SI control performance during transition from exercise to rest. The transition was initiated at t = 300s. The algorithm adapted quickly, prevented suction, and provided adequate perfusion at rest. **AoP**: Aortic pressure, **LVP**: Left ventricular pressure, **LVV**: Left ventricular volume.

SI can be determined from noisy RPM measurements with a uniformly distributed noise of 2%, regardless of the physiologic conditions. As with the ΔRPM algorithm, SI control synchronizes the assist with the native ventricular function based on the native ventricular contraction. By way of example, increased preload and exercise leads to a higher ventricular contractility due to the Frank Starling mechanism. A higher ventricular contractility results in a higher $max\left[\frac{dPS}{dt}\right]$ and SI value. The SI pump controller will in turn increase the pump current and help match the perfusion demand.

These results show that sensorless control based on pump speed pulsatile response to reserve cardiac contractility can be harvested in multiple forms by extracting different features as was illustrated in ΔRPM and SI-based control.

2.8   Limitations

Pulsatile control requires the LVAD to respond to pressure head changes and maintain some degree of contractile reserve throughout a cardiac cycle. Even in patients with end-stage heart failure (~15-20% ejection fraction), the native cardiac contractility is sufficient to cause changes in pump speeds, as demonstrated in this study. However, the proposed controller will fail during ventricular asystole/fibrillation when ventricular contractility becomes negligible, and the heart rate falls. Low ΔRPM would result in the controller reducing the pump speed and flow below physiological levels. To mitigate this, a safe mode was implemented to maintain a constant pump speed in the event of left heart asystole to maintain pump flows at basal levels (heart failure baseline) and potentially sustain life while avoiding pump thrombosis and suction. The lack of ventricular contraction in asystole/fibrillation results in a low ΔRPM, which the controller responds to by reducing the RPM. However, even if the RPM value is at the lowest clinically recommended RPM of the pump, the ΔRPM value will not increase, as there is no effective contraction of the myocardium. To accomplish this, the safe mode operates at a clinically recommended minimum RPM to minimize the risk of pump thrombosis while ensuring ~3.7 L/min of flow, which is equivalent to the heart failure baseline to enable survival. Sensing is carried out by monitoring the pump mean speed and switching to a constant speed reference point when the mean pump speed falls below the threshold for long periods of time.

The lack of circulation to the lungs resulting from ventricular fibrillation and asystole will cause patient death if not reversed quickly, even if the LVAD was pumping. By ensuring that the lack of pump flow does not cause mortality, the safe mode keeps the

pump viable by preventing thrombosis in the event the patient is resuscitated. The performance of the proposed controller may diminish in the event of pump thrombosis and inflow/outflow cannula kinking which affects the dynamics of the LVAD and change the measured ΔRPM. It may be necessary for a clinician to adjust the RPM setpoint for physiologic control and suction prevention in these extenuating circumstances.

The lumped parameter circulatory system model used in this study has several limitations. Firstly, it assumes that blood is a Newtonian fluid, the heart valves are ideal valves (i.e., no regurgitation, no pressure drop, and instant closure), and gravitational effects are not accounted for. Additionally, baroreceptor and neurohumoral responses cannot be replicated by the model. On the other hand, this previously validated circulatory system model demonstrated the feasibility of the *ΔRPM* control algorithm for physiologic perfusion and suction prevention. A mock flow loop and large animal studies are required to validate the controller's performance and demonstrate its long-term safety, efficacy, and reliability.

Lastly, the proposed *ΔRPM* algorithm was able to augment arterial pulse pressure from ~98/92 to 115/85 at rest, at a frequency of ~10 beats per minute. The exact pulse flow modulation strategy that is able to alleviate adverse events associated with diminished pulsatility is still unknown. The vascular endothelium is in constant contact with blood flow and responds to alterations in blood flow hemodynamics such as shear stress, pulse pressure, and stretch. Moreover, arterial vascular wall contains smooth muscle cells that regulate the vascular tone. While in this chapter, the advantages of *ΔRPM* control algorithm was demonstrated, and it was extended to safely augment vascular pulsatility. However, without knowing the arterial flow waveform that can

potentially normalize the vascular phenotype, it remains less used. In the following chapter, an in-vitro culture model of the arterial blood vessel is proposed as a platform for investigating and optimizing pulse flow modulation strategies to improve adverse events associated with CFLVADs' diminished pulsatility.

2.9 Conclusion

A sensorless control algorithm was developed for continuous flow ventricular assist device to provide physiologic perfusion, prevent ventricular suction and augment arterial pulsatility through pulse flow modulation. The proposed algorithm requires only the measurement of intrinsic pump speed, eliminating the need for implantable sensors or model-based estimation methods. The in-silico results demonstrated feasibility and robustness of the proposed sensorless control algorithm over a wide range of clinical test conditions and measurement noise levels. The proposed control algorithm does not require any pump design modifications and may be readily incorporated into existing blood pumps. Control based on native reserve contractility showed its versatility in being extended to augment arterial pulsatility in addition to extracting different measures of pulsatility such as a suction index from noisy pump speed signal.

CHAPTER 3: ASSESSMENT OF PULSE FLOW MODULATION USING AN INVITRO MODEL OF THE ARTERIAL WALL

3.1 Effects of Flow Hemodynamics on ECs and SMCs

The blood vessel is an active multilayered barrier that consists of the inner endothelial cells (ECs), which are enveloped by smooth muscle cells (SMCs). EC layer is in constant contact with the inner blood flow and thus reacts to mechanical forces generated by the pulsatile flow through the vessel lumen. ECs communicate stimulations such as shear stresses, pressure, and stretch forces by the release of bioactive molecules to promote or repress vasodilation, inflammation, tissue remodeling, proliferation, apoptosis and cell migration (e.g. [18-20]). Hence, pathological flow conditions can trigger adverse adaptation and remodeling by the vasculature. EC adaptation to the mechanical environment has been previously examined in literature by using *in-vitro* cell cultures of ECs usually within a parallel flow plate in the absence of SMCs.

In vivo, however, ECs are not isolated and can actively communicate these changes with surrounding interstitium and SMCs. Indeed, some growth factors are secreted by both EC and SMC and can act on both cell lines such as transferring growth factor (TGF-β) and platelet derived growth factor (PDGF) [205]. EC and SMC can communicate by

cell-cell contact as well as through soluble components. Few *in-vitro* models incorporated cocultures (e.g., [206-210]). Typically, ECs and SMCs are either cultured on both sides of a porous membrane, directly cultured over each other with ECs on top, or have SMCs embedded in a collagen matrix. However, these studies do not accurately replicate the physiologic mechanical environment and have mostly shown the response of EC-SMC coculture to singular mechanical stimulation namely either stretch, shear stress, or cyclic frequency.

In-vitro study of vascular alterations during CFLVAD support is a multifactorial problem involving pulse rate, stretch, and shear stress effects. The effect of shear stress on endothelial cells (EC) morphology has been shown in previous studies [211-213] where the cells are elongated, larger in size and oriented with the direction of the flow in areas of high shear stress, while more polygonal-shaped and randomly oriented phenotypes can be seen in areas of low shear stress areas such as bifurcations. However, the cellular level changes go beyond morphology; low shear stresses have been related to increased oxidative stress, changes in cellular growth rate, higher expression of proinflammatory adhesion molecules and the production of biologically active molecules [18, 19]. Elevated continuous and pulsatile shear stresses, on the other hand, can cause vasodilation by upregulating nitric oxide synthase, and super oxide dismutase which can induce endothelial dysfunction[214, 215]. Moreover, chronic goats studies using CFLVADs have shown reduced vasoconstrictive response to norepinephrine, thinner vessel walls, and smooth muscle cell (SMC) atrophy [216]. The alignment of EC and smooth muscle cells (SMCs) is also affected by frequency of the cyclic stretch. The cyclic stretch of SMCs cultured on a flexible membrane significantly increased the

portion of cells aligned in the longitudinal direction (75°-90°) with the radial direction [217]. The study also showed that this frequency-dependent alignment could be regulated through Integrin-ß1, p38 MAPK, and the actin filament polymerization system.

3.2   Effects of CFLVAD flow on the vasculature

CFLVADs have emerged as a standard therapy for end stage heart failure due to a shortage of donor organs. Clinically, CFLVADs are predominantly used over pulsatile flow devices, because of their higher reliability, energy efficiency, smaller size and simpler implantation procedure. [218] However, diminished pulsatility in long-term CFLVAD support has been associated with abnormal physiologic profile of myocardial and vascular energy utilization, gastrointestinal (GI) bleeding, hemorrhagic strokes, arteriovenous malformations (AVMs), valve fusion, and end organ failure. [148, 149] The formation of AVMs indicates an increase in vasculogenic activity, and the endothelial dysfunction associated with diminished pulsatility is thought to be a result of activation of Nrf-2 mediated antioxidant response and production of inflammatory and proangiogenic cytokines. [219] The bleeding events are associated with Von Willebrand Factor (we) degradation due to high shear stresses, mostly occurring at the pump. [220] Interestingly, this takes place in both PFLVADs and CFLVADs. However, low shear stresses during CFLVAD support and the subsequent low vow production thereof has been attributed to the higher rates of GI bleeding under CFLVAD support compared to PFLVAD support. [220, 221]

3.3   State of *In-vitro* Vascular Modeling from Literature

Large animal models fail to capture many of the complications observed in CFLVAD patients due to anatomical and physiological differences – animals are usually healthy

and are young, while VAD patients are typically older with chronic disease. [222]

Clinical studies are highly relevant but are not tightly controlled as patients typically have

confounding factors. Thus, study of cellular level vascular adaptations in both EC and

SMC in a physiologic cell culture model is ideal as it is highly controlled and largely

devoid of confounding factors. Given limitations with large animal models,

physiologically relevant *in-vitro* models of the human arteries may provide the best

opportunity to evaluate the effects of diminished pulsatility as seen in patients with

CFLVADs

The conditions used in most *in-vitro* systems poorly represented the physiologic

conditions in the arterial system where either continuous or sinusoidal flow waveforms

were used, and mechanical cyclic stretch was either not incorporated or introduced

uniaxially to the membrane upon which the cells were cultured [205, 214, 223]. These

conditions fail to replicate the flow shear stresses and pressure-related deflection of blood

vessels. *In vivo*, EC are not isolated and can actively communicate these changes with

surrounding interstitium and smooth muscle cells (SMC). Some growth factors are

secreted by both EC and SMC and can act on both cell lines such as transferring growth

factor (TGF-β) and platelet derived growth factor (PDGF) [205]. EC and SMC can

communicate by cell-cell contact as well as through soluble components. However, fewer

invitro models incorporated cocultures (e.g., [206-210]). Typically, ECs and SMCs are

either cultured on both sides of a porous membrane, directly cultured over each other

with ECs on top, or have SMCs embedded in a collagen matrix. However, these studies

lacked some aspect of the physiologic mechanical environment and have mostly shown

the response of EC-SMC coculture to singular mechanical stimulation namely either stretch, shear stress, or cyclic frequency.

In literature, few groups were able to achieve accurate replication of physiologic flow exposure conditions. ***Table 3-1*** and ***Figure 3-1*** provide a summary of some of the notable coculture models. Robert et al [208] used human vascular cells to engineer a 3D artery model mimicking the structural as well as functional characteristics of the native artery. While, their model is realistic, the pulsatile flow exposure was not physiologic, and the setup and seeding are lengthy and complex which may hinder its future use. Zhou et al [224] cultured ECs and SMCs on both sides of a porous membrane in a transwell cell culture insert. Their coculture model however used sinusoidal flow to simulate cyclic shear stress with a minimum shear stress > 0 dyne/ cm^2. Van Engeland et al. [209] created a microfluidic arterial model composed of a suspended porous membrane separating a monolayer of SMC and EC. The flow was steady and laminar and cyclic stretch was introduced directly to the membrane itself. While the model includes two modes of mechanical stimulation, the flow is continuous, and the shear stress is almost constant with a very low Womersley number. Further, the stretch is applied uniaxially and the membrane deflection is minimum and cannot mimic the distention geometry of in vivo artery. Elliott et al [206] used an EC monolayer culture over a collagen-SMC construct and was subjected to pulsatile flow under physiologically relevant shear stresses. However, the coculture was not subjected to cyclic strain and was seeded over a stiff glass slide.
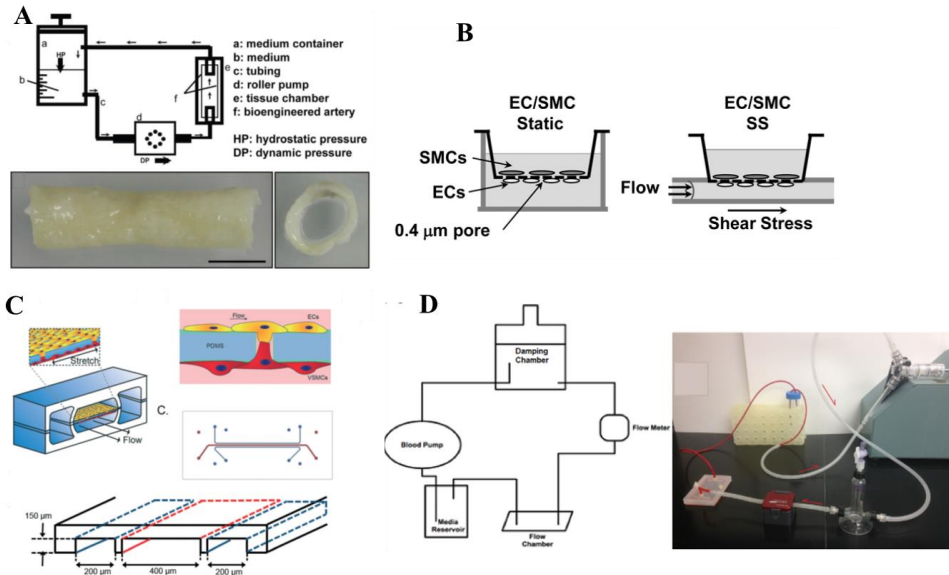
Figure 3-1 Four most relevant *in-vitro* vascular models from Literature. **A-** adapted from Robert et al. [208] The system consists of a 3D tubular scaffold that is cultured with ECs and fibroblasts. Flow is introduced through the lumen of the tube and circulated using a peristaltic pump, **B-** Culture system developed by Zhou et al. [224] ECs and SMCs are cultured on both sides of a porous membrane and constant flow is introduced to the bottom of the plate where the ECs are cultured. **C-** system developed by Van Engeland et al. [209] The study used a microfluidic vessel wall on a chip. The device consisted of two vacuum chambers and a cell culture chamber. ECs and SMCs were cultured on both sides of a porous PDMS membrane with flow running on the upper and lower culture chamber. The vacuum chambers were used to cyclically stretch the porous membrane, **D-** Adapted from Elliott et al. [206] A Pulsatile flow loop was externally connected to a stiff, glass micro culture chamber. ECs and SMCs were culture on both sides of porous membrane resting on the glass bottom and subjected pulsatile flow.

	Description	Limitations
Robert et al [208]	Biodegradable 3D tubular scaffold seeded with ECs and fibroblasts	Non-physiologic flow pulsatility, no flow or pressure measurements, and no SMCs seeding.

Zhou et al [224]	ECs and SMCs cultured on both sides of a porous membrane in a parallel plate flow subjected to pulsatile or steady flow	Non-physiologic sinusoidal flow and pressures, stiff glass bottom and stretch.
Van Engeland et al [209]	ECs and SMCs cultured on both sides of a porous membrane; cyclic stretch introduced uniaxially to the membrane	Very low flow pulsatility, non-physiologic stretch and pressures.
Elliott et al [206]	ECs and SMCs culture on both sides of a porous membrane subjected to a pulsatile flow loop.	Cultured on a stiff glass slide, thus no stretch, no pressure measurement.

Table 3-1 Comparison of the most relevant coculture vascular models from literature with their description and limitations.

3.4   Study goal and hypothesis:

While flow modulation has been proposed as an alternative to true pulsatile flow, validation of these strategies is complicated. Physical aspects like Pulse Pressure (PP), Energy Equivalent Pressure (EEP), and Surplus Hemodynamic Energy (SHE) can be validated using computer simulations or mock flow loops. However, evaluation of the effect of artificial pulsatility on cells, tissues, and organs that make up the circulatory system require cellular or animal studies. There are obvious limitations to current *in-vitro* models of the arteries that pose limitations on our ability to study the effects of CFLVAD flow on the vasculature. [225] In order to study these strategies preclinically, the effects of each element of the pulsatile waveform needs to be assessed in a physiologically relevant model.

We have previously developed an endothelial cell culture model that can better replicate physiological mechanical environment of the vasculature [226, 227]. In the present study, we expand on this model and develop an endothelial-smooth muscle cell

coculture model to evaluate the effects of flow pulsatility as well as pulsatile frequency on ECs and SMCs organization, size, and alignment.

3.5 Study Hypothesis

We hypothesize that artificial pulse frequency, stretch, and shear stresses in the arterial vasculature all play an important role in the regulation of vascular response for both ECs and SMCs and may be target parameters for the optimization of pulsatile control strategies for both PFLVADs and CFLVADs.

3.6 EC-SMC Coculture Model Components:

3.6.1 System Layout

With the clear shortcomings of *in-vitro* vascular models discussed, we developed a direct Endothelial Cell- Smooth Muscle Cell coculture model. The platform shown in *Figure 3-2* (A) consists of a PDMS rectangular channel with a suspended flexible polymeric 500μm thin membrane of elasticity matching that of human aorta (Youngs Modulus~ 500 kPa). Under pressurized flow, the membrane will distend to create a segment of a blood vessel. Human aortic endothelial cells (ECs) were cocultured with SMC on the polymeric film. A pulsatile flow pump (Model 1407, Harvard Apparatus, Holliston, MA) with adjustable frequency and stroke volume is used to produce pulsatile flow. One-way valves were used to ensure unidirectional flow. A tunable flow resistance mimics the systemic vascular resistance, and a tunable compliance element represents arterial compliance. Complete cell culture media was used as the working fluid during experimentation. The compliance element, flow resistance, pump stroke volume, and

pulsatile pump frequency can be adjusted to create the desired flow conditions as previously discussed in [226, 228].
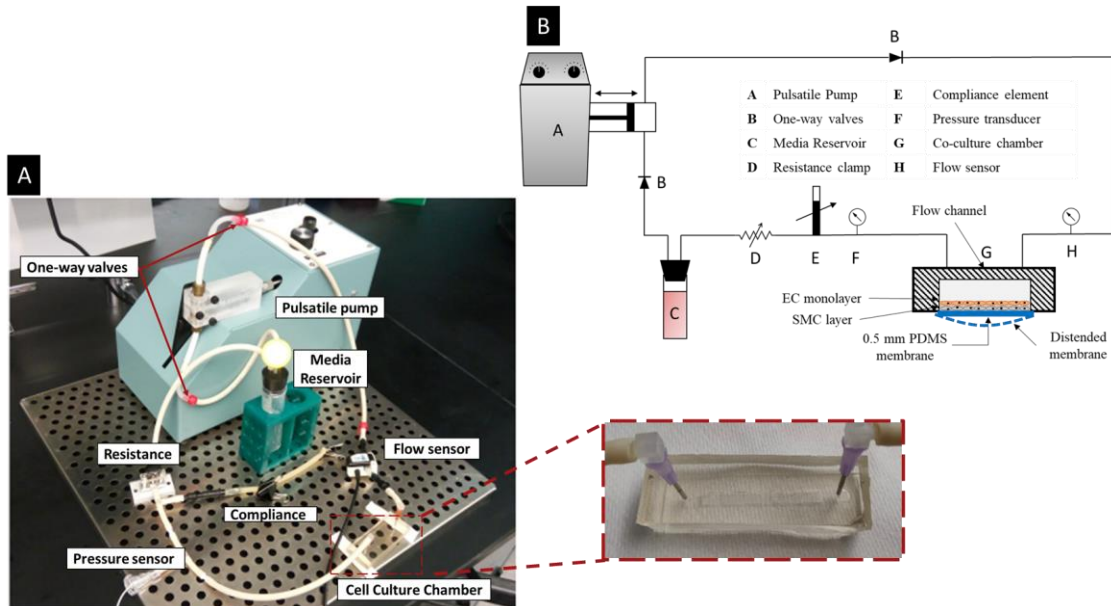
Figure 3-2 A- coculture model loop setup showing the external flow loop connected to the flow channel inlet and outlet to generate tunable flow and pressure waveforms. The magnified view shows details of the PDMS Coculture channel connected to the inlet and outlet of the miniaturized mock flow loop, B- Schematic representation of the Coculture model.

3.6.2 Experimental Design

The effects of pulsatility and pulsatile frequency on EC and SMC were evaluated during: (1) normal pulsatile flow (120/80 pulse pressure and 60 bpm), (2) low cyclic frequency (115/80 pulse pressure and 30 bpm) and (3) diminished pulsatility during CFLVAD support (98/92 pulse pressure and 60 bpm). ECs and SMCs were directly cultured on a flexible, thin membrane where it was subjected to the three flow regimes. The flow conditions were modulated so that the mean arterial pressure and the average

flowrates in all three cases were 95 ± 1 mmHg and 10.1 ± 0.5 ml/min. This ensured that any effects seen on cell size and morphology are due to pulse frequency, and flow/pressure pulse modulations. Cell morphology was assessed using fluorescent microscopy and shear stresses were calculated by simulating the flow chamber using CFD software under different conditions. Details are presented next.

3.6.3 EC-SMC Co-culture Chamber Fabrication

First, the PDMS flow channel was created using standard soft lithography as described previously in [226] and had a height, width, and length 0.3 mm, 5 mm, and 25 mm, respectively with an inlet and outlet ports on top. The final cell culture chamber was fabricated by irreversibly bonding a thin membrane of PDMS (500 µm) to a rectangular PDMS chamber using oxygen plasma bonding. Inlet and outlet ports were connected through the top holes to create a continuous recirculation of the culture medium.

3.6.4 Cell Culture

Human Aortic Smooth Muscle Cells (HASMCs) and Human Aortic Endothelial Cells (HAECs) (ATCC, Manassas, VA, and Invitrogen, Carlsbad, CA) were initially cultured and maintained according to the supplier's instructions in standard tissue culture flasks. Prior to seeding within the cell culture chamber in the ECCM, the surface of the cell culture chamber was treated with 50 mg/mL of a solution containing a mixture of attachment factor, gelatin, and fibronectin for 12 h at 4 °C and for 1 hr. at 37 °C to promote cell adhesion. Cells were stained with 15mM cell tracker (Invitrogen, Carlsbad, CA) blue for SMCs, and red for HAECs. The cell culture chamber was first washed with culture medium (M-200, with the addition of low serum growth supplement, Invitrogen, Carlsbad, CA). SMCs were seeded at a density of 5×10^5 cells/mL. Cells were

79

incubated at 37 ˚C in a humidified atmosphere containing 5% (v/v) CO_2. After 48 hours, the culture chamber was washed and coated with 50 mg/mL fibronectin for 3 hours at 37 °C and was washed with cell culture medium and seeded HAECs at a density of 5×10^5 cells/mL, cells were allowed to attach and spread for 4 hours, after that the medium was replaced and maintained in culture until they reached confluence. Once they reached confluence, they were assembled in the flow loop and subject to different pulsatile and flow conditions (24 hours) to analyze the cell growth and alignment under fluorescent microscope. To do that, SMC and HAEC were stained with cell tracker red and blue (Thermo Fisher Scientific, Waltham, MA), to achieve live imaging and visualize the cell growth and alignment. Average cell size was calculated on 10 cells for each condition using image J software (NIH, Maryland, USA).

3.6.5 Pressure and flow measurement

Pressure and flow measurements were accomplished using inline pressure and flow sensors (Millar Instruments, TX and Transonic Inc., NY). Laser-induced fluorescence (LIF) was used to track the membrane deflection under applied pressure using an imaging setup also described in [226]. Shear stress measurements utilized the flow data in conjunction with change in channel cross-section following application of pressure.

3.6.6 Shear Stress Calculation

Formulae developed to calculate shear stress from flow conditions are based on a rigid rectangular flow chamber geometry. To establish a more accurate numerical calculation of the shear stress on the flexible membrane for each flow condition, a three-dimensional Computational Fluid Dynamic (CFD) simulation of the flow chamber was performed using finite element analysis (ANSYS-CFX, Canonsburg, PA). The membrane

deflection was calculated using LIF under different fluid pressures. *Figure 3-3* shows a plot of the membrane deflection at the centerline of the membrane versus the flow chamber pressure. This relation was used to calculate the membrane's new curvature at different pressures during the CFD simulation. The dimensions of the flow chamber ensure a predominantly circumferential strain in the membrane except near the inlet and outlet. For CFD simulation and to negate entrance effects, only the fully developed section of the channel was considered for the shear stress calculation. The hydrodynamic entrance length was calculated as

$$L = 0.05 R_e D_h \tag{9}$$

Where L is the entrance length, R_e, is Reynolds number, and D_h is the hydraulic diameter. The CFD solver uses the three-dimensional conservation of mass and momentum equation, coupled with a turbulence model solver. $k-\omega$ turbulence model was used for the Reynolds Averaged Navier Stokes equation ($RANS$) to provide mathematical closure to the equations of motion. 14 discrete flow points were simulated for each pulsatile mode. The flow channel dimensions were updated using the relation from *Figure 3-3* for each flow point.

Adequate meshing was achieved using ANSYS built in mapped mesh and sweep method over the length of the flow chamber thus controlling the number of elements in the width direction and along the flow direction. A mesh independence analysis was carried out to obtain a mesh that provides accuracy with minimum computational effort. The mesh element size was changed in all three axes until an acceptable stability of solution was obtained at 157500 elements.

3.6.7 Statistical Analysis and data processing

Data was collected using PowerLab 30 (ADInstruments, Dunedin, New Zealand). Calculations, filtering, and analysis were done using MATLAB (MathWorks, Natick, MA, USA). One Way ANOVA in Minitab software (Minitab LLC, State College, PA) was used to compare the cell size among different experimental group with a confidence interval of 95%.

$$d=-2E-05\times P^2+0.005\times P$$
$$R^2 = 0.9922$$
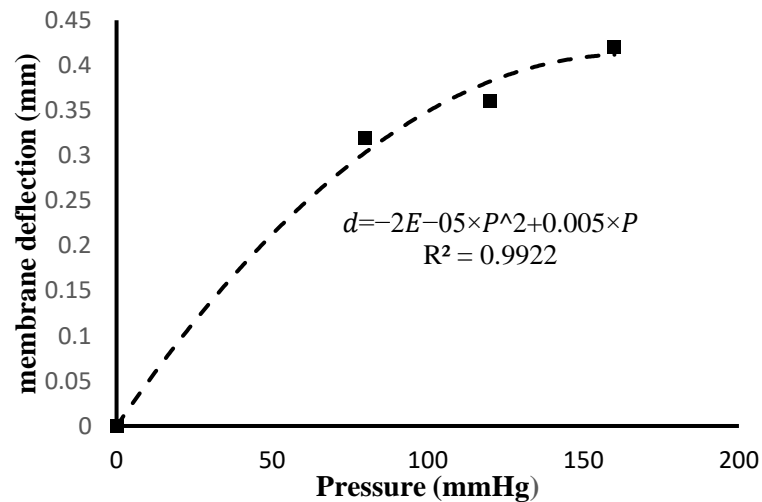
Figure 3-3 PDMS membrane deflection obtained as a function of flow channel pressure using Laser Induced Fluorescence imaging of the culture membrane.

3.7 Results

3.7.1 Emulation of different flow conditions within the culture chamber

The cell culture chamber had a rectangular shape with 0.3 mm height, 5 mm width and 25 mm length. Normal flow pressures were 120/80 mmHg (max/min) and at a frequency of 60 ± 5 bpm, . CFLVAD flow replication pressures were 98/92 at a frequency of 60 ± 5 beats per minute. CFLVAD flow modulation condition pressures were 115/80 mmHg at a frequency of 30 ± 5 bpm as shown in *Figure 3-4*. All three pressure and flowrate waveforms were adjusted to maintain a mean pressure of 95 ± 1 mmHg and a mean flowrate

of 10.1 ± 0.5 ml/min. Mean arterial pressure (MAP), Energy Equivalent Pressure (EEP), and Surplus Hemodynamic Energy (SHE) were calculated from the flow regimes as shown in *Table 3-2*.

	Normal pulsatile flow	Diminished pulsatility	Low cyclic frequency
Mean Arterial pressure (mmHg)	95 ± 1 mmHg	95 ± 1 mmHg	95 ± 1 mmHg
Mean flow rate (mL/min)	10.1 ± 0.5	10.1 ± 0.5	10.1 ± 0.5
Energy Equivalent Pressure (mmHg)	100±2	95±2	98±2
Surplus Hemodynamic Energy (erg/cm³)	6828±158	153.8±25	5156±149

Table 3-2 Calculated pulsatility measurements for each condition studied. The mean flow rate and mean arterial pressure was maintained constant for all three conditions. SHE was lowest in diminished pulsatility conditions, while low cyclic frequency showed close to normal, SHE.

3.7.2 Estimation of shear stress inside the coculture chamber

Shear stress distribution confirmed a laminar flow with maximum shear near the central axis of the membrane and minimum shear stresses towards the periphery, as shown in *Figure 3-5.* To confirm the accuracy of the simulation results, shear stresses were also calculated analytically for the three conditions using the approximate analytical relation:

$$\tau = {\alpha}/{\sqrt{2}} \times {6Q\mu}/{h^2 w} \tag{10}$$

Where Q is the volume flow rate, h and w the height and width of the channel

respectively. α is the Wormsley parameter which arises in the solution of Navier Stokes
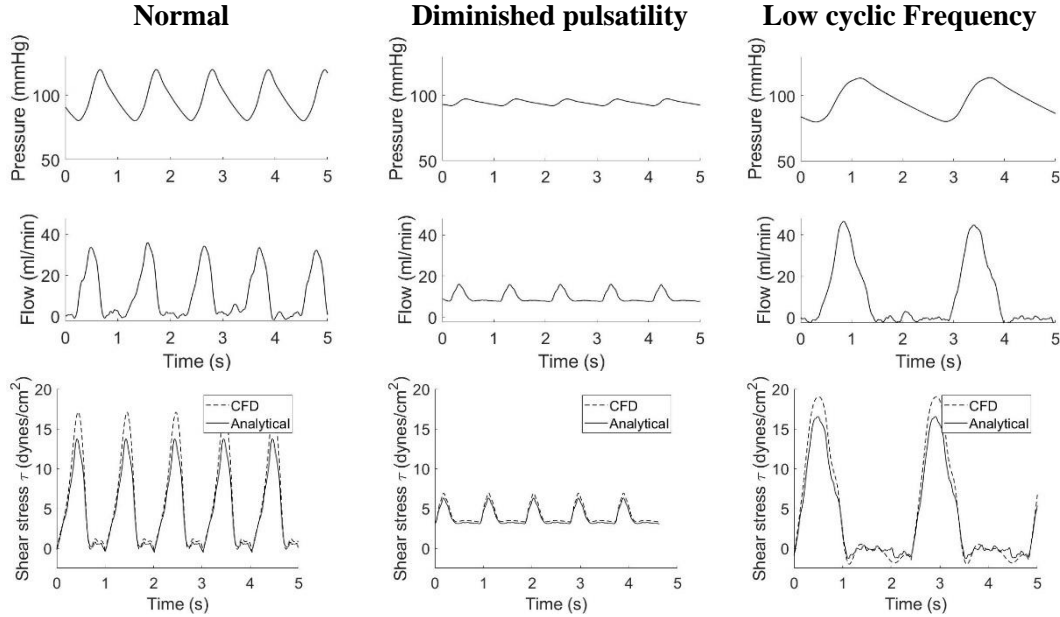
Figure 3-4 Pressure, flowrate, and estimated shear stress waveforms are shown

for each condition. The reduced pulse pressure and peak flowrate and shear stress

is clearly seen with diminished pulsatility. The average flowrate and average

shear stresses were kept equivalent between all conditions

equations for pulsatile flow and was determined to evaluate the ratio of pulsatile

flow frequency to viscous effect using the following equation:

$$\alpha = \frac{1}{2} D_h \sqrt{\frac{2\pi f \rho}{\mu}} \qquad (11)$$

where ρ is the culture media density, f is the flow pulse frequency, D_h is the

hydraulic diameter, and μ is the culture media viscosity. The average shear stress for all

conditions was within $4.2 \pm 0.5 \; dyne/cm^2$. The resulting flow waveforms, pressure

waveforms, simulated shear stress, and analytically approximated shear stress are shown in *Figure 3-4*. The shear stress varied between -0.12 and $17.09\ dyne/cm^2$ for normal flow condition, 3.39 and $6.94\ dyne/cm^2$ for diminished pulsatility condition and $-2\ and\ 19.06\ dyne/cm^2$ for CFLVAD flow modulation condition.
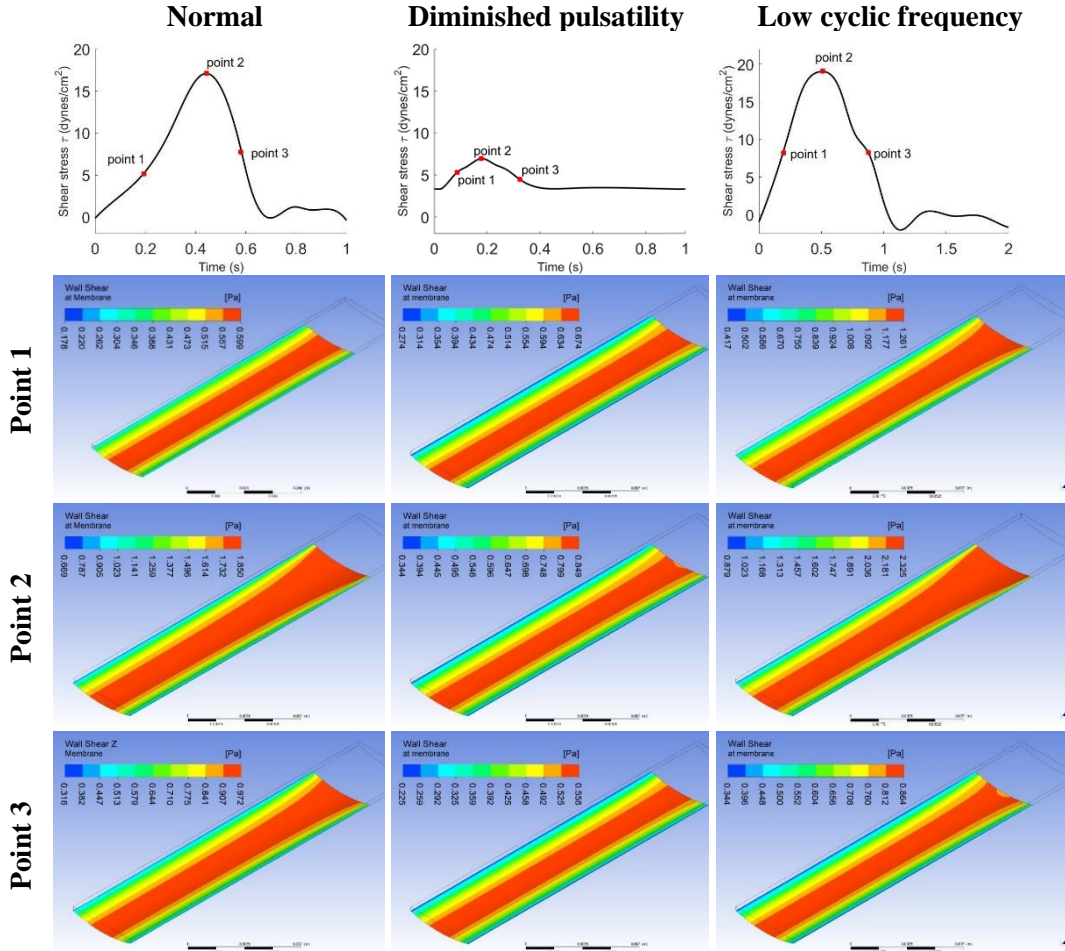
Figure 3-5 Simulated wall shear stress is shown at 3 distinct time points on a representative flow pulse for each condition, as shown in the top panel. The peak shear stress is lowest with diminished pulsatility condition, while the peak shear stress is slightly higher for low cyclic frequency (30 bpm, 2 seconds cycle time) compared to normal pulsatile (60 bpm, 1 second cycle time).

3.7.1 Assessment of HAEC and SMC morphology and alignment

Fluorescent probing with cell tracker blue and cell tracker red for SMC and HAEC respectively is shown in **Figure 3-6**. Microscopic analysis revealed change in cell size between normal pulsatile flow, low frequency flow modulation support, and diminished pulsatility with CFLVAD support (Fig.6). Compared to normal pulsatile conditions, diminished pulsatility during CFLVAD support (CFLVAD flow replication) showed a statistically significant reduction in HAEC size ($p < 0.01$). Low frequency flow modulation support did not lead to a statistically significant reduction in EC cell size, suggesting that the decreased frequency with flow modulation had no to minimal effect on EC size. Statistically significant differences in SMC size were observed during low frequency flow modulation (31%, $p < 0.01$) and diminished pulsatility with CFLVAD support flow (55%, $p < 0.01$).
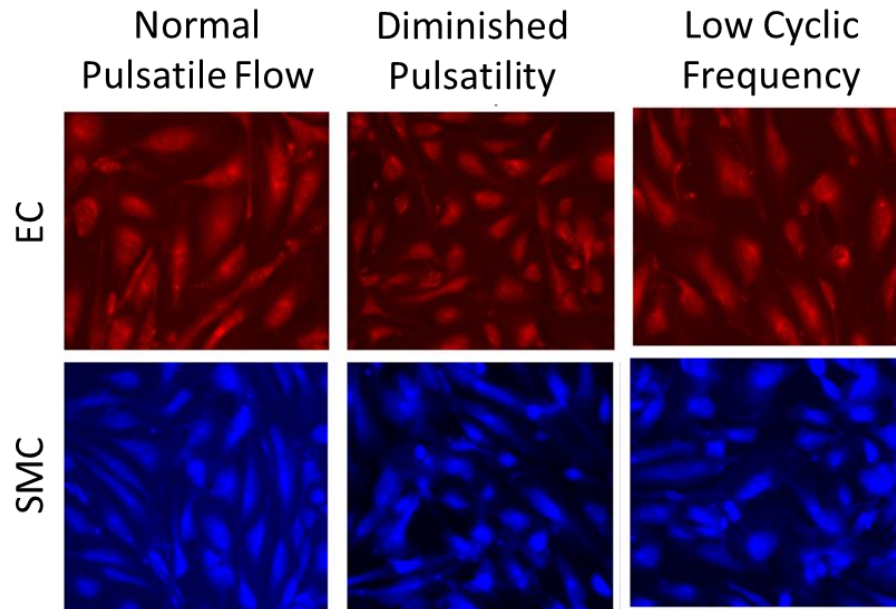
Figure 3-6 Live imaging of ECs and SMCs using fluorescent staining. The aligned morphology of ECs and SMCs in seen in with low cyclic frequency and normal pulsatility conditions, while a disrupted alignment and smaller cell size is seen in diminished pulsatility condition.
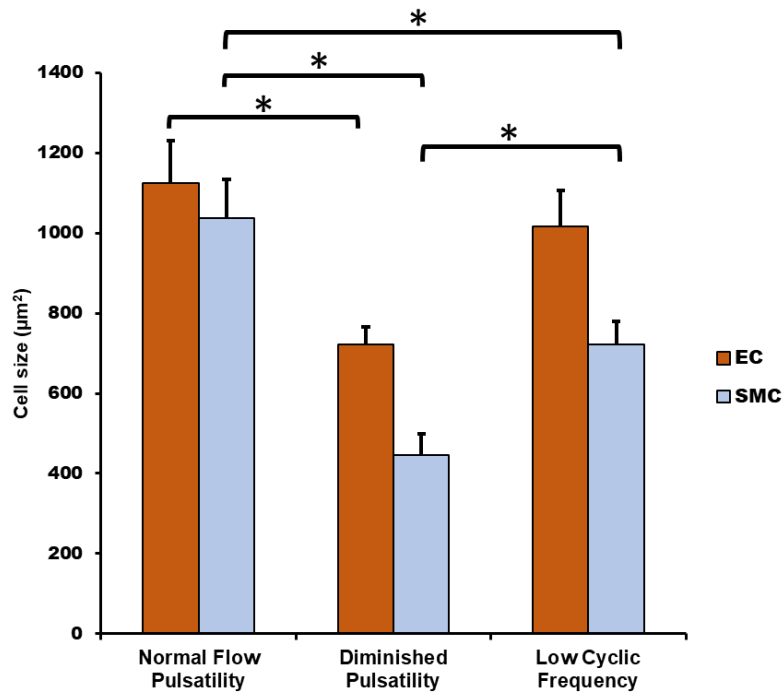
Figure 3-7 Cell size assessment of simulated conditions. ECs and SMCs size were significantly reduced with diminished pulsatility. Low cyclic frequency maintained normal EC size (p=0.07) while SMC size was significantly reduced (* p < 0.001).

3.8 Discussion

3.8.1 EC-SMC coculture model as a platform to study effects of vascular pulsatility

Experimental models of blood vessels are desirable for studying vascular physiology and pathophysiology. The ability to adequately model the arterial wall can provide new insights into vascular function, elucidate details molecular signaling pathways, and predict drug response. Historically, *in-vivo* small, and large animal models have been instrumental in developing of our understanding of vascular biology. However, the differences between human and animal vascular biology limit the interpretability of

animal experiments and threatens the translatability of such models' response to drugs and therapies.

Here, we developed a direct EC-SMC coculture model of the arterial wall that is able to replicate the hemodynamics of large arteries include pressures, shear stress, and stretch. The use of both ECs and SMCs is critical for accurate for vascular modeling. Blood vessels are complex in nature. The inner endothelial wall is surrounded by smooth muscles and connective tissue. The surrounding biomechanical environment, that is shear stress, mechanical strain, pulse flow, and pulse frequency all play critical roles in the maintenance of ECs and SMC morphology, phenotype, and function. [52, 229, 230] Therefore, the accurate replication of this mechanical environment is indispensable when building *in-vitro* models for human vasculature. Our results demonstrate the physiological relevance of the EC-SMC co-culture model to replicate hemodynamic conditions within the vasculature. The arterial pressure was 120/80 mmHg for normal pulsatile flow, 98/92 mmHg with CFVAD support, and 115/80 mmHg with flow modulation, which correspond to clinically observed values of systolic and diastolic arterial pressures. [231] The mean pressure and mean flowrate were maintained at 95 ± 1 mmHg and 10.1 ± 0.5 ml/min respectively for all groups. The flow was scaled down in the cell culture model loop to ensure physiologic values of shear stress in the cell culture model (average shear stress = $4.2 \pm 0.5 \; dyne/cm^2$) [232]. The peak shear stresses are higher ($15 \pm 2 \; dyne/cm^2$) in both normal pulsatile flow and flow modulation (low cyclic frequency) conditions. In this setup, the coculture culture model represents a 5 mm circumferential section of the aortic wall (~ 1/5th of a human aorta) and accurately mimics SHE on the simulated vascular section ~1/5th physiological values).

Importantly, the SHE is diminished by ~98% with CFLVAD support when compared to normal pulsatile flow, which is in agreement with clinical results, [233]. Flow modulation, even at a lower frequency, significantly augments SHE. Importantly, the EC-SMC co-culture model has a confluent layer of endothelial cells between the SMC and fluid, which enables the communication and shared signaling pathways between ECs and SMCs that contribute towards the development, maintenance, regulation, and remodeling of the vasculature under normal and pathological conditions.

3.8.2 Limitations to pulse flow modulation strategies

Clinical complications associated with CFLVADs have renewed efforts to attain pulsatile flow with CFLVADs. Rather than reverting to pulsatile flow VADs that are bulky, less efficient and less reliable; recent efforts have focused on generating pulsatility using CFVADs via an approach called 'flow modulation' (i.e.) rapid changes in pump speed (HeartWare HVAD or Heartmate III).[234, 235] Flow modulation can be accomplished in two ways: (1) Synchronous Flow Modulation: where changes in pump speed are accomplished in synchrony with native myocardial contractions.[236-238] The only variable that can be modulated is the pulse pressure. Unlike the native ventricle, which can generate peak flows of 30-40 L/min, CFLVADs are limited to peak flow rates of approximately 10 L/min, which limits the pulse pressure that can be generated with synchronous flow modulation to < 20 mmHg. Significantly, long-term sensors are necessary to monitor native heart rate to detect onset of ventricular systole to synchronize the frequency of pump speed changes, and (2) Asynchronous Flow Modulation: where changes in pump speed are accomplished independent of the native heart rate.[239, 240] Both pulse pressure and frequency can be modulated to achieve desired levels of

pulsatility. In terms of implementation, asynchronous flow modulation is simpler, as long-term sensors are not required to synchronize to the native heart and multiple variables (pulse pressure and frequency) can be changed. Asynchronous modulation at lower VAD flow modulation rates ($\leq$ 30 bpm) can generate near physiological pulse pressures (~35-40 mmHg) even with peak CFLVAD flow rates limited to 10 L/min.

3.8.3 Effects of low cyclical flow pulsatility on EC and SMC size and morphology

This study demonstrated that diminished pulsatility, characteristic of CFLVAD support results in significant morphological changes of both EC and SMC, resulting in cell size reduction compared to normal pulsatility. This reaffirms the important role of pulsatility in maintaining normal vascular function and tone. In our study flow modulation that restored pulsatility to 35 mmHg or higher, even at much lower frequencies compared to normal cardiac rhythm, was able to substantially normalize EC morphology, as evidenced by improved cellular alignment and maintenance of EC cell size. Changes in pulsatility primarily impact arterial vessels, where ECs are the primary mechano-transducers. Non-surgical bleeding events occur downstream of large vessels in arterioles, venules, and capillaries. While there is no established causal relationship tying pro- inflammatory/pro-angiogenic factors in large vessels to non-surgical bleeds, loss of pulsatility-mediated endothelial dysfunction and cytokine production is suspected to be the cause of downstream microvascular dysfunction that leads to non-surgical bleeds. This is based on published reports that found angiopoietin-2 (Angpt-2) levels to be significantly higher in CFLVAD patients with non-surgical bleeding events than in patients with heart failure or orthotropic heart transplants.[241-243] Additionally, various inflammatory cytokines including IL-6, IL-8, TNFα and IL-1β were also found to be

acutely elevated following CFLVAD implantation with levels of IL-6 and IL-8 remaining

elevated even after 6 months of implantation.[244] Review of literature associated with

AVMs and bleeding events in general suggests elevated levels of cytokines associated

with inflammation, vascular instability and vascular permeability including IL-1β, IL-6,

IL-8, TNF-α, HIF-1, NF-kB, VEGF, MMP-9 and decreased TIMP levels.[245-252].

Furthermore, ECs from older individuals under CF-VAD flow results in elevated levels

of pro-inflammatory (IL-8, IL-12, IL-15, MDC) and pro-angiogenic signaling (VEGF,

BMP-9, IL-8, FGF-1, ET-1, Angpt-2, HB-EGF, HGF).[253] Thus, indicate the

normalization of pulsatility even at a lower frequency can substantially minimize

endothelial dysfunction and concomitant adverse events.

3.8.4   Pulsatile modulation in CFLVAD normalized EC, but not SMC size

Indeed, in our study low cyclical frequency flow modulation approach that

generated 35 mmHg of pulse pressure enhanced the cell size of SMC compared to

diminished pulsatility. However, SMC cell size was still significantly lower compared to

normal pulse pressure and frequency condition. However, it should be noted that SMCs

showed a significant improvement with low cyclical frequency over diminished

pulsatility. Previously, Scott et al [254] demonstrated that EC-SMC coculture in high

pulsatility flow (high pulse magnitude) increased SMC size and expression of contractile

proteins, smooth muscle actin (SMA) and smooth muscle myosin heavy chains (SM-

MHC) while in the absence of ECs, high levels of pulsatility demonstrated no significant

change in cell size, and a reduced regulation of SMA and SM-MHC. Compared to our

experiments, their model did not incorporate any cyclic strain. In the light of the present

results, this may suggest that SMCs are more responsive to cyclic stretching than flow

shear forces and that in the absence of stretch, the changes in SMC shape and size may mostly be communicated through EC signaling. Previous studies [231] have demonstrated a significant increase in vascular impedance due to diminished pulsatility with CFLVAD. Given the observed change in SMC morphology with diminished pulsatility, our results indicate that while SMC morphology improves with asynchronous pulse modulation of CFLVAD, some level of derangement of vascular tone in patients may likely exist even with asynchronous pulse modulation support.

Although it is premature to base interpretations solely on cell morphology, these results suggest that there may exist a combination of pulse flow and pulse frequencies which can maintains both ECs and SMCs function and morphology. Future work will use the EC-SMC co-culture platform to do a more in-depth investigation of more relevant biomarkers such as SMC contractile protein expression, oxidative stress, angiogenesis, and inflammation markers to guide further optimization of pulse flow modulation.

3.9 Limitations

HAECs and HASMCs were obtained from healthy cell lines and are not representative of the altered phenotype present in heart failure patients. This was mitigated by keeping the cell culture in altered physiologic condition for at least 24 hours. The co-culture model does not incorporate the paracrine signaling that is present *in-vivo* but enables study of multiple mechanical loading conditions in a tightly controlled environment. Only one flow modulation strategy was tested, but the cell culture model is capable of simulating any flow modulation protocol that is physiologically feasible. The CFD simulation done to estimate the shear stress inside the flow chamber used 14 discrete time points during which the flow, pressure, and membrane shape were used to

estimate the shear stress at the wall. This method would not incorporate potential time-dependent effects of the pressure and flow on the culture membrane. However, the CFD values were in good agreement with theoretical values. The CFD studies indicated abnormal shear values in the entrance region, which may affect the EC and SMCs in that region. Cells from the entrance region were not used for analysis in this study to mitigate this concern.

3.10 Conclusion

In this study, we developed an endothelial-smooth muscle direct coculture model for human vasculature developed. The coculture was used to test the relative effects of diminished pulsatility and frequency modulation on cellular organization and size. As the need for robust *in-vitro* testing platforms grows, this novel coculture model holds the potential to be used for different types of drugs and device development and testing. The device supports physiological flow and strain and prolonged EC and SMC coculture with physiological cellular phenotypes, organization, and interactions. By using the developed system, we demonstrated that while low frequency pulse flow modulation can potentially normalize ECs morphology, it may not be adequate to prevent SMC atrophy.

CHAPTER 4: DEVELOPMENT OF A CARDIAC TISSUE CULTURE MODEL TO EMULATE THE PHYSIOLOGICAL CARDIAC ENVIRONMENT [3]

4.1 Introduction

There has been an ongoing interest in the development of efficient and effective drugs and therapies for the diseased heart. However, the complexity of the human heart makes accurate prediction of drug effects difficult. Moreover, successful translational research requires preclinical models at an adequate level of complexity to assess the impact of treatments on bio-targets as well as any collateral effects they may have. Small and large animal models are most commonly used for cardiac research. However, the anatomical and physiological interspecies differences are not trivial, including differences in thrombogenicity, heart rate, electrophysiology, and heart tissue composition. [57, 58]

Alternatively, *in-vitro* cellular models of the myocardium are readily available, and their relative simplicity facilitates clear interpretation of data. [89, 255] Indeed, such models have been instrumental in drug development as well as developing our understanding of the cellular myocardial environment. Nevertheless, current *in-vitro* myocardial models suffer serious limitations. Isolation of primary cardiomyocyte

---

Parts of the work in this chapter has been published in [1]   M. H. Meki, J. M. Miller, and T. M. A. Mohamed, "Heart Slices to Model Cardiac Physiology," (in English), *Frontiers in Pharmacology,* Mini Review vol. 12, no. 23, 2021-February-04 2021, doi: 10.3389/fphar.2021.617922.

produces low cell yield and will rapidly dedifferentiate in culture within the first 48 hours in culture, limiting their chronic use. [77] In the absence of proper biomimetic conditioning, human induced Pluripotent Stem Cell derived Cardiomyocytes (hiPSC-CMs) remain fetal and lack many of the adult cardiac phenotype characteristics such as absent cell-cell coupling, T-tubules, and under-developed sarcoplasmic reticulum. [89, 256]

Thin heart slices have been prepared from human and animal hearts with high viability and organotypic, multi cell-type structure. [112, 257] Fresh heart slices have been shown to maintain normal contractile function [120, 257, 258], electrophysiology [110, 259], calcium homeostasis [120], and response to inotropes. [120, 260] These bio-fidelic characteristics of heart slices make them an attractive system for disease and drug research. Historically, however, the usefulness of heart slices has been limited to acute experiments because of the rapid loss in structural and functional integrity beyond 24 h in culture. [257] Ou et al. have previously shown that electrical stimulation and abundance of metabolic substrate can improve the viability and functionality of heart slices in culture for 6 days.[120] However, by day 10 of culture, the heart slices experienced significant downregulation of contractile cardiac genes and upregulation of fibrotic remodeling and inflammatory genes.

By inspection, the lack of mechanical loading and humoral stimulus in culture may partially explain these observed effects. Multiple studies have shown the plasticity of heart slices to culture conditions, including changes in preload and afterload at the functional and transcriptional levels. [258, 261, 262] Thyroid hormones are known to play a vital role in cardiac development [263], and Triiodothyronine (T3) has been shown

96

previously to improve hiPSC-CMs in culture by increasing contractile force, mitochondrial activity, and improving calcium handling. [90, 264] Dexamethasone (Dex) is a potent glucocorticoid that is essential for fetal myofibril assembly and organization. [265] The combination of T3 and Dex has been shown to improve hiPSC-CMs maturity in culture and could potentially have the same effects in heart slice culture.

4.2   Study Hypothesis

In order to extend the functional and structural integrity, we hypothesize that the introduction of mechanical loading similar to physiology, coupled with appropriate humoral stimulation, can improve the adaptation of heart slices to culture and promote a more physiological cardiac phenotype. To that end, mere stretching of the tissue (e.g.,[258]) or uniaxial linear auxotonic loading (e.g., [261]) cannot recreate the normal physiological mechanical environment necessary for prolonged culture and has shown evidence of inducing hypertrophic remodeling and downregulation of cardiac genes.

 Here, an optimized myocardial slice culture system that incorporates synchronized electromechanical stimulation in a physiologically mimetic fashion is introduced. We show that the combination of T3-Dex treatment under physiological mechanical loading can improve viability, myocardial gene expression, structural integrity, and decrease fibrotic remodeling.

4.3   Application of synchronized electromechanical stimulation to heart slices

Multiple groups have shown the plasticity of cardiomyocytes to culture conditions and that mechanical loading can induce physiological/ pathological adaptation of heart slices to culture conditions. Therefore, a bioreactor Cardiac Tissue Culture Model

(CTCM) that applies synchronized, physiological electromechanical stimulation was developed. Circular pig heart slices were attached to 7mm rings using surgical histoacryl glue and placed in the CTCM which can accommodate up to 6 slices to be cultured together. The goal of CTCM is to mimic the physiological electrical stimulation and mechanical loading of the native heart, *Figure 4-1*.

4.4 CTCM operation, design, and characterization

To achieve physiological mechanical loading, CTCM uses a programmable pneumatic driver to pump air into an air chamber which is topped by a flexible silicone membrane that separates the air chamber from the culture chamber, as shown in *Figure 4-1*-**A, B**. When the membrane distends under pressure, the culture media below the tissue is displaced and stretches the heart slice, thereby preloading it. As the air chamber pressure decreases, electrical stimulation takes place and the heart tissue contracts and is allowed to shorten at a physiological rate. The pneumatic driver was set to 1.2 Hz (72 beats/min) and the systolic time was set to 40% of the cycle, while the diastolic time was set to 60%, similar to the native heart. The schematic of the culture system is shown in *Figure* **4-2.** The pneumatic driver was able to accommodate up to 4 devices working at the same timing and pressure conditions.
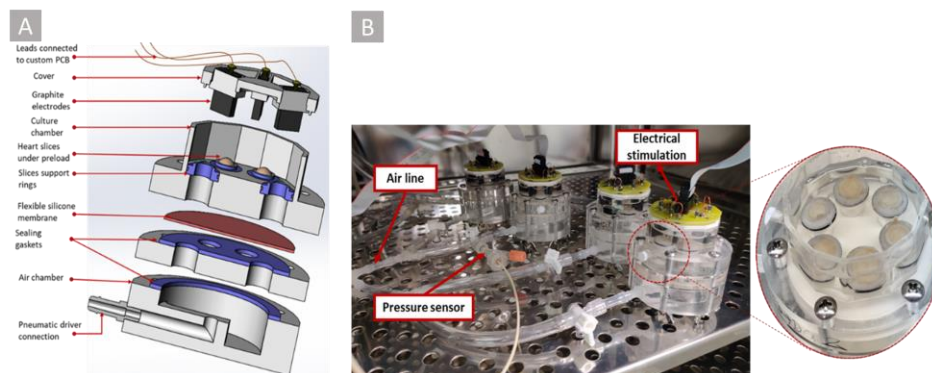
Figure 4-1 **A**- CTCM exploded view showing different components. The device is composed of an air chamber and a culture chamber that are separated by a flexible silicone membrane. The heart slices are glued onto circular rings and placed in the culture chamber. The bottom membrane will distend under pressure, thereby stretching the tissue. Graphite electrode pairs provide synchronized electrical field stimulation at 3 V/cm. **B**- The system setup is shown inside the incubator chamber. The developed system allows for 4 devices to be simultaneously connected to a single pneumatic driver, with each device containing up to 6 heart slices.
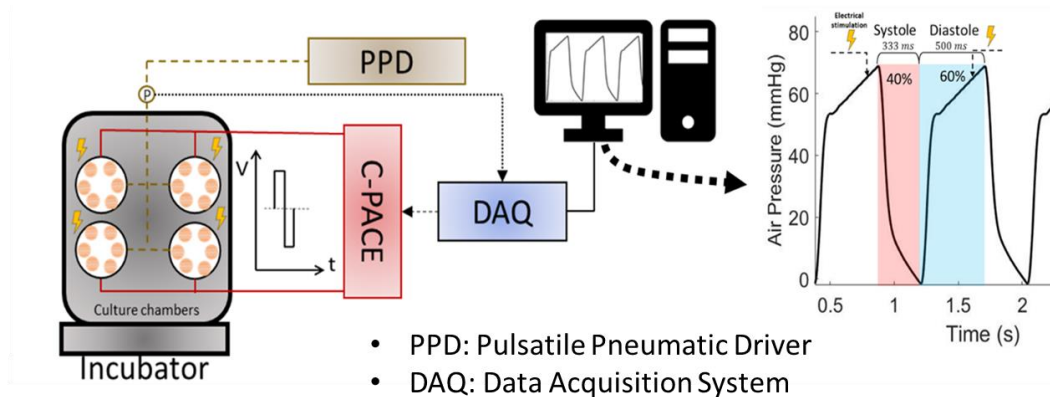
Figure 4-2 Schematic representation of the Cardiac Tissue Culture System (CTCM). The pulsatile pneumatic driver pressure line is equipped with a catheter pressure sensor and is fed into a DAQ which controls the timing of the electrical impulse stimulus.

4.5 Quantification of the heart slice movement using camera tracking

Extensive characterization of CTCM was performed. Firstly, to characterize the movement of the heart slices within CTCM and confirm that it follows the same waveform as applied pressure, a custom camera system was built as shown in *Figure 4-3*-A. Videos were recorded using a DSLR camera (Cannon Rebel T7i, Cannon, Tokyo, Japan) and Navitar Zoom 7000 18-108mm macro lens, (Navitar, San Francisco, CA).

Firstly, an open-source software (MUSCLEMOTION, [266]) was used with Image-J to quantify the movement of the heart slices. As shown in *Figure 4-3 -B*, the heart slices followed the expected strain waveform, similar to the input pressure waveform. Here, the pneumatic driver was set to 72 bpm, or 833.33 ms cycle time. Videos were recorded every day for 8 cultured heart slices in CTCM for 12 days. Each video trace was converted to a frame sequence and analyzed using MUSCLEMOTION. The collected heart slice motion traces were used to quantify the cycle time, relaxation time, contraction time, contraction rate, and relaxation rate. As shown in *Figure 4-3* **E**, the cycle time was maintained at 833±32 ms, relaxation time was 509 ± 19 ms, and contraction time was 333±22 ms. Contraction and relaxation rates were also plotted and showed a physiological waveform.

To obtain quantitative movement data, frame-by-frame tracking of the peak movement of the tissue was performed manually using image-J to characterize the heart slice stretch. To ensure a physiological level of preload stretch, the pneumatic driver was programmed to a peak pressure of 80mmHg to achieve 25% preload stretch, which corresponds to a physiological 2.2–2.3 μm sarcomere length [262, 267, 268]. As they contract during systole, the heart slices are shortened in an auxotonic fashion and follow a physiological shortening waveform [269] as shown in *Figure 4-3-***B** and *Figure 4-4*. The contraction and relaxation velocities were calculated and are plotted in *Figure 4-4*
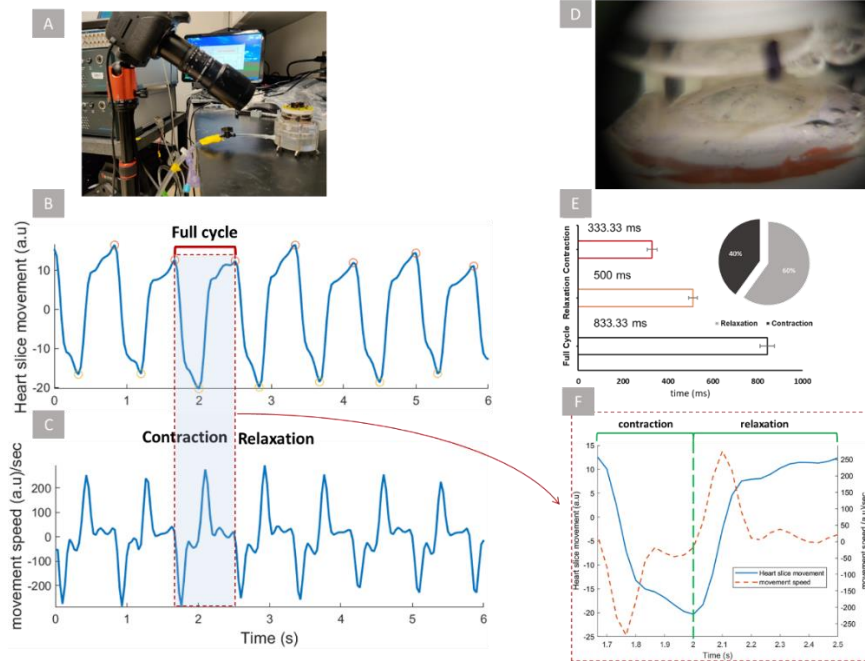
Figure 4-3 **A**- Camera system used to measure the stretch within each cycle of the heart slices. **B-** Assessment of heart slice movement by measuring the dynamic changes in pixel intensity in MUSCLEMOTION in Image-J. Representative tissue movement is shown with peak and valley detection that were used to calculate cycle timing and peak to peak movement. The movement speed was also calculated from the slice movement **C-** Movement speed was calculated from acquired video data showing peak contraction velocity. **D-** Representative video frame collected from **E-** Calculated heart slice timing using MUSCLEMOTION results showing that 40% of the cycle time was systole and 60% was diastole. The relaxation (diastole), contraction (systole), and cycle times were calculated for traces of 8 different tissues over 12 days in culture (N=96)**. F**- Close up representative loading cycle in CTCM showing the heart slice movement and movement velocity.
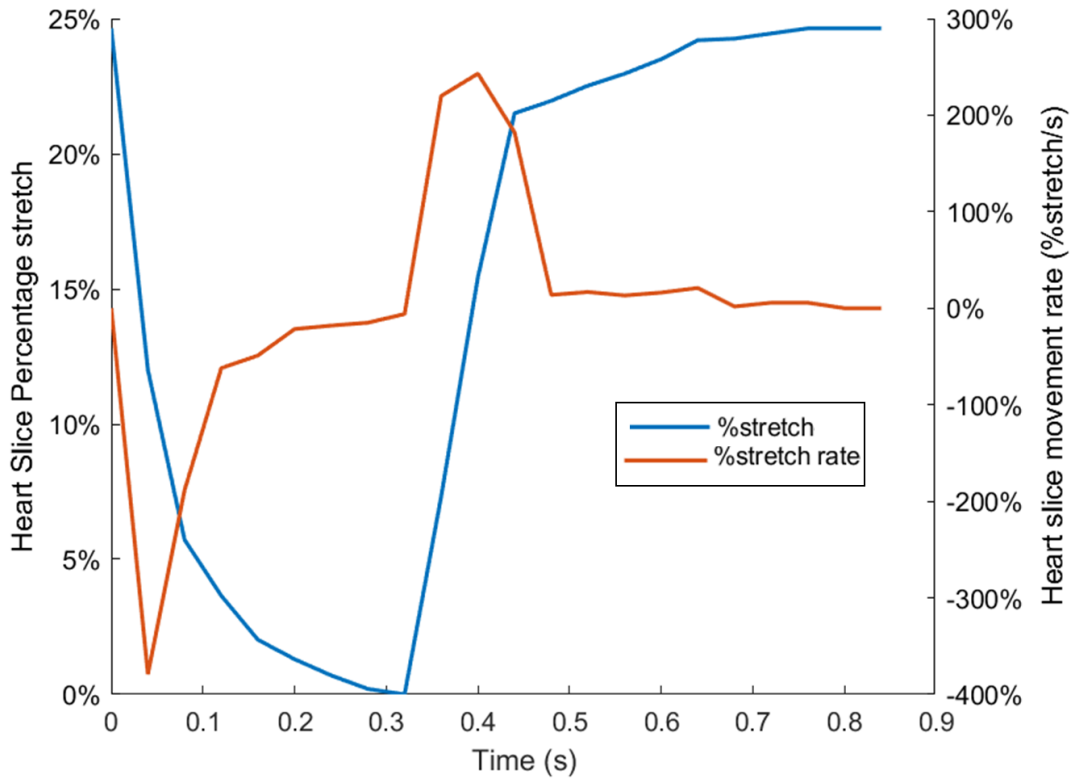
Figure 4-4 Frame by frame analysis of the heart slice stretch over a representative cycle. The figure shows the calculated percentage stretch for the heart slices. The stretch rate is shown in orange showing the peak contraction rate and relaxation rate. The tissue is stretched by 25% during diastole and is electrically stimulated and allowed to contract at a physiological rate during systole.

4.6   Characterization of the electrical stimulation in CTCM

A custom printed circuit board was designed to interface with an electrical stimulator (C-PACE EM, IonOptix, Westwood MA). Graphite electrode pairs provided field stimulation of the heart slice tissue. 2ms Biphasic electrical voltage signal was set to achieve 3.1 V/cm electric filed intensity at the center of the tissue and was confirmed

with computational simulation using Finite Element Analysis (FEA), as shown in **Figure 4-5**.
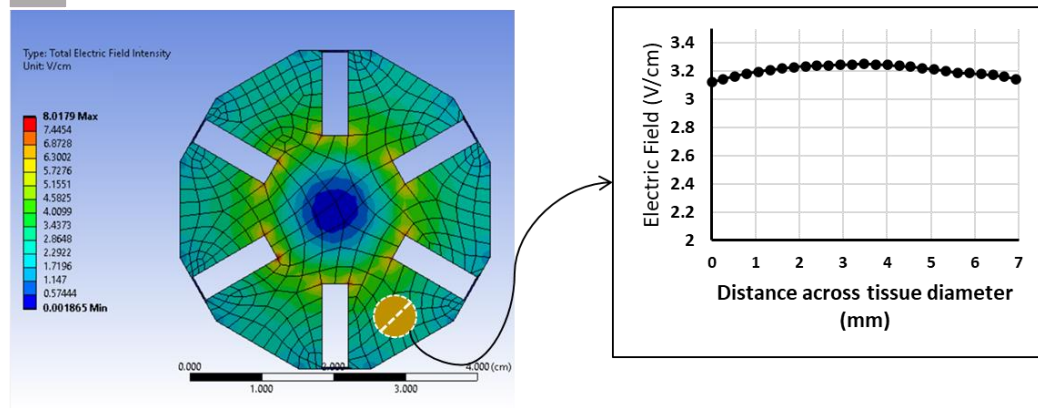
Figure 4-5 Computational simulation of the electrical field inside the culture chamber, showing the position of the heart slices within the chamber. The electric field across the tissue diameter was uniform and did not exceed 3.2 V/cm.

4.7   Estimation of the strain field within the heart slice

As the heart slices are stretched, cardiomyocytes are subjected to circumferential and radial strain. In the healthy heart the preload strain varies between 15%-27%. [270] The peak tissue center movement was recorded and was used as reference for the estimating the strain within the tissue. The simulated strain field within the heart slices at end of diastole was determined using FEA analysis (ANSYS Mechanical, Canonsburg, PA). *Figure 4-6* shows the central movement out-of-plane of the heart slice tissue and the resulting radial and circumferential strain along the tissue diameter.
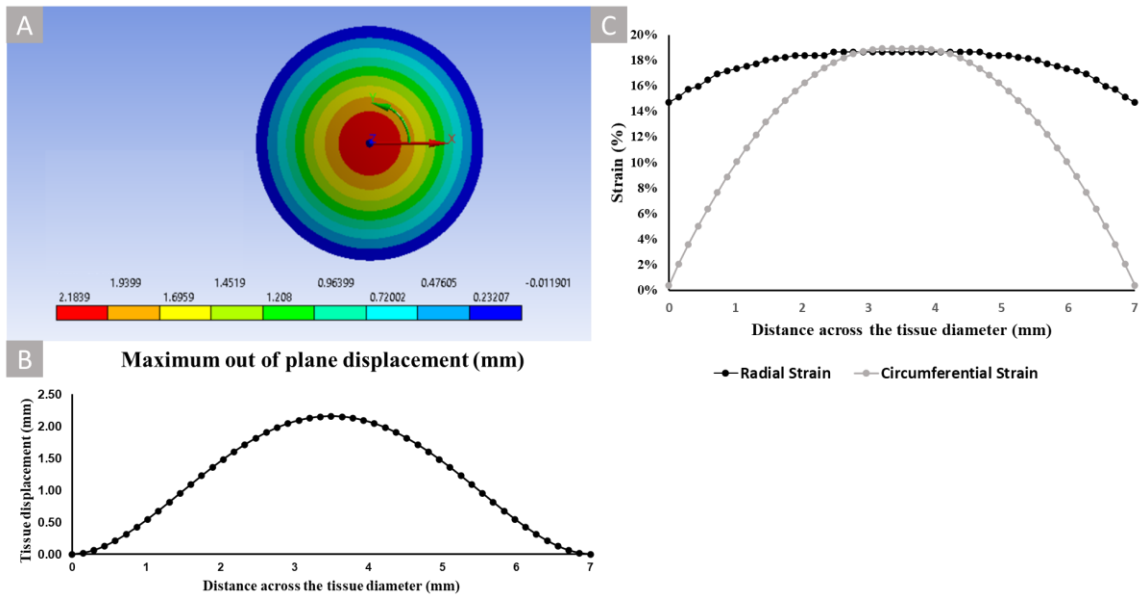
Figure 4-6 Estimation of strain field within the tissue slice using FEA in ANSYS Mechanical. A,B- Heart slice deflection under pressure, and C- simulated radial and circumferential strain in the tissue slice as a function of radial distance across the tissue.

4.8   Experimental Design

To investigate the effects of mechanical loading and T3-Dex treatment on heart slices, pig heart slices were cultured in CTCM with T3-DexD treatment (MT condition) and without T3-Dex treatment (MC condition). Additionally, heart slices cultured in CTCM were compared to static culture controls without T3-Dex treatment (CTRL condition) and with T3-Dex treatment (TD condition). CTRL and TD were cultured in transwell plates with nutrient rich medium, oxygenations, and electrical stimulation as previously described in [62, 271]. All four conditions (CTRL, TD, MC, MT) were cultured over 12 days and tissue was collected for end point assays and compared to fresh tissue slices from day 0. A schematic representation of the experimental design is shown in *Figure 4-7*.
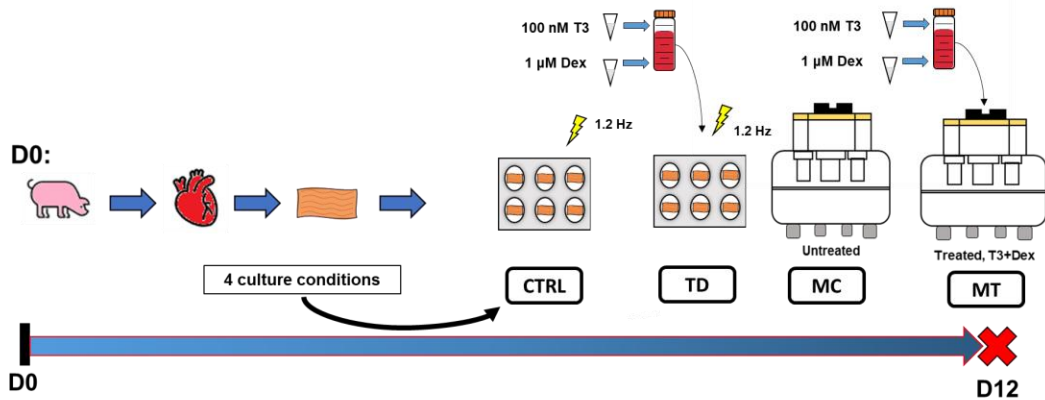
Figure 4-7 Schematic representation of the experimental design to evaluate the performance of CTCM and T3-Dex small molecule treatment. 4 conditions were cultured using fresh pig heart slices for 12 days: (1) MT, CTCM electromechanically stimulated tissue with T3-Dex treatment, (2) MC, CTCM electromechanically stimulated tissue without treatment, (3) TD, unloaded, static tissue treated with T3-Dex treatment, and (4) CTRL, unloaded, static tissue without treatment.

4.9 Assessment of viability, energy utilization, and structural integrity in pig heart slices.

To determine the effect of humoral and electromechanical stimulation on heart slices in 12 days prolonged culture, 6 mm circular sections were punched from each condition and metabolic activity was assessed using MTT assay as a marker for cell viability. As shown in *Figure 4-8* (A), following 12 days in culture viability did not significantly decrease in CTCM (MC and MT) conditions and was maintained similar to fresh tissue ($p > 0.05$). Interestingly, the addition of T3+Dex to transwell culture (TD) did not significantly improve viability compared to CTRL condition, implying the vital role of mechanical stimulation in maintenance of heart slice viability.

Further, to determine if the improvement in viability may be due to alterations in energy utilization and metabolism, glycolytic flux assay was performed on all four conditions. Metabolic shift from fatty acid oxidation to glycolysis is a hall mark for cardiomyocyte dedifferentiation. Immature cardiomyocyte primarily utilize glucose for ATP production and have underdeveloped mitochondria with few cristae. and shift towards a fetal phenotype. [1, 272] As shown in *Figure 4-8*-**B**, glycolytic flux assay revealed a significant increase in glucose utilization for energy generation in CTRL condition compared to day 0 after 12 days in culture. However, MC and MT conditions showed glycolysis utilization similar to day 0. TD condition caused a higher level of glycolysis than MC and MT but did not reach statistical significance compared to fresh tissue (p>0.05).

Next, we investigated if the improvements with humoral and mechanical loading were reflected on the structural protein level. Mechanical stretch is known to be an essential stimulus for cardiomyocyte arrangement and contraction. [273, 274] Non-physiological mechanical loading, or lack thereof, will trigger structural changes of the sarcomere, contractile machinery, and cellular communication. [275, 276]. To assess structural integrity of cultured heart slices, immunostaining of cardiac troponin T (cTnT) and gap junction protein connexin 43 (Cx43) was performed, *Figure 4-8*- **C**. Propagation of the electrical stimulus in the heart is regulated by the gap junctions which can synchronize action potential progression and contraction. Cx43 is the major connexin protein expressed in the ventricular myocardium and its normal expression at the gap junction is essential for coordinated cardiomyocyte electrical activity.[277] At day 12 of culture, Cx43 was intact and widely localized at the gap junctions in MT condition, with

normal cell morphology and myofibrillar striation. To characterize the structural integrity of the imaged heart slices, we developed a deep learning Convolutional Neural Network (CNN) framework to assess the overall deterioration in tissue structure, organization, signal intensity, and localization. This AI framework was previously validated and published in [278]. The automated structural deterioration assessment algorithm outputs the probability that a given immunofluorescence image is similar to day 0 tissue. Merged heart slice images fluorescently labeled for DAPI, cTnnT, and Cx43 from each of the 4 conditions were analyzed for their structural similarity to Fresh heart tissue. As shown in *Figure 4-8* (D), T3-Dex treatment significantly improved heart slice structure compared to CTRL tissue ($p<0.001$) and was ~48% similar to fresh tissue. Culture in CTCM appeared to further improve the structural benefits of T3-Dex treatment, where MT conditions showed the most structural improvement compared to CTRL tissue and resulted in an overall tissue structure that is ~77% similar to fresh tissue. Interestingly, while there was a trend towards improvement in MC tissue compared to control, it did not reach statistical significance ($p=0.059$) and did not exceed ~30% similarity. These results provided additional evidence on the synergistic favorable effects of T3-Dex small molecules and physiological mechanical loading.
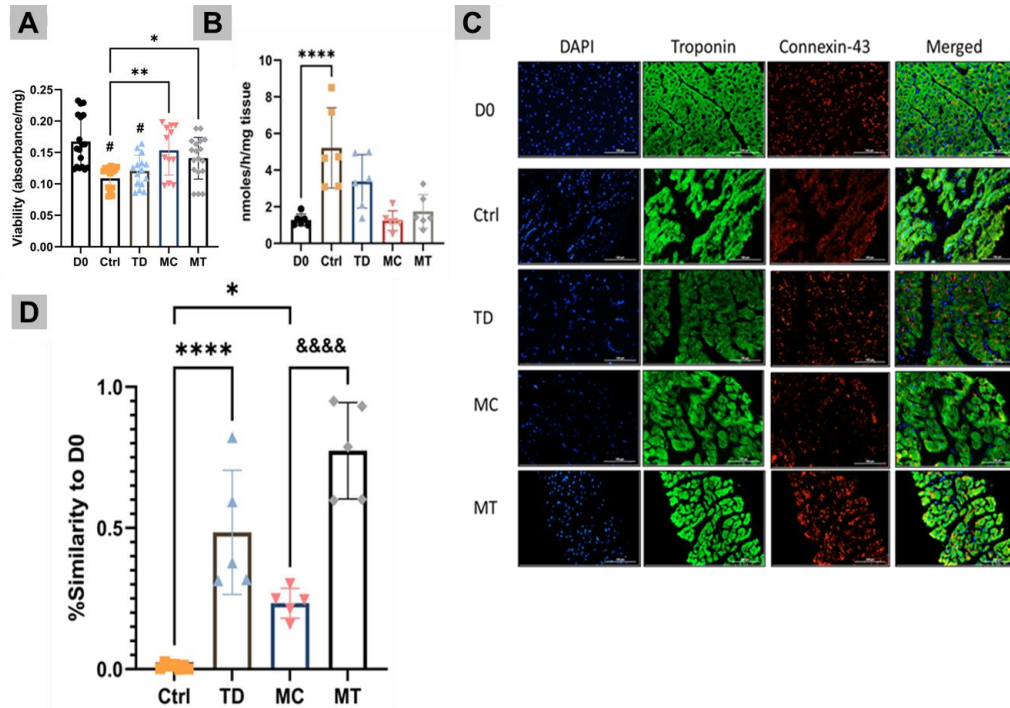
Figure 4-8 **A**- Tissue viability assessed using MTT assay on day 12 of culture compared to day 0 tissue. Fresh tissue (D0), N=6, CTRL, N=6, TD, N=3, MC, N=3, MT, N=3. **B**- Glycolytic flux assay after 12 days in culture. D0, N=6, CTRL, N=6, TD, N=6, MC N=6, MT, N=5. **C**- Representative immunofluorescence staining image of connexin-43 and troponin-T on tissue from day 12 in culture. **D**- Percentage structural similarity of heart slices after 12 days in culture to fresh heart slices (D0). CTRL, N=6, TD, N=5, MC, N=5, MT, N=5. One-way analysis of variance (ANOVA) was used to determine if there were any significant differences between groups. Dots represent individual data points. *,**** groups compared to CTRL * $p<0.05$, **** $p<0.001$, # groups compared to D0 $p<0.05$, @@@@ groups compared to TD, @@@@ $p<0.001$, &&&& groups compared to MC, &&&& $p<0.001$.

4.10 Assessment of Fibrosis in heart slices under electromechanical stimulation and T3-Dex treatment

Immunohistochemical staining for cTnT and Cx43 revealed an improvement in tissue structure and was based on myofibrillar structure and gap junction protein localization. Cardiac fibroblasts are the predominant Extra Cellular Matrix (ECM) producing cells in the heart and are of paramount importance in preserving fibrillar collagen homeostasis. [279] Cardiomyocytes have a negligible ability to regenerate and during cellular damage or inadequate conditions, as seen in several cardiomyopathies, excessive fibrosis will take place through either activation of fibroblast synthetic pathways or a disproportionate matrix degradation. To further evaluate the effectiveness of T3-Dex treatment and CTCM in modulating healthy structural adaptation in heart slices, Masson's Trichrome staining was performed on fixed heart slices to quantify fibrosis interstitially. The location within the ventricle from which the slices are harvested varies from one slice to another and the presence of capillaries and blood vessels was common within the collected slices. To account for that, only interstitial fibrosis was considered in the quantification and perivascular fibrosis was excluded, as shown in *Figure 4-9*-**A**. Trichrome quantification revealed a significant reduction in interstitial collagen in TD condition compared to CTRL, indicating the efficacy of T3-Dex treatment in reducing fibrosis in pig heart slices, *Figure 4-9*-**B**. This is in congruous with the anti-fibrotic effects of T3, likely due to inhibition of TGF-β1 dependent pathways [280]. Interestingly, in the absence of T3-Dex treatment in CTCM culture (MC condition) fibrosis was significantly reduced compared to CTRL condition. Importantly, MT showed further reduction in area of fibrosis compared to MC. While MT condition

did not completely stop the fibrotic remodeling, the combined effects of electromechanical stimulation and T3-Dex small molecule treatment showed the best reduction in the maladaptive fibrotic processes within the tissue.
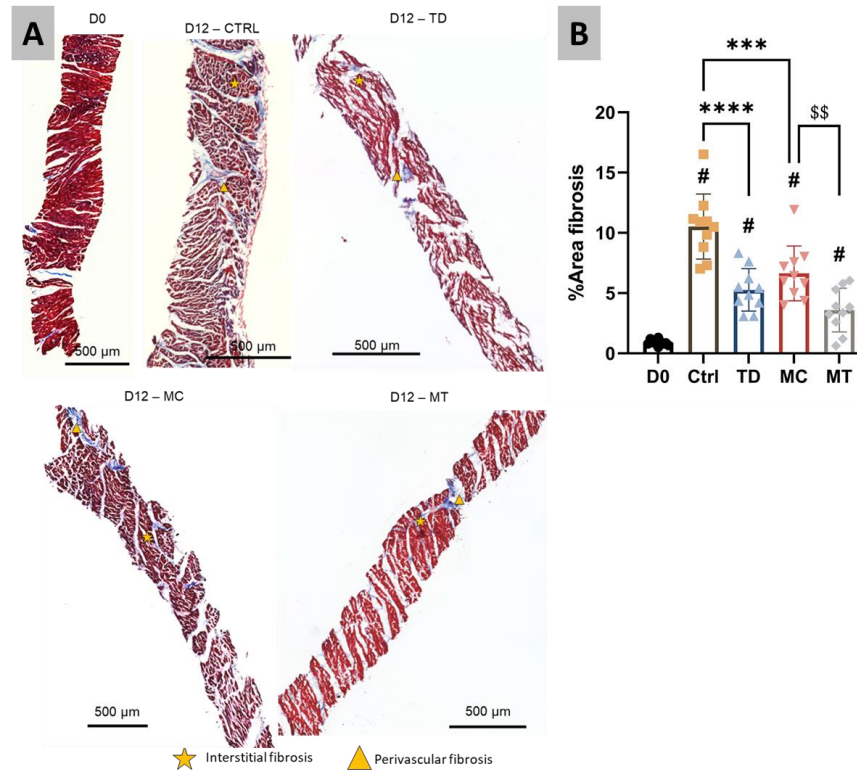
Figure 4-9 **A**- Representative images obtained from Masson's trichrome staining for all 4 conditions showing areas of interstitial fibrosis and perivascular fibrosis, **B**- Percentage area fibrosis quantification as measured from Masson's trichrome stained slices. N=10 per group. # groups compared to D0, # $p<0.01$. ***,**** groups compared to CTRL, *** $p<0.01$, **** $p<0.0001$. $$, compared to MC, $$ $p<0.01$.

4.11 Transcriptional profiling of pig heart slices under electromechanical stimulation and T3-Dex treatment

RNA sequencing was performed to evaluate the effects of electromechanical stimulation and small molecules on the transcriptome, *Figure 4-10*. Heart slice tissue

from all 4 conditions was collected at days 8, 10, and 12 and were subsequently compared to fresh heart tissue from day 0. The goal of the transcriptional profiling was to investigate the effects of physiological mechanical and humoral stimulation on heart slices expression of cardiac and contractile genes. Compared to D0, unloaded conditions (CTRL and TD) showed a significant downregulation of genes coding contractile protein synthesis. Transcriptionally, the addition of T3-Dex treatment did not significantly improve cardiac gene expression compared to CTRL. The introduction of electromechanical stimulation in MC condition relatively improved expression of cardiac and contractile genes compared to CTRL and TD but were still downregulated in comparison to fresh tissue, as shown in Figure. 5. Interestingly, the combination of electromechanical stimulation and T3-Dex treatment in MT condition resulted in an expression profile most similar to fresh heart slices with only 30 differentially regulated genes after 12 days in culture (23 genes downregulated and 7 genes upregulated). Contractile filament protein coding genes (e.g., TNNT2, TNNC1, MYH7, and MYL3) were all normally expressed compared to fresh tissue.
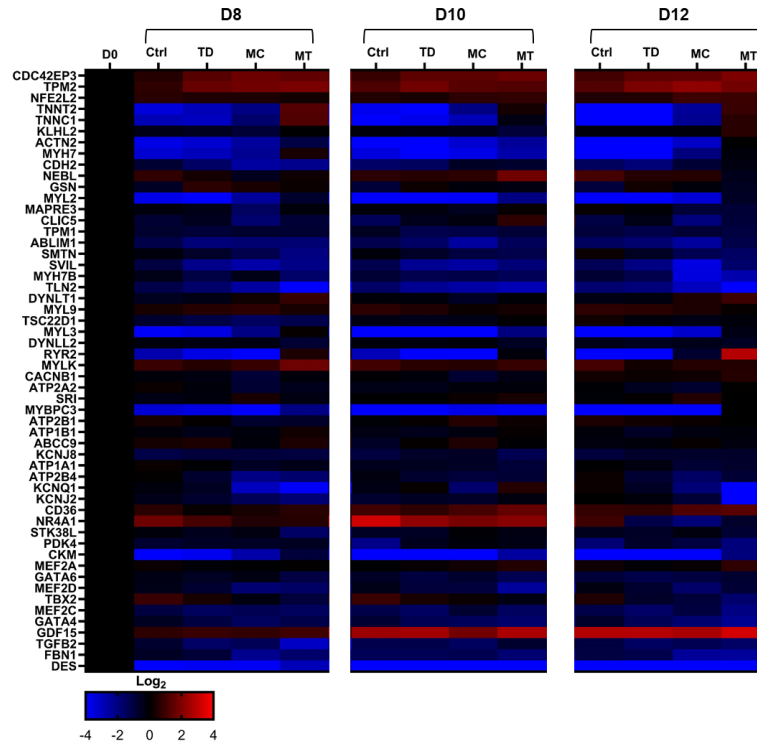
Figure 4-10 Heat map showing log2-fold change in gene expression of representative cardiac genes on days 8, 10, and 12 in culture compared with fresh heart slices (D0).

4.12 Modelling volume overload by the use of CTCM

Heart tissue is continuously exposed to external forces *in-vivo* and pathological forces can induce diseased cardiac remodeling. The ability to model altered mechanical environments is of particular importance for therapeutic and drug discovery. To illustrate the ability of CTCM in modeling diseased mechanical states, the CTCM was used to model volume overload condition was modeled. During volume overload, end-diastolic volume is increased due to numerous abnormalities such as aortic and mitral valve insufficiency. [281] The elevated ventricular preload causes increased stretching of the cardiomyocyte beyond physiological levels and has been related to an array of compensatory effects the most significant of which is eccentric hypertrophy. In eccentric

hypertrophy, ventricular wall thickens due to increased fibrosis and myocardial fibrosis while the ventricular lumen is dilated. In CTCM, the peak pressure in the air chamber was increased from 80 mmHg (Normal stretch) to 140 mmHg, as shown in *Figure 4-11*. This corresponds to a preload stretch of 32%. Heart slice tissue treated with T3-Dex (MT) and without T3-Dex (MC) were either subjected to normal preload stretch (MC-Norm, MT-Norm) or volume overload conditions (MC-OL,MC-OL) for 6 days. The heart slices were assessed for viability, cardiomyocyte cell size, and fibrotic remodeling.
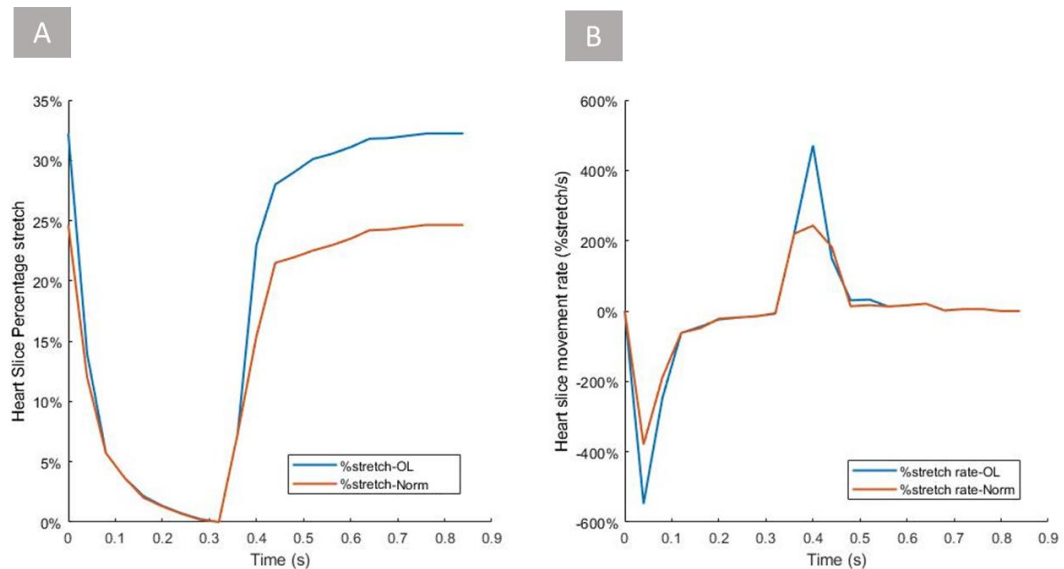
Figure 4-11 **A-** Percentage stretch during volume overload modeling assessed using a custom camera system. The heart slices are stretched by 32% during diastole, compared to 25% during normal physiological loading. **B-** Stretch rate during volume-overload compared to normal physiological load. The peak contraction velocity is increased in volume-overload compared to normal loading as well as the peak relaxation velocity.

4.13 Hypertrophic and fibrotic remodeling with increased preload stretch.

Pathological cardiac remodeling takes place in response to altered mechanical states. The compensatory mechanisms which help adapt the heart to transient demanding conditions (e.g., fight or flight and physical exercise). In contrast, pathological loading as in valvular diseases, hypertension, or infarcted hearts will cause maladaptive remodeling.

Hypertrophic remodeling was assessed by staining the cell membrane using Wheat Germ Agglutinin (WGA). Quantification of cardiomyocyte cross-sectional area revealed a significant increase in cell size in both MC-OL and MT-OL compared to their respective control (MC-Norm and MT-Norm), *Figure 4-12*. Further, to determine the formation of fibrosis within the cardiac lattice, Masson's trichrome was used. As shown in *Figure 4-13*, fibrosis was significantly increased in MC-OL and MT-OL compared to D0 and to their respective controls. These results show clear evidence of pathological remodeling, typical of volume overload conditions.
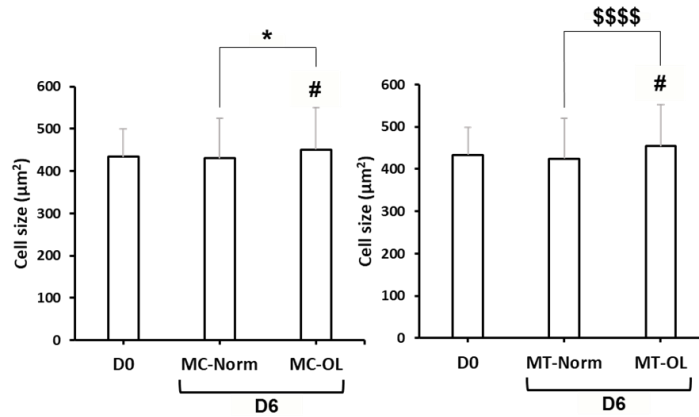
Figure 4-12 WGA quantification of cardiomyocyte cell size in volume-overload

conditions MC-OL and MT-OL compared to normal physiological load and fresh heart

slices (D0). # Significant groups compared to D0, # $p<0.01$. * Significant groups

compared to MC-Norm, * $p<0.05$. $$$$, significant groups compared to MT-Norm, $$$$

$p<0.0001$. MT-OL showed a 7% increase in cell size compared to MT-Norm, while MC-

OL showed a 5% increase in cell size compared to MC-Norm. D0, N= 267. MC-Norm,

N= 346. MC-OL, N=294. MT-Norm, N =369. MT-OL, N=330.
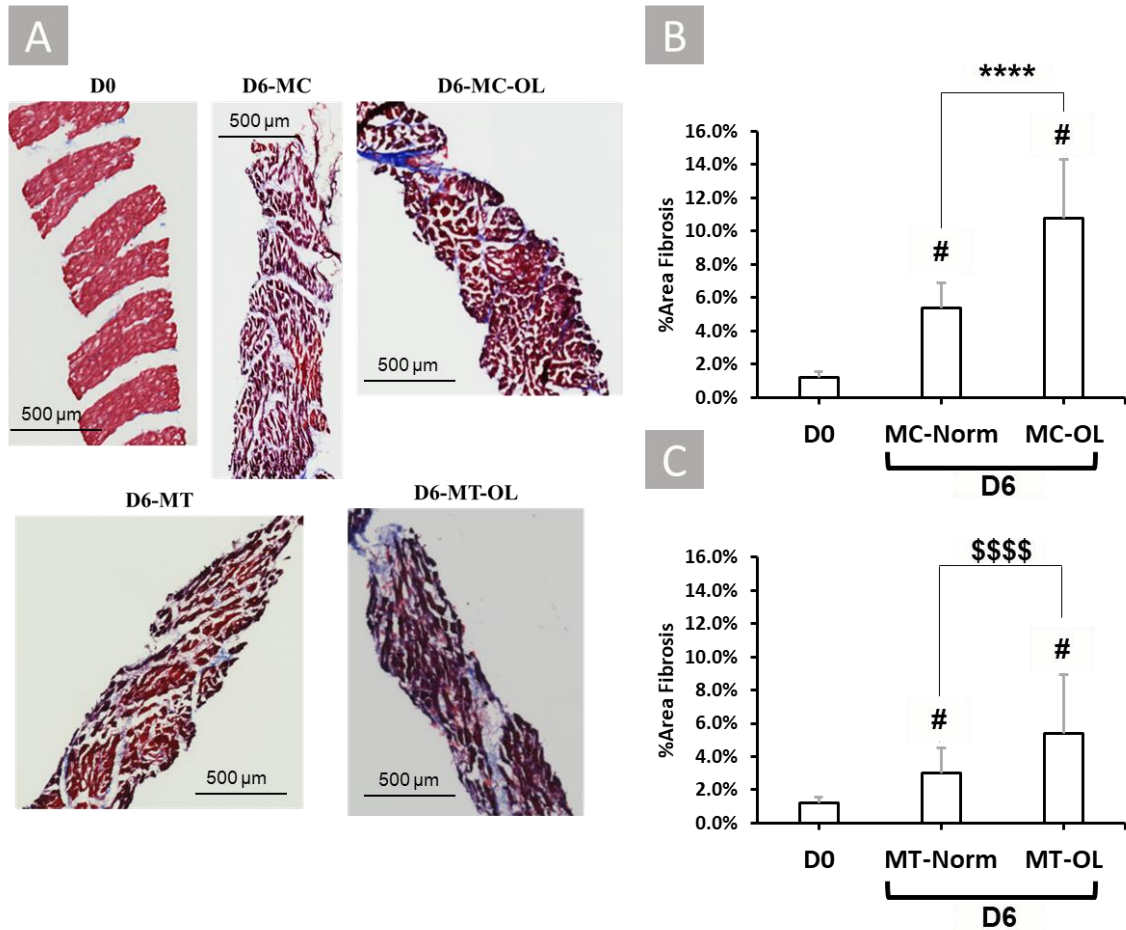
Figure 4-13 Fibrosis assessment using Masson's trichrome staining after 6 days in culture with volume-overload. A– representative images for trichrome staining from each condition. B,C– %area fibrosis quantification asses for all conditions.   #, significant from D0, # p <0.01. **** significant from MC-Norm, **** p<0.0001. $$$$ significant from MT-Norm, $$$$ p<0.0001. D0 , N= 18, MC-Norm, N =16, MT-Norm, N=16, MC-OL = 15, MT-OL, N=16. One-way ANOVA was used to determine significance.

4.14 Discussion

Translational cardiovascular research requires cellular models capable of faithfully replicating the cardiac milieu. In this study, a cardiac tissue culture model (CTCM) that

uses ultra-thin heart slices was developed and characterized. CTCM system encompasses physiological synchronized electromechanical stimulation coupled with humoral enrichment with T3 and Dex. Building on previous work by Ou et al. [120], these results demonstrated improved viability, structural integrity, reduced fibrosis, normal energy utilization for 12 days in culture. These results confirm the critical role of physiological culture conditions in the maintenance of a normal cardiac phenotype.

Multiple factors contribute to the optimal environment for cardiomyocyte functional survival. The most identifiable of these factors are related to 1) cell-to-cell interactions through paracrine signaling as well as through force transduction, 2) electromechanical stimulation, 3) humoral factors, and 4) metabolic substrates. Physiological cell-to-cell interaction requires the presence of intricate 3-dimensional multi-cell-type cellular networks with extra cellular matrix. While this factor is difficult to recreate *in-vitro*, it lends itself easily in organotypic heart slices. Moreover, mechanical loading of cardiomyocytes has been indicated to be of paramount importance in preserving the cardiac phenotype. [282-284] While mechanical stimulation has been used extensively in hiPSC-CM conditioning and maturation, few studies have attempted mechanical loading of heart slices in culture. [121, 267] Indeed, these studies have shown the positive influence of mechanical loading on the cardiac phenotype. However, the way by which the heart slices were loaded did not replicate the physiological mechanical loading by using either isometric stretch forces [267] or linear auxotonic loading [121] and was reflected on the downregulation of multiple cardiac genes or the overexpression genes related to pathological stretch response. Notably, Pitoulis et al. [262] developed a dynamic heart slice culture bath to recreate the cardiac cycle using a force transducer

feedback and a stretcher actuator. The main drawback with this system is complexity and low throughput where the culture bath can only accommodate one heart slice at a time. In the present platform, CTCM can provide electromechanical stimulation that mimics the native cardiac cycle in terms of cycle timing and loading (25% preload stretch, 40% systole, 60% diastole, and 72 beats per minutes). By replicating physiological strain waveform (similar to the ventricular volume waveform), the mechanical loading of the heart tissue can be modulated, which was demonstrated by simulating a volume-overload condition.

T3 can influence transport of amino acids, sugars, and calcium across the cell membrane as well as increase transcription of MHC-A, and decrease MHC-B. [285] The lack of T3 in the normal heart, as with hypothyroid patients, can lead to loss of myofibrillar striation, interstitial fibrosis, and reduced rate of tension development.[285] On the other hand, Dex is mediated by the glucocorticoid receptor and has been shown to increase cardiac contractility in ex-vivo perfused hearts [286] and this improvement is thought to be related to an effect on store operated calcium entry (SOCE). [287, 288]

Interestingly, our results showed that physiological mechanical stimulation (MC) improved overall culture performance compared to CTRL, but could not solely maintain viability, structural integrity, and contractile protein expression after 12 days in culture. The incorporation of T3-Dex treatment into CTCM culture resulted in improved viability compared to transwell culture with electrical stimulation (CTRL), maintained 80% structural similarity to fresh tissue, and provided most reduction in fibrosis formation compared to all other experimental conditions. The effects of T3-Dex were also noticed in the context of metabolic energy utilization where static heart slices treated with T3-

Dex (TD) showed normal glucose utilization for energy production compared to D0 which was also achieved in MC condition. Moreover, TD condition also showed significant decrease in fibrosis and improvement in cx43 expression and structural integrity compared to CTRL. This is consistent with previous studies indicating their favorable effects on hiPSC-CM maturation, T-tubule development, and contraction. [289] The current study shows 1) the beneficial effects of T3-Dex for cardiac maturation, in line with past reports in previous studies using hiPSC-CMs, and 2) an interesting synergistic effect of electromechanical and T3-Dex hormonal treatment on heart slice functional integrity.

CTCM is considered a major advancement over the old transwell culture with optimized media (CTRL), which was only able to maintain viability for 6 days in culture and suffered severe downregulation of cardiac genes by day 10. [271] Here, CTCM combination of electromechanical stimulation and T3-Dex treatment in MT condition supported the hypothesis that biomimetic culture of myocardial slices can further improve their survival and maintain their phenotype in culture and that a combination of different physiological stimulants is needed to achieve that. Moreover, a single device can accommodate up to 6 heart slices cultured under identical conditions. In our experience, a single pneumatic driver can be connected up to 4 CTCM devices without causing significant attenuation of the pressure due to membrane and tubing compliance.

Pathological volume-overload modeling using CTCM was achieved by controlling the pulsatile pneumatic driver pressure, illustrating the versatility of the CTCM system. Volume-overload culture showed typical effects associated with pathological compensatory remodeling of the heart in MC and MT conditions where fibrotic processes

and hypertrophic remodeling were both significantly increased by day 6 of culture. It should be noted that CTCM parameters can be modulated to simulate many conditions such as tachycardia, bradycardia, pressure overload, and mechanical circulatory support (mechanically unloaded heart) by changing the pneumatic driver parameters. The presented technology could be used to study cardiotoxic effects and efficacy of novel therapeutic agents. Future studies will aim at including more in-depth assessments of the CTCM cultured heart slices. Meaningful data should include continuous monitoring of the contractile function of heart slices, and mechanical characteristics of heart slices over days.

4.15 Limitations

In this study, ultra-thin heart slices were prepared from pig heart slices. CTCM culture using porcine heart tissue showed preserved viability, physiological energy utilization, similar structure to fresh heart tissue, and normal expression of contractile proteins. However, the study lacked confirmation of these findings using tissue of human origins. Further, the mechanical loading of the slices within the culture in CTCM was applied by stretching the tissue in a controlled manner within physiological limits and hence loading the tissue while it actively contracts. In CTCM. While our results show normalized contractile gene expression, improved cardiac structure, z-disc alignment and gap junction cx43, CTCM does not allow for active monitoring of cardiac contraction during each cycle. The size of tissue that can be used with this device was limited to only 7mm diameter. This limitation is to make sure that tear-free circular slice can be extracted from the tissue. Lastly, the CTCM is of medium complication and includes multiple parts that need to be assembled together including pressurized air from a

pulsatile pneumatic driver which needs to be connected into an incubator and provides a possible source of contamination.

4.16 Conclusion

A novel cardiac tissue culture model was developed that allows for maintained culture of adult myocardial slices under physiological mechanical and humoral stimulation. The study showed that the addition of T3-Dex hormonal treatment significantly improved heart slice culture viability, structural integrity, and energy utilization. CTCM demonstrated the ability to model pathological conditions, which can be used to test drugs and therapies. The cardiac milieu is complex and the ability to replicate some of its constituents showed that it can improve heart slice culture *in-vitro*. This study provides a major advancement over current methodologies, including the ability to mimic the cardiac cycle while maintaining adequate throughput, providing synchronized electromechanical stimulation, and combining humoral stimulation (T3-Dex) with optimized media rich with nutrients.

4.17 Methods

4.17.1 Heart tissue collection from pigs

To collect heart tissue from pigs, all animal procedures were in accordance with institutional guidelines of the University of Louisville and approved from the Institutional Animal Care and Use Committee (IACUC). Pig hearts are clamped at the aortic arch and subsequently perfused with 1L sterile cardioplegia solution (110 mM NaCl, 1.2 mM $CaCl_2$, 16 mM KCl, 10 mM , 6 mM $MgCl_2$, $NaHCO_3$, 5 U/mL heparin, and set to a pH of

7.4). The hearts were preserved in ice-cold cardioplegia solution and transported to the lab.

4.17.2 Heart slicing

As described in detail here [271], pig hearts are packaged in sterile glass container with cardioplegia solution containers. The left ventricle is sectioned into 1-2 cm^3 blocks. Epicardial side of the block was glued onto 4% agar bed using histoacryl glue and subsequently glued on top of the specimen holder of the Vibrating Microtome 700SMZ (Campden Instruments). The cutting bed was filled with 4°C modified Tyrode's solution (Tyrode's solution (140 mM NaCl, 6 mM KCl, 10 mM glucose, 10 mM HEPES, 1mM $MgCl_2$, 1.8 mM $CaCl_2$) and 2,3-butanedione monoxide (BDM) 10mM and set to pH 7.4. To limit cardiomyocyte damage while slicing, the vibrating microtome's z-axis vibration was calibrated with the ceramic cutting blade to <0.5 µm. The vibrating microtome was set to produce 300 um thick slices with an advance speed 0.03 mm/s and 80 Hz vibration frequency and 2mm horizontal vibration amplitude. The heart slices were the immersed in Tyrode's solution without BDM in a cold bath for at least 20°C to wash out BDM before being glued to the ring supports.

4.17.3 Heart slice culture

Transwell culture:

The same protocol previously described by Ou et al. [120] was used. Here, heart slices were glued at their edges using histoacryl glue to polyurethane supports (6 mm width). The supported slices were transferred into 6 well plates containing 6 mL of stimulated medium. The composition of the medium is Medium 199, 1x ITS supplement, 10% FBS, 5 ng/mL VEGF, 10 ng/mL FGF-basic, and 2X Antibiotic-Antimycotic). The

C-Dish top (IonOptix, Westwood, MA) with 6 pairs of graphite electrodes were placed

on top of the 6 well plate and connected to the C-Pace-EM system (IonOptix, Westwood,

MA) and stimulated at 10V and 1.2 Hz. The plates were placed in the incubator at 37 C

with humidified air and 5% CO2. C-Dish top was swapped every day to avoid build up of

contaminants on the electrodes. Culture media was changed 3 times a day and either

supplemented with T3-Dex (100 nM T3, and 1 µM Dex) with every media change.

CTCM culture:

Heart slices were first placed on a custom 3D-printed apparatus to oversize the

heart slices by 25% of the support ring area. The apparatus was placed in a modified

Tyrode's solution bath to ensure complete contractile filament decoupling. The oversize

apparatus ensures the heart slices are not over-stretched when they are taken out of the

Tyrode's solution and placed in media. The ring support were prepared with histoacryl

glue and push against the tissue as shown in *Figure 4-14*. The ring supports with sealing

O-rings were placed in the CTCM device prefilled with 21 mL of stimulated media

(Medium 199, 1x ITS supplement, 10% FBS, 5 ng/mL VEGF, 10 ng/mL FGF-basic, and

2X Antibiotic-Antimycotic). The process was repeated for each ring and finally the cover

plate with graphite electrode pairs and custom interface C-PACE-EM system was placed

on top and set to provide 4 V at 1.2 Hz, 2ms biphasic stimulation. The assembled device

was then placed in temperature and humidity-controlled incubator, 37°C with humidified

air and 5% CO2. The pneumatic driver was then turned on and the air flow valve was

turned on. Media was changed twice every day, and the graphite electrodes were

swapped every day to avoid buildup of contaminants within the electrode pores. T3-Dex

treatment was added with every media change at 100 nM T3, and 1 µM Dex.
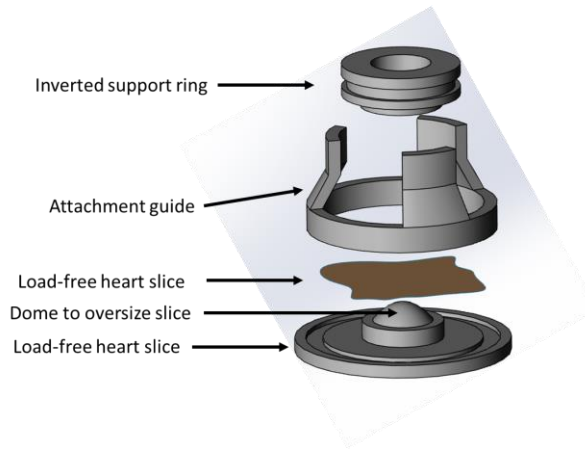
Figure 4-14 3D-printed oversizing apparatus to ensure no mechanical stretch on the unloaded heart slice once glued on the ring. The load-free heart slice in Tyrode's solution with BDM is oversized 25% by area compared to the ring area.

4.17.4 CTCM fabrication, design, and dimensions

Culture chamber, air chamber, support rings, silicone membrane, and gaskets:

CTCM was designed in SolidWorks Computer Aided Design (CAD) software. Parts were CNC machined out of clear acrylic plastic. Support rings were center-lathed from high density poly-ethylene plastic (HDPE). The support ring is equipped with an O-ring groove that accommodate a silicone O-ring for sealing the media volume below the ring. The silicone membrane was laser-cut out of 0.02'' silicone sheet, durometer 35A. The bottom and top silicone gaskets were laser-cut from 1/16'' silicone sheet, durometer 50A. 316L stainless steel screws and wing nuts were used to sandwich the body parts together to create an air-tight seal. Gross part dimensions are shown in *Figure 4-15*.
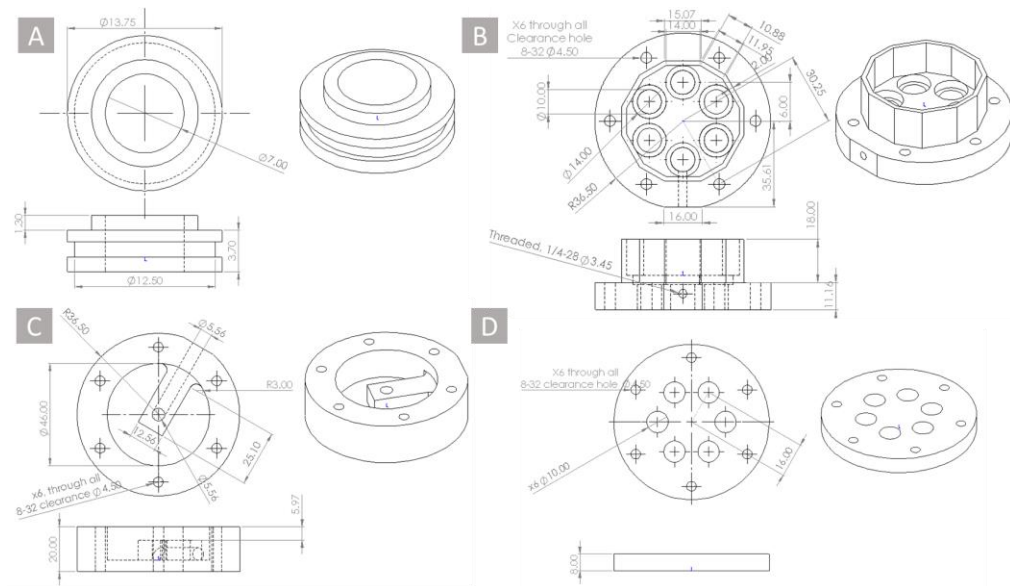
Figure 4-15 Technical drawings of CTCM parts. A- HDPE support ring with O-ring groove, B- Culture chamber, C- Air chamber, and D- middle plate.

Electrical connections and device cover:

A custom PCB was designed to integrate with the C-PACE-EM system and is shown in the figure below. Swiss machine headers outlets on the PCB are each connected to a graphite electrode via silver plated copper wires and 0-60 bronze screws that are threaded into the electrodes. The PCB fits into a 3D printed device cover. Cover dimensions and schematic of the electrode interface is shown in *Figure 4-16*.
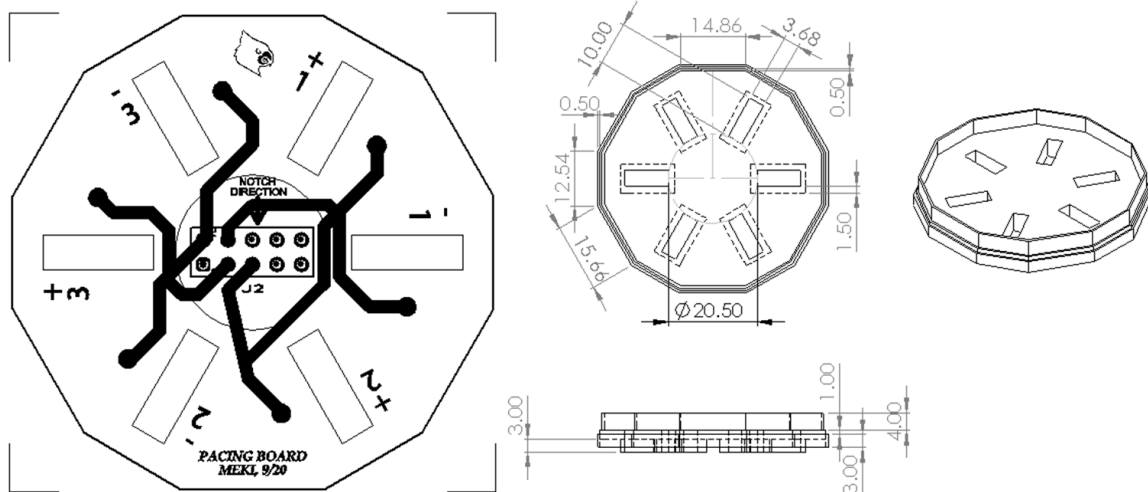
Figure 4-16 A- Custom interface PCB with C-PACE-EM system, B- 3D printed cover with sockets for 6 electrodes for electrically stimulating heart slices.

4.17.5 Heart slice movement assessment using MUSCLEMOTION

To obtain a movement trace of the heart slices, a custom camera system was developed. A DSLR camera (Cannon Rebel T7i, Cannon, Tokyo, Japan) was used with a Navitar Zoom 7000 18-108mm Macro Lens, (Navitar, San Francisco, CA). The camera was placed at a 51° angle and videos were recorded at 30 fps. First a mask was created using MATLAB (MathWorks, Natick, MA, USA) to define the region of interest which is the beating heart slice to avoid any noise from extraneous effects. The manually segmented mask was applied to all images in the frame sequence and then fed to the MUSCLEMOTION plugin. Briefly, MUSCLE motion uses the average pixel intensity within each frame to quantify its movement relative to a reference frame. The contraction data was recorded, filtered, and used to quantify the cycle time and assess the tissue movement. The process is shown in *Figure 4-17*.

Post processing of recorded videos was performed using a zero phase first order digital filter. To quantify the tissue movement (peak to peak), peak analysis was performed to distinguish the peaks and valleys of the recorded signal. Additionally, detrending was performed to remove signal drift using a 6th order polynomial. Software code was developed in MATLAB to detect overall tissue movement, cycle time, relaxation time, and contraction time.
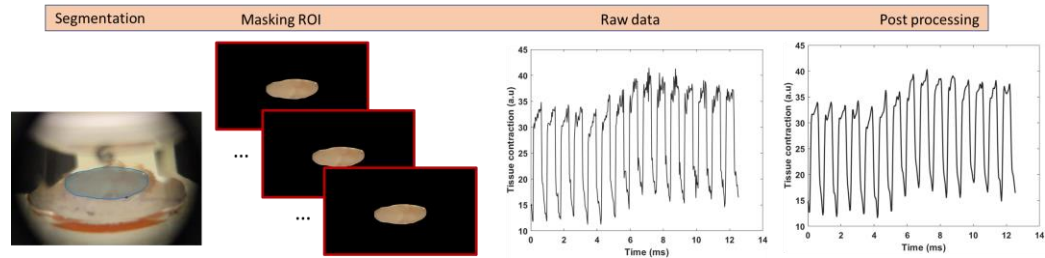
Figure 4-17 Assessment of heart slice movement in CTCM using MUSCLEMOTION with Image-J. Each frame was segmented and stacked. The stack was used to calculate the contraction data.

4.17.6 Quantification of tissue stretch during the cycle

To calculate the peak movement of the heart slices, frame-by-frame analysis was performed manually using Image J, (NIH, Washington DC, USA). The center point of the tissue was tracked manually at each frame and a peak trace was calculated with the aid of a reference length (the ring diameter, 7mm) and the camera incline. Pixel length measurements were converted using the following equation

$$S = \frac{L_m \ [pixels]}{L_{ref}[pixels] \times \cos(\emptyset)} \times 7 \ [mm] \tag{13}$$

Where S is the tissue peak movement in mm, L_m is the measured peak movement in pixels, L_{ref} is the ring diameter as in the frame in pixels, and $\emptyset$ is the camera inclination angle in degrees. Tissue movement was approximated a membrane movement that follows the equation [290]

$$y(r) = S \left(1 - \left(\frac{r}{R}\right)^2\right)^2 \tag{14}$$

Where y is the upwards deflection of the tissue at distance r from the center, S is the tissue peak movement at any frame, r is the distance from the center, and R is the tissue diameter.

Once the peak movement was determined at each frame, %area stretch was calculated using surface rotation of equation 14

$$\%stretch = (\pi R^2 - \int_0^R 2\pi r \sqrt{1 + \left(\frac{dy}{dr}\right)^2}\, dr)/\pi R^2 \times 100 \tag{15}$$

These calculations were performed using custom software written in MATLAB.

4.17.7 FEA to determine Electric field distribution in the culture chamber

ANSYS Workbench software was used to model and simulate the electrical field potential and electrical voltage within the culture chamber. Adaptive meshing optimized for electrical simulation was used and resulted in 10171 elements. The voltages at each electrode were used as inputs (4.0 V for positive, and 0 V for ground).

4.17.8 FEA to determine the strain field within the heart slice

Ansys Mechanical was used to simulate the strain field within the heart slices with SOLID 187 elements. Adaptive meshing was used and resulted in 2956 elements.

The circular tissue was modeled in 3-D with fixed support boundary conditions on the outer edge of the tissue. The peak central movement recorded with the camera system was used as reference for the FEA. To model the maximum strain on the tissue (end of diastole), the maximum center deflection was used which was calculated as 2.1 mm. Pressure was applied to the bottom of the tissue model equally. Large deflection setting was turned on to account for non-linear effects.

4.17.9 Immunohistochemical staining

Heart slice fixation, mounting and immunofluorescence:

Heart slices were fixed in 4% paraformaldehyde for 24 hours. Fixed tissue underwent dehydration in 30% sucrose overnight and was then embedded in optimal cutting temperature compound (OCT compound) and gradually frozen in isopentane/dry ice bath. OCT embedded blocks were stored at -80°C until sectioning. 8µm cross-sectional sections were cut and immune-stained for target proteins.

Immunofluorescent staining:

To remove the OCT, compound the slides were heated for 5 minutes at 95°C until the OCT compound melted. 1-2 ml of PBS were added to each slide and incubated at room temperature for 10-30 minutes until the OCT compound washed off. Sections were then permeabilized by incubating them for 30 minutes with 0.1% Triton-X in PBS at room temperature. Triton-X was washed with PBS and non-specific antibody binding in the sections was blocked by 3% BSA solution for 1 hour at room temperature. After washing BSA with PBS, the primary antibodies (1:100 dilution in 1% BSA) (Connexin 43 (Abcam; #AB11370), and Troponin-T (Thermo Scientific; #MA5-12960), were added

to the section for 90 minutes followed by the secondary antibodies (1:200 dilution in 1%

BSA) Anti-mouse Alexa Fluor 488 (Thermo Scientific; #A16079), Anti-rabbit Alexa

Fluor 594 (Thermo Scientific; #T6391) for another 90 minutes separated by 3 washes

with PBS. To distinguish the target staining from background, we used a secondary

antibody only as a control. Finally, the DAPI stain was added, and the slides were

mounted in vectashield (Vector Laboratories) and sealed with nail polish. For WGA

staining, WGA-Alexa Fluor 555 (Thermo Scientific; #W32464) was used at 5 µg/mL in

PBS and was applied to fixed sections for 10 minutes at room temperature, followed by

wash and addition of mounting media and nail polish sealant. All immunofluorescence

imaging and quantification was performed using a Cytation 1 high content imager and the

fluorescent signal quantification and masking was performed using the Gen5 software

4.17.10 Trichrome staining

Fixed slides were first heated for 10 minutes at 95 C to melt OCT. PBS was added

to each slide to remove any remaining OCT for 30 minutes. Slides were submersed in

Bouin's solution (Picric acid, Formaldehyde, and glacial acetic acid) overnight (12 hours)

to improve the staining quality. The slides were then rinsed with running tap water for 15

minutes to remove Bouin's solution yellow color. The slides were then stained in

Biebrich scarlet acid fuchsin (1% aqueous, 1% aqueous, and glacial acetic acid) solution

for 10 minutes and then washed running DI water. The slides were then differentiated in

phosphomolybdic-phosphotungstic acid solution (5%-5%) for another 10 minutes to

remove red color from collagen. Without rinsing, the slides are directly transferred into

aniline blue solution to stain for 10 minutes. Then the slides were rinsed again with DI

water and differentiated in 1% acetic acid solution for 2 minutes. After rinsing with

running DI water, the slides were dried in 200 proof ethyl alcohol and subsequently

transferred into xylene to clear off Biebrich scarlet-acid fuchsin staining. Mounting media

is then added, and coverslips are sealed on with nail polish.

4.17.11 MTT assay

CyQUANT™ MTT Cell Viability Assay (Invitrogen, Carlsbad, CA), catalogue #

V13154 was used according to the manufacturer's protocol with some modifications.

Briefly, a 6 mm surgical punch was to collect heart slice tissue to perform the MTT assay

and ensure similar tissue weights were used. The punches were each placed in a well of

12 well plate containing 0.9 ml of growth media with 0.1 ml of the reconstituted MTT

substrate according to the manufacturer's protocol. The tissues were incubated for 3

hours at 37°C and viable tissue metabolized the MTT substrate creating a purple color

formazan compound. To extract the purple formazan from the heart slices, The growth

medium was removed and 1 ml of DMSO was added to each tissue and incubated it at

37°C for 15 minutes, or until the tissue was translucent and no longer dark purple.

Samples were diluted 1:10 in DMSO and the intensity of the purple color was measured

using a Cytation plate reader (BioTek) at 570nm using a 96 well plate reader. The

readings were normalized to the weight of each heart slice and converted into OD/mg

tissue.

4.17.12 Statistical Analysis

Prism software (GraphPad, San Diego, CA) was used to perform all statistical

analysis. One way ANOVA was used to determine significance between multiple groups

with p-value cut off at 0.05 confidence interval. Kolmogorov–Smirnov test for normality

was first used to determine if parametric or non-parametric tests were warranted. To

compare between individual groups, Tukey HSD post hoc test was used.

CHAPTER 5: CONCLUSION

5.1 Summary

Cardiovascular diseases are responsible for the most mortality globally and in the United States. The ability to model different elements of the cardiovascular systems at different degrees of complexity offers great power in the search for appropriate treatment for cardiovascular diseases. In-silico simulations are gaining attention because of their ability to model many biological phenomena at a low cost. Cellular and tissue level models provide an adequate platform for basic science discovery as well as drug testing due to their versatility and high throughput. However, limitations for cell and tissue culture systems are clear when extraneous stimulants become relevant in the context of the desired experimental model. The complexity of the cardiovascular system exacerbates this limitation due to the presence of multiple factors that come into the regulation and maintenance of the normal homeostasis. (e.g., hemodynamic loading, neuro-hormonal factors, downstream feedback mechanisms, metabolic substrate, cell-cell interaction …, etc.). Unfortunately, this has resulted in cell and tissue-level studies with little physiological relevance.

In this dissertation, three models encompassing different components of the cardiovascular system at different degrees of complexity were used/ developed in their relevant application.

Firstly, an extensive lumped parameter model of the cardiovascular system was used to model the hemodynamics of blood flow. This *in-silico* model was used to help solve on the lingering problems with chronic mechanical circulatory support; that is physiological control of CFLVADs. A novel sensorless control algorithm was developed and tested using this model. Using the pump speed pulsatility the control algorithm was able to 1) Adjust pump flow to tissue demand, 2) avoid ventricular suction by over pumping, and 3) augment arterial pulsatility through the incorporation of a pulsatile mode. The sensorless algorithm avoids the use of implantable pressure or volume sensors that can drift or the use of unreliable model-based estimations. The use of computer simulation to develop this algorithm greatly sped up its optimization, which would have otherwise been time consuming.

The second problem addressed in this work was the choice of appropriate pulsatility augmentation strategy that can mitigate vascular adverse events caused by diminished pulsatility in CFLVAD flow. To address this, a microfluidic endothelial cell-smooth muscle cell model was developed to model the arterial vascular wall and simulate the hemodynamic loading it is subjected to. The results showed that pulse frequency and pulse magnitude are both relevant variables to the normalization of endothelial cells and smooth muscle cells morphology and that in the absence of stretch the effects of flow hemodynamics on cell morphology may only be communicated to smooth muscle cells through endothelial paracrine secretion. This model may be further used to identify relevant biomarkers to optimize the pulse flow modulation strategy.

Lastly, a cardiac tissue culture model that utilizes thin heart slices was developed. CTCM is a platform technology that provides a medium throughput system that can

replicate the electromechanical environment within the heart. The study with CTCM showed that humoral stimulation in the form of T3 and dexamethasone can further enhance the viability and structural integrity of heart slices in culture. The characterization and conceptual proof were demonstrated using CTCM and its ability to replicate diseased state was exemplified. The system can be used for drug discovery and study of various conditions associated with cardiovascular diseases.

In the context of CFLVAD, CTCM system can be used to test the effects of mechanical unloading on the heart muscles. It is well known that CFLVAD support can cause cardiac atrophy. Hence, pulse flow modulation strategies, in addition to augmenting arterial pulsatility, can be used to intermittently load and unload the native ventricle.

5.2 Future work

Pulsatility-based ΔRPM control:

In-silico simulations using a lumped parameter model showed the feasibility of this type of physiological control. Noting that there are no physiological control algorithms that are FDA-approved to date, further validation of this algorithm must be performed in-vitro using mock flow loop on physical pumps followed by animal studies.

Studying pulse flow modulation in EC-SMC coculture model:

The study conducted using EC-SMC coculture was restricted to the characterization of the system and the flow regime, stretch, and pressure within the culture chamber analytically and using CFD. Effects on ECs and SMCs were limited to morphological changes. In future work, it is necessary to interrogate the system by

investigating relevant biomarkers related to inflammatory response, oxidative stress, contractile protein expression, and paracrine signaling as well as full transcriptional profiling. This way the most relevant biomarkers can be narrowed down, studied, and used to optimize modulation strategies. Beyond pulse flow modulation assessment, EC-SMC coculture model provides an excellent tool to study tissue response to drug therapies in a physiologically relevant platform.

Electromechanical stimulation of heart slice tissue:

Future work using CTCM must include the use of human heart slices to confirm the study findings from pig heart slices. In the study, the CTCM system was extensively characterized by the assessment of cellular targets. In addition, the mechanical loading of the heart slices in terms of physiological strains. However, a major improvement to the system would be the addition of continuous monitoring of the active contraction of the individual heart slices. Further, quantification of changes in heart tissue stiffness is a good indicator of its composition and may provide a good and easy way to assess remodeling progression temporally.

Lastly, this system can be used extensively to study different pathological conditions. Molecular and cellular studies of myocardial slices can be investigated under these pathological conditions.

REFERENCES

[1]   M. H. Meki, J. M. Miller, and T. M. A. Mohamed, "Heart Slices to Model Cardiac Physiology," (in English), *Frontiers in Pharmacology,* Mini Review vol. 12, no. 23, 2021-February-04 2021, doi: 10.3389/fphar.2021.617922.

[2]   J. E. Hall, *Guyton and Hall textbook of medical physiology*, 13th edition. ed. Philadelphia, PA: Elsevier (in English), 2016.

[3]   J. C. Greenfield, "Circulatory Physiology: Cardiac Output and Its Regulation," *JAMA,* vol. 187, no. 3, 1964, doi: 10.1001/jama.1964.03060160066027.

[4]   H. Gray, T. P. Pick, R. Howden, T. P. Pick, and R. Howden, *Anatomy, descriptive and surgical*, Rev. American, from the 15th English ed. ed. New York: Gramercy Books (in English), 2000.

[5]   Y. C. Fung, *Biomechanics : circulation*. (in English), 2010.

[6]   J. C. Han, T. Pham, A. J. Taberner, D. S. Loiselle, and K. Tran, "Solving a century-old conundrum underlying cardiac force-length relations," (in eng), *Am J Physiol Heart Circ Physiol,* vol. 316, no. 4, pp. H781-h793, Apr 1 2019, doi: 10.1152/ajpheart.00763.2018.

[7]   J. G. Chaui-Berlinck and L. H. A. Monteiro, "Frank-Starling mechanism and short-term adjustment of cardiac flow," (in eng), *J Exp Biol,* vol. 220, no. Pt 23, pp. 4391-4398, Dec 1 2017, doi: 10.1242/jeb.167106.

[8]   H E Morgan *et al.*, "Biochemical Mechanisms of Cardiac Hypertrophy," *Annual Review of Physiology,* vol. 49, no. 1, pp. 533-543, 1987, doi: 10.1146/annurev.ph.49.030187.002533.

[9]   P. J. R. Barton *et al.*, "Myocardial Insulin-Like Growth Factor-I Gene Expression During Recovery From Heart Failure After Combined Left Ventricular Assist Device and Clenbuterol Therapy," *Circulation,* vol. 112, no. 9_supplement, pp. I-46-I-50, 2005, doi: doi:10.1161/01.CIRCULATIONAHA.105.525873.

[10]   F. Ye, F. Yuan, X. Li, N. Cooper, J. P. Tinney, and B. B. Keller, "Gene expression profiles in engineered cardiac tissues respond to mechanical loading and inhibition of tyrosine kinases," (in eng), *Physiological reports,* vol. 1, no. 5, p. e00078, Oct 2013, doi: 10.1002/phy2.78.

[11]   C. R. Haggart, E. G. Ames, J. K. Lee, and J. W. Holmes, "Effects of stretch and shortening on gene expression in intact myocardium," (in eng),

Physiological genomics, vol. 46, no. 2, pp. 57-65, Jan 15 2014, doi: 10.1152/physiolgenomics.00103.2013.

[12]   D. Sedmera, T. Pexieder, V. Rychterova, N. Hu, and E. B. Clark, "Remodeling of chick embryonic ventricular myoarchitecture under experimentally changed loading conditions," (in eng), *The Anatomical record,* vol. 254, no. 2, pp. 238-52, Feb 1 1999, doi: 10.1002/(sici)1097-0185(19990201)254:2<238::aid-ar10>3.0.co;2-v.

[13]   K. Tobita and B. B. Keller, "Right and left ventricular wall deformation patterns in normal and left heart hypoplasia chick embryos," (in eng), *Am J Physiol Heart Circ Physiol,* vol. 279, no. 3, pp. H959-69, Sep 2000, doi: 10.1152/ajpheart.2000.279.3.H959.

[14]   G. S. Hoffman, C. M. Weyand, and J. A. D. o. M. M. G. H. B. Mills, "Inflammatory Diseases of Blood Vessels," *Mayo Clinic Proceedings,* vol. 77, no. 12, pp. 1399-1399, 2002, doi: 10.4065/77.12.1398.

[15]   R. S. Vasan, M. G. Larson, and D. Levy, "Determinants of echocardiographic aortic root size. The Framingham Heart Study," (in eng), *Circulation,* vol. 91, no. 3, pp. 734-40, Feb 1 1995, doi: 10.1161/01.cir.91.3.734.

[16]   C. R. Ethier and C. A. Simmons, *Introductory biomechanics : from cells to organisms*, Octava impresión. ed. (Cambridge texts in biomedical engineering). Cambridge ;: Cambridge University Press (in English), 2013.

[17]   M. Sato and T. Ohashi, "Biorheological views of endothelial cell responses to mechanical stimuli," (in eng), *Biorheology,* vol. 42, no. 6, pp. 421-41, 2005.

[18]   Y. S. Li, J. H. Haga, and S. Chien, "Molecular basis of the effects of shear stress on vascular endothelial cells," (in eng), *Journal of biomechanics,* vol. 38, no. 10, pp. 1949-71, Oct 2005, doi: 10.1016/j.jbiomech.2004.09.030.

[19]   A. B. Fisher, S. Chien, A. I. Barakat, and R. M. Nerem, "Endothelial cellular response to altered shear stress," (in eng), *American journal of physiology. Lung cellular and molecular physiology,* vol. 281, no. 3, pp. L529-33, Sep 2001, doi: 10.1152/ajplung.2001.281.3.L529.

[20]   R. Steward, Jr., D. Tambe, C. C. Hardin, R. Krishnan, and J. J. Fredberg, "Fluid shear, intercellular stress, and endothelial cell alignment," *American journal of physiology. Cell physiology,* vol. 308, no. 8, pp. C657-C664, 2015, doi: 10.1152/ajpcell.00363.2014.

[21]   W. C. Aird, "Phenotypic heterogeneity of the endothelium: I. Structure, function, and mechanisms," (in eng), *Circ Res,* vol. 100, no. 2, pp. 158-73, Feb 2 2007, doi: 10.1161/01.RES.0000255691.76142.4a.

[22]   P. F. Davies, "Flow-mediated endothelial mechanotransduction," (in eng), *Physiol Rev,* vol. 75, no. 3, pp. 519-60, Jul 1995, doi: 10.1152/physrev.1995.75.3.519.

[23]   A. G. Passerini *et al.,* "Coexisting proinflammatory and antioxidative endothelial transcription profiles in a disturbed flow region of the adult porcine aorta," (in eng), *Proc Natl Acad Sci U S A,* vol. 101, no. 8, pp. 2482-7, Feb 24 2004, doi: 10.1073/pnas.0305938101.

[24]   T. W. Secomb, "Theoretical models for regulation of blood flow," (in eng), *Microcirculation,* vol. 15, no. 8, pp. 765-775, 2008, doi: 10.1080/10739680802350112.

[25]   J. P. Stegemann, H. Hong, and R. M. Nerem, "Mechanical, biochemical, and extracellular matrix effects on vascular smooth muscle cell phenotype," (in eng), *J Appl Physiol (1985),* vol. 98, no. 6, pp. 2321-7, Jun 2005, doi: 10.1152/japplphysiol.01114.2004.

[26]   J. D. Humphrey, "Mechanisms of arterial remodeling in hypertension: coupled roles of wall shear and intramural stress," (in eng), *Hypertension,* vol. 52, no. 2, pp. 195-200, Aug 2008, doi: 10.1161/hypertensionaha.107.103440.

[27]   Y. Shi, P. Lawford, and R. Hose, "Review of Zero-D and 1-D Models of Blood Flow in the Cardiovascular System," *BioMedical Engineering OnLine,* vol. 10, no. 1, p. 33, 2011/04/26 2011, doi: 10.1186/1475-925X-10-33.

[28]   K. Sagawa, R. K. Lie, and J. Schaefer, "Translation of Otto Frank's paper "Die Grundform des Arteriellen Pulses" Zeitschrift für Biologie 37: 483-526 (1899)," (in eng), *J Mol Cell Cardiol,* vol. 22, no. 3, pp. 253-4, Mar 1990, doi: 10.1016/0022-2828(90)91459-k.

[29]   N. Westerhof, J. W. Lankhaar, and B. E. Westerhof, "The arterial Windkessel," (in eng), *Med Biol Eng Comput,* vol. 47, no. 2, pp. 131-41, Feb 2009, doi: 10.1007/s11517-008-0359-2.

[30]   H. Liu *et al.*, "Multi-scale modeling of hemodynamics in the cardiovascular system," *Acta Mechanica Sinica,* vol. 31, no. 4, pp. 446-464, 2015/08/01 2015, doi: 10.1007/s10409-015-0416-7.

[31]   S. Zhou *et al.*, "A review on low-dimensional physics-based models of systemic arteries: application to estimation of central aortic pressure," *BioMedical Engineering OnLine,* vol. 18, no. 1, p. 41, 2019/04/02 2019, doi: 10.1186/s12938-019-0660-3.

[32]   G. A. Giridharan, M. Skliar, D. B. Olsen, and G. M. Pantalos, "Modeling and control of a brushless DC axial flow ventricular assist device," (in eng), *ASAIO J,* vol. 48, no. 3, pp. 272-289, 2002 May-Jun 2002, doi: 10.1097/00002480-200205000-00013.

[33]   M. Abdollahzade, C. S. Kim, N. Fazeli, B. A. Finegan, M. Sean McMurtry, and J. O. Hahn, "Data-driven lossy tube-load modeling of arterial tree: in-human study," (in eng), *J Biomech Eng,* vol. 136, no. 10, p. 101011, Oct 2014, doi: 10.1115/1.4028089.

[34] A. Petrou, M. Granegger, M. Meboldt, and M. Schmid Daners, "A Versatile Hybrid Mock Circulation for Hydraulic Investigations of Active and Passive Cardiovascular Implants," (in eng), *ASAIO J,* vol. 65, no. 5, pp. 495-502, 2019, doi: 10.1097/MAT.0000000000000851.

[35] G. A. Truskey, "Endothelial Cell Vascular Smooth Muscle Cell Co-Culture Assay For High Throughput Screening Assays For Discovery of Anti-Angiogenesis Agents and Other Therapeutic Molecules," (in eng), *Int J High Throughput Screen,* vol. 2010, no. 1, pp. 171-181, Oct 1 2010, doi: 10.2147/ijhts.S13459.

[36] R. T. Yen and Y. C. Fung, "Effect of velocity of distribution on red cell distribution in capillary blood vessels," (in eng), *Am J Physiol,* vol. 235, no. 2, pp. H251-7, Aug 1978, doi: 10.1152/ajpheart.1978.235.2.H251.

[37] G. W. Schmid-Schoenbein, Y. C. Fung, and B. W. Zweifach, "Vascular endothelium-leukocyte interaction; sticking shear force in venules," *Circulation Research,* vol. 36, no. 1, pp. 173-184, 1975, doi: doi:10.1161/01.RES.36.1.173.

[38] S. S. Shevkoplyas, S. C. Gifford, T. Yoshida, and M. W. Bitensky, "Prototype of an in vitro model of the microcirculation," (in eng), *Microvasc Res,* vol. 65, no. 2, pp. 132-6, Mar 2003, doi: 10.1016/s0026-2862(02)00034-1.

[39] U. M. Sonmez, Y.-W. Cheng, S. C. Watkins, B. L. Roman, and L. A. Davidson, "Endothelial Cell Polarization and Orientation to Flow in a Novel Microfluidic Multimodal Shear Stress Generator," *bioRxiv,* p. 2020.07.10.197244, 2020, doi: 10.1101/2020.07.10.197244.

[40] S. Z. Birol, R. Fucucuoglu, S. Cadirci, A. Sayi-Yazgan, and L. Trabzon, "Studying dynamic stress effects on the behaviour of THP-1 cells by microfluidic channels," *Scientific Reports,* vol. 11, no. 1, 2021, doi: 10.1038/s41598-021-93935-w.

[41] M. D. Frame, G. B. Chapman, Y. Makino, and I. H. Sarelius, "Shear stress gradient over endothelial cells in a curved microchannel system," (in eng), *Biorheology,* vol. 35, no. 4-5, pp. 245-61, Jul-Oct 1998, doi: 10.1016/s0006-355x(99)80009-2.

[42] C. S. Wallace, J. C. Champion, and G. A. Truskey, "Adhesion and function of human endothelial cells co-cultured on smooth muscle cells," (in eng), *Ann Biomed Eng,* vol. 35, no. 3, pp. 375-86, Mar 2007, doi: 10.1007/s10439-006-9230-5.

[43] J. J. Chiu, L. J. Chen, C. N. Chen, P. L. Lee, and C. I. Lee, "A model for studying the effect of shear stress on interactions between vascular endothelial cells and smooth muscle cells," (in eng), *J Biomech,* vol. 37, no. 4, pp. 531-9, Apr 2004, doi: 10.1016/j.jbiomech.2003.08.012.

[44] J. J. Chiu *et al.*, "Shear stress inhibits adhesion molecule expression in vascular endothelial cells induced by coculture with smooth muscle cells," (in eng), *Blood,* vol. 101, no. 7, pp. 2667-74, Apr 1 2003, doi: 10.1182/blood-2002-08-2560.

[45] G. E. Rainger, P. Stone, C. M. Morland, and G. B. Nash, "A novel system for investigating the ability of smooth muscle cells and fibroblasts to regulate adhesion of flowing leukocytes to endothelial cells," (in eng), *J Immunol Methods,* vol. 255, no. 1-2, pp. 73-82, Sep 1 2001, doi: 10.1016/s0022-1759(01)00427-6.

[46] M. F. Fillinger, L. N. Sampson, J. L. Cronenwett, R. J. Powell, and R. J. Wagner, "Coculture of endothelial cells and smooth muscle cells in bilayer and conditioned media models," (in eng), *J Surg Res,* vol. 67, no. 2, pp. 169-78, Feb 1 1997, doi: 10.1006/jsre.1996.4978.

[47] M. F. van Buul-Wortelboer, H. J. Brinkman, K. P. Dingemans, P. G. de Groot, W. G. van Aken, and J. A. van Mourik, "Reconstitution of the vascular wall in vitro. A novel model to study interactions between endothelial and smooth muscle cells," (in eng), *Exp Cell Res,* vol. 162, no. 1, pp. 151-8, Jan 1986, doi: 10.1016/0014-4827(86)90433-7.

[48] T. Ziegler, R. W. Alexander, and R. M. Nerem, "An endothelial cell-smooth muscle cell co-culture model for use in the investigation of flow effects on vascular biology," (in eng), *Ann Biomed Eng,* vol. 23, no. 3, pp. 216-25, May-Jun 1995, doi: 10.1007/bf02584424.

[49] K. Niwa, T. Kado, J. Sakai, and T. Karino, "The Effects of a Shear Flow on the Uptake of LDL and Acetylated LDL by an EC Monoculture and an EC–SMC Coculture," *Annals of Biomedical Engineering,* vol. 32, no. 4, pp. 537-543, 2004/04/01 2004, doi: 10.1023/B:ABME.0000019173.79939.54.

[50] Y. Wada *et al.*, "In vitro model of atherosclerosis using coculture of arterial wall cells and macrophage," (in eng), *Yonsei Med J,* vol. 41, no. 6, pp. 740-55, Dec 2000, doi: 10.3349/ymj.2000.41.6.740.

[51] J. C. Zhang, Q. Ruan, L. Paucz, A. Fabry, B. R. Binder, and J. Wojta, "Stimulation of tissue factor expression in human microvascular and macrovascular endothelial cells by cultured vascular smooth muscle cells in vitro," (in eng), *J Vasc Res,* vol. 36, no. 2, pp. 126-32, Mar-Apr 1999, doi: 10.1159/000025635.

[52] S. Heydarkhan-Hagvall, G. Helenius, B. R. Johansson, J. Y. Li, E. Mattsson, and B. Risberg, "Co-culture of endothelial cells and smooth muscle cells affects gene expression of angiogenic factors," (in eng), *J Cell Biochem,* vol. 89, no. 6, pp. 1250-9, Aug 15 2003, doi: 10.1002/jcb.10583.

[53] C. S. Wallace, S. A. Strike, and G. A. Truskey, "Smooth muscle cell rigidity and extracellular matrix organization influence endothelial cell spreading

and adhesion formation in coculture," (in eng), *Am J Physiol Heart Circ Physiol,* vol. 293, no. 3, pp. H1978-86, Sep 2007, doi: 10.1152/ajpheart.00618.2007.

[54]   L. Evensen *et al.*, "Mural cell associated VEGF is required for organotypic vessel formation," (in eng), *PLoS One,* vol. 4, no. 6, p. e5798, Jun 4 2009, doi: 10.1371/journal.pone.0005798.

[55]   L. E. Niklason *et al.*, "Functional arteries grown in vitro," (in eng), *Science,* vol. 284, no. 5413, pp. 489-93, Apr 16 1999, doi: 10.1126/science.284.5413.489.

[56]   B. C. Isenberg, C. Williams, and R. T. Tranquillo, "Small-diameter artificial arteries engineered in vitro," (in eng), *Circ Res,* vol. 98, no. 1, pp. 25-35, Jan 6 2006, doi: 10.1161/01.Res.0000196867.12470.84.

[57]   W. Liu *et al.*, "MR tagging demonstrates quantitative differences in regional ventricular wall motion in mice, rats, and men," (in eng), *Am J Physiol Heart Circ Physiol,* vol. 291, no. 5, pp. H2515-21, Nov 2006, doi: 10.1152/ajpheart.01016.2005.

[58]   G. Salama and G. C. Bett, "Sex differences in the mechanisms underlying long QT syndrome," (in eng), *Am J Physiol Heart Circ Physiol,* vol. 307, no. 5, pp. H640-8, Sep 1 2014, doi: 10.1152/ajpheart.00864.2013.

[59]   B. D. Guth *et al.*, "Considerations for an In Vitro, Cell-Based Testing Platform for Detection of Adverse Drug-Induced Inotropic Effects in Early Drug Development. Part 1: General Considerations for Development of Novel Testing Platforms," *Frontiers in Pharmacology,* vol. 10, 2019, doi: 10.3389/fphar.2019.00884.

[60]   D. Wang, C. Patel, C. Cui, and G.-X. Yan, "Preclinical assessment of drug-induced proarrhythmias: Role of the arterially perfused rabbit left ventricular wedge preparation," *Pharmacology & Therapeutics,* vol. 119, no. 2, pp. 141-151, 2008, doi: 10.1016/j.pharmthera.2008.02.009.

[61]   J. K. Gwathmey, K. Tsaioun, and R. J. Hajjar, "Cardionomics: a new integrative approach for screening cardiotoxicity of drug candidates," *Expert opinion on drug metabolism & toxicology,* vol. 5, no. 6, pp. 647-660, 2009.

[62]   J. M. Miller *et al.*, "Heart slice culture system reliably demonstrates clinical drug-related cardiotoxicity," *Toxicology and Applied Pharmacology,* vol. 406, p. 115213, 2020, doi: 10.1016/j.taap.2020.115213.

[63]   S. P. Halbert, R. Bruderer, and A. Thompson, "Growth of dissociated beating human heart cells in tissue culture," *Life Sciences,* vol. 13, no. 7, pp. 969-975, 1973/10/01/ 1973, doi: https://doi.org/10.1016/0024-3205(73)90087-8.

[64]   I. Harary and B. Farley, "In vitro studies on single beating rat heart cells: I. Growth and organization," *Experimental Cell Research,* vol. 29, no. 3, pp. 451-465, 1963/02/01/ 1963, doi: https://doi.org/10.1016/S0014-4827(63)80008-7.

[65]   S. Halbert and R. Bruderer, "STUDIES ON IN-VITRO GROWTH OF DISSOCIATED BEATING RAT AND HUMAN HEART CELLS," in *Circulation*, 1971, vol. 44, no. 4: LIPPINCOTT WILLIAMS & WILKINS 227 EAST WASHINGTON SQ, PHILADELPHIA, PA 19106, pp. 174-&.

[66]   T. Powell and V. W. Twist, "A rapid technique for the isolation and purification of adult cardiac muscle cells having respiratory control and a tolerance to calcium," *Biochemical and Biophysical Research Communications,* vol. 72, no. 1, pp. 327-333, 1976/09/07/ 1976, doi: https://doi.org/10.1016/0006-291X(76)90997-9.

[67]   Q. Ke *et al.*, "Electrophysiological properties of cardiomyocytes isolated from CYP2J2 transgenic mice," (in eng), *Mol Pharmacol,* vol. 72, no. 4, pp. 1063-1073, 2007, doi: 10.1124/mol.107.035881.

[68]   D. J. Beuckelmann and W. G. Wier, "Mechanism of release of calcium from sarcoplasmic reticulum of guinea-pig cardiac cells," (in eng), *J Physiol,* vol. 405, pp. 233-255, 1988, doi: 10.1113/jphysiol.1988.sp017331.

[69]   M. R. N. Celes *et al.*, "Disruption of Calcium Homeostasis in Cardiomyocytes Underlies Cardiac Structural and Functional Changes in Severe Sepsis," vol. 8, no. 7, p. e68809, 2013, doi: 10.1371/journal.pone.0068809.

[70]   P. A. Gorski, C. Kho, and J. G. Oh, "Measuring Cardiomyocyte Contractility and Calcium Handling In Vitro," (in eng), *Methods Mol Biol,* vol. 1816, pp. 93-104, 2018, doi: 10.1007/978-1-4939-8597-5_7.

[71]   D. J. Beuckelmann, M. Näbauer, and E. Erdmann, "Intracellular calcium handling in isolated ventricular myocytes from patients with terminal heart failure," (in eng), *Circulation,* vol. 85, no. 3, pp. 1046-55, Mar 1992, doi: 10.1161/01.cir.85.3.1046.

[72]   J. Judd, J. Lovas, and G. N. Huang, "Isolation, Culture and Transduction of Adult Mouse Cardiomyocytes," *Journal of Visualized Experiments,* no. 114, 2016, doi: 10.3791/54012.

[73]   F. d. Monte *et al.*, "Restoration of Contractile Function in Isolated Cardiomyocytes From Failing Human Hearts by Gene Transfer of SERCA2a," *Circulation,* vol. 100, no. 23, pp. 2308-2311, 1999, doi: doi:10.1161/01.CIR.100.23.2308.

[74]   S. S. Parikh, S. Z. Zou, and L. Tung, "Contraction and relaxation of isolated cardiac myocytes of the frog under varying mechanical loads," (in eng), *Circ Res,* vol. 72, no. 2, pp. 297-311, Feb 1993, doi: 10.1161/01.res.72.2.297.

[75]   R. Gilsbach *et al.*, "Dynamic DNA methylation orchestrates cardiomyocyte development, maturation and disease," (in eng), *Nat Commun,* vol. 5, p. 5288, Oct 22 2014, doi: 10.1038/ncomms6288.

[76]   J. Mitcheson, "Cultured adult cardiac myocytes Future applications, culture methods, morphological and electrophysiological properties," *Cardiovascular Research,* vol. 39, no. 2, pp. 280-300, 1998, doi: 10.1016/s0008-6363(98)00128-x.

[77]   S. D. Bird *et al.*, "The human adult cardiomyocyte phenotype," *Cardiovascular Research,* vol. 58, no. 2, pp. 423-434, 2003, doi: 10.1016/s0008-6363(03)00253-0.

[78]   K. Dipla, J. A. Mattiello, V. Jeevanandam, S. R. Houser, and K. B. Margulies, "Myocyte recovery after mechanical circulatory support in humans with end-stage heart failure," (in eng), *Circulation,* vol. 97, no. 23, pp. 2316-22, Jun 16 1998, doi: 10.1161/01.cir.97.23.2316.

[79]   J. Tytgat, "How to isolate cardiac myocytes," (in eng), *Cardiovasc Res,* vol. 28, no. 2, pp. 280-3, Feb 1994, doi: 10.1093/cvr/28.2.280.

[80]   D. Dobrev *et al.*, "G-Protein beta(3)-subunit 825T allele is associated with enhanced human atrial inward rectifier potassium currents," (in eng), *Circulation,* vol. 102, no. 6, pp. 692-7, Aug 8 2000, doi: 10.1161/01.cir.102.6.692.

[81]   G.-R. Guo, L. Chen, M. Rao, K. Chen, J.-P. Song, and S.-S. Hu, "A modified method for isolation of human cardiomyocytes to model cardiac diseases," *J Transl Med,* vol. 16, no. 1, 2018, doi: 10.1186/s12967-018-1649-6.

[82]   N. I. Callaghan *et al.*, "Functional culture and in vitro genetic and small-molecule manipulation of adult mouse cardiomyocytes," *Communications Biology,* vol. 3, no. 1, 2020, doi: 10.1038/s42003-020-0946-9.

[83]   K. Takahashi *et al.*, "Induction of pluripotent stem cells from adult human fibroblasts by defined factors," *cell,* vol. 131, no. 5, pp. 861-872, 2007.

[84]   O. Sirenko, E. F. Cromwell, C. Crittenden, J. A. Wignall, F. A. Wright, and I. Rusyn, "Assessment of beating parameters in human induced pluripotent stem cells enables quantitative in vitro screening for cardiotoxicity," *Toxicology and applied pharmacology,* vol. 273, no. 3, pp. 500-507, 2013.

[85]   A. Pointon *et al.*, "Assessment of cardiomyocyte contraction in human-induced pluripotent stem cell-derived cardiomyocytes," *Toxicological Sciences,* vol. 144, no. 2, pp. 227-237, 2015.

[86]   A. Sharma *et al.*, "Use of human induced pluripotent stem cell-derived cardiomyocytes to assess drug cardiotoxicity," (in eng), *Nat Protoc,* vol. 13, no. 12, pp. 3018-3041, 2018, doi: 10.1038/s41596-018-0076-8.

[87] G. Jung and D. Bernstein, "hiPSC Modeling of Inherited Cardiomyopathies," (in eng), *Curr Treat Options Cardiovasc Med,* vol. 16, no. 7, p. 320, Jul 2014, doi: 10.1007/s11936-014-0320-7.

[88] C. Yang *et al.*, "Concise Review: Cardiac Disease Modeling Using Induced Pluripotent Stem Cells," (in eng), *Stem Cells,* vol. 33, no. 9, pp. 2643-51, Sep 2015, doi: 10.1002/stem.2070.

[89] C. Denning *et al.*, "Cardiomyocytes from human pluripotent stem cells: From laboratory curiosity to industrial biomedical platform," *Biochimica et Biophysica Acta (BBA) - Molecular Cell Research,* vol. 1863, no. 7, Part B, pp. 1728-1748, 2016/07/01/ 2016, doi: https://doi.org/10.1016/j.bbamcr.2015.10.014.

[90] R. E. Ahmed, T. Anzai, N. Chanthra, and H. Uosaki, "A Brief Review of Current Maturation Methods for Human Induced Pluripotent Stem Cells-Derived Cardiomyocytes," *Frontiers in Cell and Developmental Biology,* vol. 8, 2020, doi: 10.3389/fcell.2020.00178.

[91] M. A. Roberts *et al.*, "Stromal Cells in Dense Collagen Promote Cardiomyocyte and Microvascular Patterning in Engineered Human Heart Tissue," *Tissue Engineering Part A,* vol. 22, no. 7-8, pp. 633-644, 2016, doi: 10.1089/ten.tea.2015.0482.

[92] D. Zhang, I. Y. Shadrin, J. Lam, H. Q. Xian, H. R. Snodgrass, and N. Bursac, "Tissue-engineered cardiac patch for advanced functional maturation of human ESC-derived cardiomyocytes," (in eng), *Biomaterials,* vol. 34, no. 23, pp. 5813-20, Jul 2013, doi: 10.1016/j.biomaterials.2013.04.026.

[93] Y. S. Zhang *et al.*, "Bioprinting 3D microfibrous scaffolds for engineering endothelialized myocardium and heart-on-a-chip," (in eng), *Biomaterials,* vol. 110, pp. 45-59, 2016, doi: 10.1016/j.biomaterials.2016.09.003.

[94] S. S. Nunes *et al.*, "Biowire: a platform for maturation of human pluripotent stem cell–derived cardiomyocytes," *Nature Methods,* vol. 10, no. 8, pp. 781-787, 2013, doi: 10.1038/nmeth.2524.

[95] N. Tandon *et al.*, "Electrical stimulation systems for cardiac tissue engineering," *Nat Protoc,* vol. 4, no. 2, pp. 155-173, 2009/02/01 2009, doi: 10.1038/nprot.2008.183.

[96] J. L. Ruan *et al.*, "Mechanical Stress Conditioning and Electrical Stimulation Promote Contractility and Force Maturation of Induced Pluripotent Stem Cell-Derived Human Cardiac Tissue," (in eng), *Circulation,* vol. 134, no. 20, pp. 1557-1567, Nov 15 2016, doi: 10.1161/circulationaha.114.014998.

[97] K. Ronaldson-Bouchard *et al.*, "Advanced maturation of human cardiac tissue grown from pluripotent stem cells," *Nature,* vol. 556, no. 7700, pp. 239-243, 2018/04/01 2018, doi: 10.1038/s41586-018-0016-3.

[98] C. P. Jackman, A. L. Carlson, and N. Bursac, "Dynamic culture yields engineered myocardium with near-adult functional output," (in eng), *Biomaterials,* vol. 111, pp. 66-79, Dec 2016, doi: 10.1016/j.biomaterials.2016.09.024.

[99] K. Kroll, M. Chabria, K. Wang, F. Häusermann, F. Schuler, and L. Polonchuk, "Electro-mechanical conditioning of human iPSC-derived cardiomyocytes for translational research," *Progress in Biophysics and Molecular Biology,* vol. 130, pp. 212-222, 2017/11/01/ 2017, doi: https://doi.org/10.1016/j.pbiomolbio.2017.07.003.

[100] K. H. Benam *et al.,* "Engineered In Vitro Disease Models," *Annual Review of Pathology: Mechanisms of Disease,* vol. 10, no. 1, pp. 195-262, 2015, doi: 10.1146/annurev-pathol-012414-040418.

[101] Y. Zhao *et al.,* "Towards chamber specific heart-on-a-chip for drug testing applications," (in eng), *Adv Drug Deliv Rev,* vol. 165-166, pp. 60-76, 2020, doi: 10.1016/j.addr.2019.12.002.

[102] B. Zhang, A. Korolj, B. F. L. Lai, and M. Radisic, "Advances in organ-on-a-chip engineering," *Nature Reviews Materials,* vol. 3, no. 8, pp. 257-278, 2018/08/01 2018, doi: 10.1038/s41578-018-0034-7.

[103] K. Ronaldson-Bouchard and G. Vunjak-Novakovic, "Organs-on-a-Chip: A Fast Track for Engineered Human Tissues in Drug Development," (in eng), *Cell Stem Cell,* vol. 22, no. 3, pp. 310-324, 2018, doi: 10.1016/j.stem.2018.02.011.

[104] G.-X. Yan and C. Antzelevitch, "Cellular Basis for the Electrocardiographic J Wave," *Circulation,* vol. 93, no. 2, pp. 372-379, 1996, doi: doi:10.1161/01.CIR.93.2.372.

[105] G.-X. Yan, W. Shimizu, and C. Antzelevitch, "Characteristics and Distribution of M Cells in Arterially Perfused Canine Left Ventricular Wedge Preparations," *Circulation,* vol. 98, no. 18, pp. 1921-1927, 1998, doi: 10.1161/01.cir.98.18.1921.

[106] C. O'Shea *et al.,* "Cardiac Optogenetics and Optical Mapping – Overcoming Spectral Congestion in All-Optical Cardiac Electrophysiology," (in English), *Frontiers in Physiology,* Review vol. 10, no. 182, 2019-March-07 2019, doi: 10.3389/fphys.2019.00182.

[107] A. V. Glukhov *et al.,* "Transmural dispersion of repolarization in failing and nonfailing human ventricle," (in eng), *Circulation research,* vol. 106, no. 5, pp. 981-991, 2010, doi: 10.1161/CIRCRESAHA.109.204891.

[108] Q. Lou, V. V. Fedorov, A. V. Glukhov, N. Moazami, V. G. Fast, and I. R. Efimov, "Transmural heterogeneity and remodeling of ventricular excitation-contraction coupling in human heart failure," (in eng),

Circulation, vol. 123, no. 17, pp. 1881-1890, 2011, doi: 10.1161/CIRCULATIONAHA.110.989707.

[109] X. Chen, J. S. Cordes, J. A. Bradley, Z. Sun, and J. Zhou, "Use of arterially perfused rabbit ventricular wedge in predicting arrhythmogenic potentials of drugs," (in eng), *J Pharmacol Toxicol Methods,* vol. 54, no. 3, pp. 261-72, Nov-Dec 2006, doi: 10.1016/j.vascn.2006.02.005.

[110] Y. Qiao *et al.,* "Multiparametric slice culture platform for the investigation of human cardiac tissue physiology," *Progress in Biophysics and Molecular Biology,* vol. 144, pp. 139-150, 2019, doi: 10.1016/j.pbiomolbio.2018.06.001.

[111] C. Kang *et al.,* "Human Organotypic Cultured Cardiac Slices: New Platform For High Throughput Preclinical Human Trials," *Sci Rep,* vol. 6, p. 28798, Jun 30 2016, doi: 10.1038/srep28798.

[112] A. R. Parrish *et al.,* "Organ Culture of Rat Myocardial Slices: An Alternative in Vitro Tool in Organ-Specific Toxicology," *Toxicology Methods,* vol. 2, no. 2, pp. 101-111, 1992/01/01 1992, doi: 10.3109/15376519209087715.

[113] M. Brandenburger *et al.,* "Organotypic slice culture from human adult ventricular myocardium," *Cardiovasc Res,* vol. 93, no. 1, pp. 50-9, Jan 1 2012, doi: 10.1093/cvr/cvr259.

[114] S. A. Watson, M. Scigliano, I. Bardi, R. Ascione, C. M. Terracciano, and F. Perbellini, "Preparation of viable adult ventricular myocardial slices from large and small mammals," *Nat Protoc,* vol. 12, no. 12, pp. 2623-2639, 2017, doi: 10.1038/nprot.2017.139.

[115] V. Talman and R. Kivelä, "Cardiomyocyte—Endothelial Cell Interactions in Cardiac Remodeling and Regeneration," (in English), *Frontiers in Cardiovascular Medicine,* Mini Review vol. 5, no. 101, 2018-July-26 2018, doi: 10.3389/fcvm.2018.00101.

[116] S. Yoshida *et al.,* "Maturation of Human Induced Pluripotent Stem Cell-Derived Cardiomyocytes by Soluble Factors from Human Mesenchymal Stem Cells," *Molecular Therapy,* vol. 26, no. 11, pp. 2681-2695, 2018, doi: 10.1016/j.ymthe.2018.08.012.

[117] S. A. Watson *et al.,* "Biomimetic electromechanical stimulation to maintain adult myocardial slices in vitro," *Nat Commun,* vol. 10, no. 1, p. 2168, May 15 2019, doi: 10.1038/s41467-019-10175-3.

[118] Q. Ou *et al.,* "Slicing and Culturing Pig Hearts under Physiological Conditions," *J Vis Exp,* no. 157, Mar 20 2020, doi: 10.3791/60913.

[119] F. Perbellini *et al.,* "Investigation of cardiac fibroblasts using myocardial slices," *Cardiovascular Research,* vol. 114, no. 1, pp. 77-89, 2018, doi: 10.1093/cvr/cvx152.

[120] Q. Ou *et al.*, "Physiological Biomimetic Culture System for Pig and Human Heart Slices," *Circulation Research,* vol. 125, no. 6, pp. 628-642, 2019, doi: doi:10.1161/CIRCRESAHA.119.314996.

[121] C. Fischer *et al.*, "Long-term functional and structural preservation of precision-cut human myocardium under continuous electromechanical stimulation in vitro," *Nature Communications,* vol. 10, no. 1, 2019, doi: 10.1038/s41467-018-08003-1.

[122] K. Y. Ye and L. D. Black, 3rd, "Strategies for tissue engineering cardiac constructs to affect functional repair following myocardial infarction," (in eng), *J Cardiovasc Transl Res,* vol. 4, no. 5, pp. 575-591, 2011, doi: 10.1007/s12265-011-9303-1.

[123] M. N. Hirt *et al.*, "Functional improvement and maturation of rat and human engineered heart tissue by chronic electrical stimulation," *Journal of Molecular and Cellular Cardiology,* vol. 74, pp. 151-161, 2014, doi: 10.1016/j.yjmcc.2014.05.009.

[124] T. M. Mohamed *et al.*, "Chemical Enhancement of In Vitro and In Vivo Direct Cardiac Reprogramming," (in eng), *Circulation,* vol. 135, no. 10, pp. 978-995, Mar 2017, doi: 10.1161/CIRCULATIONAHA.116.024692.

[125] T. M. A. Mohamed *et al.*, "Regulation of Cell Cycle to Stimulate Adult Cardiomyocyte Proliferation and Cardiac Regeneration," *Cell,* vol. 173, no. 1, pp. 104-116 e12, Mar 22 2018, doi: 10.1016/j.cell.2018.02.014.

[126] H. Yamakawa *et al.*, "Fibroblast Growth Factors and Vascular Endothelial Growth Factor Promote Cardiac Reprogramming under Defined Conditions," (in eng), *Stem Cell Reports,* vol. 5, no. 6, pp. 1128-1142, Dec 8 2015, doi: 10.1016/j.stemcr.2015.10.019.

[127] F. J. Giordano, "Oxygen, oxidative stress, hypoxia, and heart failure," *Journal of Clinical Investigation,* vol. 115, no. 3, pp. 500-508, 2005, doi: 10.1172/jci24408.

[128] F. G. Pitoulis, S. A. Watson, F. Perbellini, and C. M. Terracciano, "Myocardial slices come to age: an intermediate complexity in vitro cardiac model for translational research," *Cardiovascular Research,* vol. 116, no. 7, pp. 1275-1287, 2020, doi: 10.1093/cvr/cvz341.

[129] S. S. Virani *et al.*, "Heart Disease and Stroke Statistics—2021 Update: A Report From the American Heart Association," *Circulation,* 2021, doi: 10.1161/cir.0000000000000950.

[130] R. Gindi, "Health, United States, 2019," Centers for Disease Control and Prevention (U.S.), 2021. [Online]. Available: https://dx.doi.org/10.15620/cdc:100685

[131] A. J. Lusis, "Atherosclerosis," (in eng), *Nature,* vol. 407, no. 6801, pp. 233-41, Sep 14 2000, doi: 10.1038/35025203.

[132] J. Segovia Cubero, L. Alonso-Pulpón Rivera, R. Peraira Moral, and L. Silva Melchor, "Heart Failure: Etiology and Approach to Diagnosis," *Revista Española de Cardiología (English Edition),* 10.1016/S1885-5857(06)60143-6 vol. 57, no. 3, pp. 250-259, 2004, doi: 10.1016/S1885-5857(06)60143-6.

[133] W. J. Remme, K. Swedberg, T. F. f. t. Diagnosis, and E. S. o. C. Treatment of Chronic Heart Failure, "Guidelines for the diagnosis and treatment of chronic heart failure," *European Heart Journal,* vol. 22, no. 17, pp. 1527-1560, 2001, doi: 10.1053/euhj.2001.2783.

[134] M. Metra and J. R. Teerlink, "Heart failure," *The Lancet,* vol. 390, no. 10106, pp. 1981-1995, 2017, doi: 10.1016/S0140-6736(17)31071-1.

[135] R. W. Schrier, "Role of diminished renal function in cardiovascular mortality: marker or pathogenetic factor?," (in eng), *J Am Coll Cardiol,* vol. 47, no. 1, pp. 1-8, Jan 3 2006, doi: 10.1016/j.jacc.2005.07.067.

[136] P. A. McKee, W. P. Castelli, P. M. McNamara, and W. B. Kannel, "The Natural History of Congestive Heart Failure: The Framingham Study," *New England Journal of Medicine,* vol. 285, no. 26, pp. 1441-1446, 1971, doi: 10.1056/nejm197112232852601.

[137] S. P. Murphy, N. E. Ibrahim, and J. L. Januzzi, "Heart Failure With Reduced Ejection Fraction," *JAMA,* vol. 324, no. 5, p. 488, 2020, doi: 10.1001/jama.2020.10262.

[138] C. W. Yancy *et al.*, "2017 ACC/AHA/HFSA Focused Update of the 2013 ACCF/AHA Guideline for the Management of Heart Failure: A Report of the American College of Cardiology/American Heart Association Task Force on Clinical Practice Guidelines and the Heart Failure Society of America," *Circulation,* vol. 136, no. 6, pp. e137-e161, 2017, doi: doi:10.1161/CIR.0000000000000509.

[139] "Nomenclature and Criteria for Diagnosis of Diseases of the Heart and Blood Vessels," *Journal of the American Medical Association,* vol. 153, no. 9, pp. 891-891, 1953, doi: 10.1001/jama.1953.02940260115033.

[140] W. T. Abraham and D. L. Hayes, "Cardiac Resynchronization Therapy for Heart Failure," *Circulation,* vol. 108, no. 21, pp. 2596-2603, 2003, doi: doi:10.1161/01.CIR.0000096580.26969.9A.

[141] E. J. Benjamin *et al.*, "Heart Disease and Stroke Statistics—2017 Update: A Report From the American Heart Association," *Circulation,* 10.1161/CIR.0000000000000485 2017. [Online]. Available: http://circ.ahajournals.org/content/early/2017/01/25/CIR.0000000000000485.abstract.

[142] M. Jessup and S. Brozena, "Heart Failure," *New England Journal of Medicine,* vol. 348, no. 20, pp. 2007-2018, 2003, doi: 10.1056/nejmra021498.

[143] A. Cheng, C. A. Williamitis, and M. S. Slaughter, "Comparison of continuous-flow and pulsatile-flow left ventricular assist devices: is there an advantage to pulsatility?," (in eng), *Ann Cardiothorac Surg,* vol. 3, no. 6, pp. 573-581, 2014, doi: 10.3978/j.issn.2225-319X.2014.08.24.

[144] D. Barić, "Why pulsatility still matters: a review of current knowledge," (in eng), *Croat Med J,* vol. 55, no. 6, pp. 609-620, 2014, doi: 10.3325/cmj.2014.55.609.

[145] J. K. Kirklin *et al.*, "Eighth annual INTERMACS report: Special focus on framing the impact of adverse events," *The Journal of Heart and Lung Transplantation,* vol. 36, no. 10, pp. 1080-1086, 2017, doi: 10.1016/j.healun.2017.07.005.

[146] M. R. Mehra *et al.*, "A Fully Magnetically Levitated Circulatory Pump for Advanced Heart Failure," (in eng), *N Engl J Med,* vol. 376, no. 5, pp. 440-450, Feb 2 2017, doi: 10.1056/NEJMoa1610426.

[147] M. Kuehl and J. Garbade, "The evolution of left ventricular assist devices-a moment to reflect," (in eng), *J Thorac Dis,* vol. 9, no. 5, pp. E492-E494, 2017, doi: 10.21037/jtd.2017.03.72.

[148] S. Crow *et al.*, "Gastrointestinal bleeding rates in recipients of nonpulsatile and pulsatile left ventricular assist devices," (in eng), *The Journal of thoracic and cardiovascular surgery,* vol. 137, no. 1, pp. 208-15, Jan 2009, doi: 10.1016/j.jtcvs.2008.07.032.

[149] R. John, "Current axial-flow devices--the HeartMate II and Jarvik 2000 left ventricular assist devices," (in eng), *Seminars in thoracic and cardiovascular surgery,* vol. 20, no. 3, pp. 264-72, Fall 2008, doi: 10.1053/j.semtcvs.2008.08.001.

[150] S. C. Koenig, G. M. Pantalos, K. J. Gillars, D. L. Ewert, K. N. Litwak, and S. W. Etoch, "Hemodynamic and pressure-volume responses to continuous and pulsatile ventricular assist in an adult mock circulation," (in eng), *ASAIO J,* vol. 50, no. 1, pp. 15-24, Jan-Feb 2004, doi: 10.1097/01.mat.0000104816.50277.eb.

[151] M. Loebe *et al.*, "Inflammatory response after implantation of a left ventricular assist device: comparison between the axial flow MicroMed DeBakey VAD and the pulsatile Novacor device," (in eng), *ASAIO J,* vol. 47, no. 3, pp. 272-4, May-Jun 2001, doi: 10.1097/00002480-200105000-00023.

[152] M. S. Slaughter *et al.*, "Advanced heart failure treated with continuous-flow left ventricular assist device," (in eng), *N Engl J Med,* vol. 361, no. 23, pp. 2241-51, Dec 3 2009, doi: 10.1056/NEJMoa0909938.

[153] T. S. Kato *et al.*, "Effects of continuous-flow versus pulsatile-flow left ventricular assist devices on myocardial unloading and remodeling," (in

eng), *Circ Heart Fail,* vol. 4, no. 5, pp. 546-553, 2011, doi: 10.1161/CIRCHEARTFAILURE.111.962142.

[154] J. Grinstein, R. Torii, C. V. Bourantas, and H. M. Garcia-Garcia, "Left Ventricular Assist Device Flow Pattern Analysis Using a Novel Model Incorporating Left Ventricular Pulsatility," *ASAIO Journal,* vol. 67, no. 7, 2021. [Online]. Available: https://journals.lww.com/asaiojournal/Fulltext/2021/07000/Left_Ventricular_Assist_Device_Flow_Pattern.3.aspx.

[155] "Unknown article," doi: 10.1007/978-1-59745-443-8_16.

[156] W. Shi *et al.*, "Development of an Auto Calibration Method for the Implantable Blood Pressure Sensor in the Undulation pump ventricular assist device (UPVAD)," in *7th Asian-Pacific Conference on Medical and Biological Engineering*, Berlin, Heidelberg, Y. Peng and X. Weng, Eds., 2008// 2008: Springer Berlin Heidelberg, pp. 66-69.

[157] L. Brancato, G. Keulemans, T. Verbelen, B. Meyns, and R. Puers, "An Implantable Intravascular Pressure Sensor for a Ventricular Assist Device," *Micromachines,* vol. 7, no. 8, pp. 135-151, 2016, doi: 10.3390/mi7080135.

[158] L. Liang *et al.*, "A suction index based control system for rotary blood pumps," *Biomedical Signal Processing and Control,* vol. 62, p. 102057, 2020/09/01/ 2020, doi: https://doi.org/10.1016/j.bspc.2020.102057.

[159] M. Meki, Y. Wang, P. Sethu, M. Ghazal, A. El-Baz, and G. Giridharan, "A Sensorless Rotational Speed-Based Control System for Continuous Flow Left Ventricular Assist Devices," *IEEE Transactions on Biomedical Engineering,* vol. 67, no. 4, pp. 1050-1060, 2020, doi: 10.1109/TBME.2019.2928826.

[160] K. Fukamachi *et al.*, "Preload Sensitivity in Cardiac Assist Devices," *The Annals of thoracic surgery,* vol. 95, no. 1, pp. 373-380, 12/25 2013, doi: 10.1016/j.athoracsur.2012.07.077.

[161] H. A. Khalil, W. E. Cohn, R. W. Metcalfe, and O. H. Frazier, "Preload sensitivity of the Jarvik 2000 and HeartMate II left ventricular assist devices," (in eng), *ASAIO J,* vol. 54, no. 3, pp. 245-8, May-Jun 2008, doi: 10.1097/MAT.0b013e318173e0f4.

[162] L. E. Couperus *et al.*, "Pump Speed Optimization in Stable Patients with a Left Ventricular Assist Device," *ASAIO Journal,* vol. 63, no. 3, pp. 266-272, 2017, doi: 10.1097/mat.0000000000000483.

[163] N. Uriel *et al.*, "Long Term Outcomes for LVAD Patients Who Underwent Speed Optimization Using Pre-Discharge Ramp Test," *The Journal of Heart and Lung Transplantation,* vol. 32, no. 4, Supplement, p. S182, 2013/04/01/ 2013, doi: https://doi.org/10.1016/j.healun.2013.01.439.

[164] N. Uriel *et al.*, "Development of a Novel Echocardiography Ramp Test for Speed Optimization and Diagnosis of Device Thrombosis in Continuous-

Flow Left Ventricular Assist Devices: The Columbia Ramp Study," *Journal of the American College of Cardiology,* vol. 60, no. 18, pp. 1764-1775, 2012/10/30/ 2012, doi: https://doi.org/10.1016/j.jacc.2012.07.052.

[165] Y. Wang and M. A. Simaan, "A Suction Detection System for Rotary Blood Pumps Based on the Lagrangian Support Vector Machine Algorithm," *IEEE Journal of Biomedical and Health Informatics,* vol. 17, no. 3, pp. 654-663, 2013, doi: 10.1109/TITB.2012.2228877.

[166] M. Vollkron, H. Schima, L. Huber, R. Benkowski, G. Morello, and G. Wieselthaler, "Development of a suction detection system for axial blood pumps," (in eng), *Artificial organs,* vol. 28, no. 8, pp. 709-16, Aug 2004, doi: 10.1111/j.1525-1594.2004.00011.x.

[167] O. Voigt, R. J. Benkowski, and G. F. Morello, "Suction detection for the MicroMed DeBakey Left Ventricular Assist Device," (in eng), *ASAIO J,* vol. 51, no. 4, pp. 321-8, Jul-Aug 2005.

[168] Y. Wang, S. C. Koenig, Z. J. Wu, M. S. Slaughter, and G. A. Giridharan, "Sensorless Physiologic Control, Suction Prevention, and Flow Balancing Algorithm for Rotary Biventricular Assist Devices," *IEEE Transactions on Control Systems Technology,* pp. 1-13, 2018, doi: 10.1109/TCST.2017.2773518.

[169] M. C. Stevens *et al.*, "Frank-starling control of a left ventricular assist device," (in eng), *Conference proceedings : ... Annual International Conference of the IEEE Engineering in Medicine and Biology Society. IEEE Engineering in Medicine and Biology Society. Annual Conference,* vol. 2011, pp. 1335-8, 2011, doi: 10.1109/iembs.2011.6090314.

[170] G. N. R. *et al.*, "Starling-Like Flow Control of a Left Ventricular Assist Device: In Vitro Validation," *Artificial organs,* vol. 38, no. 3, pp. E46-E56, 2014, doi: doi:10.1111/aor.12221.

[171] N. Malagutti *et al.*, "Noninvasive average flow estimation for an implantable rotary blood pump: a new algorithm incorporating the role of blood viscosity," (in eng), *Artificial organs,* vol. 31, no. 1, pp. 45-52, Jan 2007, doi: 10.1111/j.1525-1594.2007.00339.x.

[172] P. J. Ayre, N. H. Lovell, and J. C. Woodard, "Non-invasive flow estimation in an implantable rotary blood pump: a study considering non-pulsatile and pulsatile flows," (in eng), *Physiological measurement,* vol. 24, no. 1, pp. 179-89, Feb 2003.

[173] E. Lim, D. M. Karantonis, J. A. Reizes, S. L. Cloherty, D. G. Mason, and N. H. Lovell, "Noninvasive average flow and differential pressure estimation for an implantable rotary blood pump using dimensional analysis," (in eng), *IEEE transactions on bio-medical engineering,* vol. 55, no. 8, pp. 2094-101, Aug 2008, doi: 10.1109/tbme.2008.919723.

[174] G. G. A. and S. Mikhail, "Physiological Control of Blood Pumps Using Intrinsic Pump Parameters: A Computer Simulation Study," *Artificial organs,* vol. 30, no. 4, pp. 301-307, 2006, doi: doi:10.1111/j.1525-1594.2006.00217.x.

[175] A. H. AlOmari, A. V. Savkin, D. M. Karantonis, E. Lim, and N. H. Lovell, "Non-invasive estimation of pulsatile flow and differential pressure in an implantable rotary blood pump for heart failure patients," (in eng), *Physiological measurement,* vol. 30, no. 4, pp. 371-86, Apr 2009, doi: 10.1088/0967-3334/30/4/003.

[176]   D. M. Karantonis, S. L. Cloherty, D. G. Mason, P. J. Ayre, and N. H. Lovell, "Noninvasive Pulsatile Flow Estimation for an Implantable Rotary Blood Pump," in *2007 29th Annual International Conference of the IEEE Engineering in Medicine and Biology Society*, 22-26 Aug. 2007 2007, pp. 1018-1021, doi: 10.1109/IEMBS.2007.4352467.

[177] M. S. Slaughter *et al.*, "Intraoperative evaluation of the HeartMate II flow estimator," (in eng), *The Journal of heart and lung transplantation : the official publication of the International Society for Heart Transplantation,* vol. 28, no. 1, pp. 39-43, Jan 2009, doi: 10.1016/j.healun.2008.10.007.

[178] K. A. Pennings *et al.*, "Pump flow estimation from pressure head and power uptake for the HeartAssist5, HeartMate II, and HeartWare VADs," (in eng), *ASAIO J,* vol. 59, no. 4, pp. 420-6, Jul-Aug 2013, doi: 10.1097/MAT.0b013e3182937a3a.

[179] A. P.J., V. S.S., T. G.D., W. P.A., and L. N.H., "Sensorless Flow and Head Estimation in the VentrAssist Rotary Blood   Pump," *Artificial organs,* vol. 24, no. 8, pp. 585-588, 2000, doi: doi:10.1046/j.1525-1594.2000.06586.x.

[180] A. Petrou, M. Kanakis, S. Boes, P. Pergantis, M. Meboldt, and M. S. Daners, "Viscosity Prediction in a Physiologically Controlled Ventricular Assist Device," *IEEE Transactions on Biomedical Engineering,* pp. 1-1, 2018, doi: 10.1109/TBME.2018.2797424.

[181] O. H. Frazier, H. A. Khalil, R. J. Benkowski, and W. E. Cohn, "Optimization of axial-pump pressure sensitivity for a continuous-flow total artificial heart," (in eng), *The Journal of heart and lung transplantation : the official publication of the International Society for Heart Transplantation,* vol. 29, no. 6, pp. 687-91, Jun 2010, doi: 10.1016/j.healun.2009.12.017.

[182] G. A. Saxton, Jr. and C. B. Andrews, "An ideal heart pump with hydrodynamic characteristics analogous to the mammalian heart," (in eng), *Transactions - American Society for Artificial Internal Organs,* vol. 6, pp. 288-91, Apr 10-11 1960.

[183] D. J. Farrar, K. Bourque, C. P. Dague, C. J. Cotter, and V. L. Poirier, "Design Features, Developmental Status, and Experimental Results With the

Heartmate III Centrifugal Left Ventricular Assist System With a Magnetically Levitated Rotor," *ASAIO Journal,* vol. 53, no. 3, pp. 310-315, 2007, doi: 10.1097/MAT.0b013e3180536694.

[184] G. A. Giridharan, M. Skliar, D. B. Olsen, and G. M. Pantalos, "Modeling and control of a brushless DC axial flow ventricular assist device," (in eng), *ASAIO journal (American Society for Artificial Internal Organs : 1992),* vol. 48, no. 3, pp. 272-89, May-Jun 2002.

[185] K. G. Soucy, S. C. Koenig, M. A. Sobieski, M. S. Slaughter, and G. A. Giridharan, "Fault detection in rotary blood pumps using motor speed response," (in eng), *ASAIO J,* vol. 59, no. 4, pp. 410-9, Jul-Aug 2013, doi: 10.1097/MAT.0b013e3182976838.

[186] Y. Wang, S. C. Koenig, M. S. Slaughter, and G. A. Giridharan, "Rotary blood pump control strategy for preventing left ventricular suction," (in eng), *ASAIO J,* vol. 61, no. 1, pp. 21-30, Jan-Feb 2015, doi: 10.1097/mat.0000000000000152.

[187] Y. Wang, S. C. Koenig, Z. Wu, M. S. Slaughter, and G. A. Giridharan, "Sensor-Based Physiologic Control Strategy for Biventricular Support with Rotary Blood Pumps," (in eng), *ASAIO J,* vol. 64, no. 3, pp. 338-350, May/Jun 2018, doi: 10.1097/mat.0000000000000671.

[188] A. P.J., V. S.S., T. G.D., W. P.A., and L. N.H., "Sensorless Flow and Head Estimation in the VentrAssist Rotary BloodPump," *Artificial organs,* vol. 24, no. 8, pp. 585-588, 2000, doi: doi:10.1046/j.1525-1594.2000.06586.x.

[189] C. Seongjin, J. R. Boston, D. Thomas, and J. F. Antaki, "Modeling and identification of an axial flow blood pump," in *Proceedings of the 1997 American Control Conference (Cat. No.97CH36041)*, 4-6 Jun 1997 1997, vol. 6, pp. 3714-3715 vol.6, doi: 10.1109/ACC.1997.609538.

[190] P. Pillay and R. Krishnan, "Modeling, simulation, and analysis of permanent-magnet motor drives. II. The brushless DC motor drive," *IEEE Transactions on Industry Applications,* vol. 25, no. 2, pp. 274-279, 1989, doi: 10.1109/28.25542.

[191] A. Petrou, D. Kuster, J. Lee, M. Meboldt, and M. Schmid Daners, "Comparison of Flow Estimators for Rotary Blood Pumps: An In Vitro and In Vivo Study," *Annals of Biomedical Engineering,* journal article vol. 46, no. 12, pp. 2123-2134, December 01 2018, doi: 10.1007/s10439-018-2106-7.

[192] E. Bullister, S. Reich, and J. Sluetz, "Physiologic Control Algorithms for Rotary Blood Pumps Using Pressure Sensor Input," *Artificial organs,* vol. 26, no. 11, pp. 931-938, 2002, doi: doi:10.1046/j.1525-1594.2002.07126.x.

[193] Y. Wu, P. Allaire, H. Wood, J. Adams, and D. Olsen, "Physiological control of a ventricle assist device," *Annals Biomed. Eng,* vol. 29 (supp 1), pp. S-2, 1.2.6, 2001.

[194] M. H. Meki, G. A. Giridharan, P. Sethu, A. S. El-Baz, and Y. Wang, "Methods, system, and computer readable media for a rotational speed-based control system for ventricular assist devices," ed: Google Patents, 2020.

[195] A. Sen *et al.*, "Mechanical circulatory assist devices: a primer for critical care and emergency physicians," *Critical Care,* vol. 20, p. 153, 06/25 2016, doi: 10.1186/s13054-016-1328-z.

[196] M. Mansouri, R. F. Salamonsen, E. Lim, R. Akmeliawati, and N. H. Lovell, "Preload-based starling-like control for rotary blood pumps: numerical comparison with pulsatility control and constant speed operation," (in eng), *PloS one,* vol. 10, no. 4, p. e0121413, 2015, doi: 10.1371/journal.pone.0121413.

[197] G. Ochsner *et al.*, "A physiological controller for turbodynamic ventricular assist devices based on a measurement of the left ventricular volume," (in eng), *Artificial organs,* vol. 38, no. 7, pp. 527-38, Jul 2014, doi: 10.1111/aor.12225.

[198] F. Moscato, M. Arabia, F. M. Colacino, P. Naiyanetr, G. A. Danieli, and H. Schima, "Left Ventricle Afterload Impedance Control by an Axial Flow Ventricular Assist Device: A Potential Tool for Ventricular Recovery," *Artificial organs,* vol. 34, no. 9, pp. 736-744, 2010, doi: doi:10.1111/j.1525-1594.2010.01066.x.

[199] A. H. AlOmari *et al.*, "Developments in control systems for rotary left ventricular assist devices for heart failure patients: a review," (in eng), *Physiological measurement,* vol. 34, no. 1, pp. R1-27, Jan 2013, doi: 10.1088/0967-3334/34/1/r1.

[200] Y. A. Wu, PE; Wood, HG; Adams, JM; Olsem, DB, " Physiological Control of a Ventricle Assist Device," *Annals of Biomedical Engineering,* vol. 29, no. Suppl 1, 2001.

[201] Y. Wu, P. Allaire, G. Tao, H. Wood, D. Olsen, and C. Tribble, "An Advanced Physiological Controller Design for a Left Ventricular Assist Device to Prevent Left Ventricular Collapse," *Artificial organs,* vol. 27, no. 10, pp. 926-930, 2003, doi: doi:10.1046/j.1525-1594.2003.00032.x.

[202] R. F. Salamonsen *et al.*, "Theoretical Foundations of a Starling-Like Controller for Rotary Blood Pumps," *Artificial organs,* vol. 36, no. 9, pp. 787-796, 2012/09/01 2012, doi: 10.1111/j.1525-1594.2012.01457.x.

[203] J. P. Pauls, M. C. Stevens, N. Bartnikowski, J. F. Fraser, S. D. Gregory, and G. Tansley, "Evaluation of Physiological Control Systems for Rotary Left Ventricular Assist Devices: An In-Vitro Study," (in eng), *Ann Biomed Eng,* vol. 44, no. 8, pp. 2377-87, Aug 2016, doi: 10.1007/s10439-016-1552-3.

[204] P. J. Ayre, S. S. Vidakovic, G. D. Tansley, P. A. Watterson, and N. H. Lovell, "Sensorless Flow and Head Estimation in the VentrAssist Rotary Blood

Pump," *Artificial Organs,* vol. 24, no. 8, pp. 585-588, 2000, doi: https://doi.org/10.1046/j.1525-1594.2000.06586.x.

[205] P. F. Davies, "Vascular cell interactions with special reference to the pathogenesis of atherosclerosis," (in eng), *Laboratory investigation; a journal of technical methods and pathology,* vol. 55, no. 1, pp. 5-24, Jul 1986.

[206] W. Elliott, D. Scott-Drechsel, and W. Tan, "In Vitro Model of Physiological and Pathological Blood Flow with Application to Investigations of Vascular Cell Remodeling," (in eng), *J Vis Exp,* no. 105, p. e53224, Nov 3 2015, doi: 10.3791/53224.

[207] N. Sakamoto, Y. Ueki, M. Oi, T. Kiuchi, and M. Sato, "Fluid shear stress suppresses ICAM-1-mediated transendothelial migration of leukocytes in coculture model," (in eng), *Biochem Biophys Res Commun,* vol. 502, no. 3, pp. 403-408, Jul 20 2018, doi: 10.1016/j.bbrc.2018.05.182.

[208] J. Robert *et al.*, "A three-dimensional engineered artery model for in vitro atherosclerosis research," (in eng), *PloS one,* vol. 8, no. 11, p. e79821, 2013, doi: 10.1371/journal.pone.0079821.

[209] N. C. A. van Engeland, A. Pollet, J. M. J. den Toonder, C. V. C. Bouten, O. Stassen, and C. M. Sahlgren, "A biomimetic microfluidic model to study signalling between endothelial and vascular smooth muscle cells under hemodynamic conditions," (in eng), *Lab on a chip,* vol. 18, no. 11, pp. 1607-1620, May 29 2018, doi: 10.1039/c8lc00286j.

[210] M. K. Ganesan *et al.*, "Three-Dimensional Coculture Model to Analyze the Cross Talk Between Endothelial and Smooth Muscle Cells," *Tissue engineering. Part C, Methods,* vol. 23, no. 1, pp. 38-49, 2017, doi: 10.1089/ten.TEC.2016.0299.

[211] C. M. Potter *et al.*, "Role of shear stress in endothelial cell morphology and expression of cyclooxygenase isoforms," (in eng), *Arteriosclerosis, thrombosis, and vascular biology,* vol. 31, no. 2, pp. 384-91, Feb 2011, doi: 10.1161/atvbaha.110.214031.

[212] C. M. F. Potter, S. Schobesberger, M. H. Lundberg, P. D. Weinberg, J. A. Mitchell, and J. Gorelik, "Shape and Compliance of Endothelial Cells after Shear Stress In Vitro or from Different Aortic Regions: Scanning Ion Conductance Microscopy Study," *PloS one,* vol. 7, no. 2, p. e31228, 2012, doi: 10.1371/journal.pone.0031228.

[213] C. L. Ives, S. G. Eskin, and L. V. McIntire, "Mechanical Effects on Endothelial Cell Morphology: In vitro Assessment," *In Vitro Cellular & Developmental Biology,* vol. 22, no. 9, pp. 500-507, 1986. [Online]. Available: http://www.jstor.org/stable/4295958.

[214] N. Inoue, S. Ramasamy, T. Fukai, R. M. Nerem, and D. G. Harrison, "Shear stress modulates expression of Cu/Zn superoxide dismutase in human aortic endothelial cells," (in eng), *Circ Res,* vol. 79, no. 1, pp. 32-7, Jul 1996.

[215] O. Traub and B. C. Berk, "Laminar shear stress: mechanisms by which endothelial cells transduce an atheroprotective force," (in eng), *Arteriosclerosis, thrombosis, and vascular biology,* vol. 18, no. 5, pp. 677-85, May 1998.

[216] T. Nishimura *et al.*, "Morphologic changes of the aortic wall due to reduced systemic pulse pressure in prolonged non pulsatile left heart bypass," (in eng), *ASAIO J,* vol. 43, no. 5, pp. M691-5, Sep-Oct 1997.

[217] B. Liu *et al.*, "Role of cyclic strain frequency in regulating the alignment of vascular smooth muscle cells in vitro," (in eng), *Biophysical journal,* vol. 94, no. 4, pp. 1497-507, Feb 15 2008, doi: 10.1529/biophysj.106.098574.

[218] B. A. Reitz, "Mechanical devices and US Food and Drug Administration (FDA) approval," (in eng), *Seminars in thoracic and cardiovascular surgery. Pediatric cardiac surgery annual,* pp. 123-7, 2006, doi: 10.1053/j.pcsu.2006.02.018.

[219] P. K. Patibandla, N. S. Rajasekaran, S. B. Shelar, G. A. Giridharan, S. H. Litovsky, and P. Sethu, "Evaluation of the effect of diminished pulsatility as seen in continuous flow ventricular assist devices on arterial endothelial cell phenotype and function," (in Eng), *The Journal of heart and lung transplantation : the official publication of the International Society for Heart Transplantation,* Mar 22 2016, doi: 10.1016/j.healun.2016.03.008.

[220] A. L. Meyer, D. Malehsa, U. Budde, C. Bara, A. Haverich, and M. Strueber, "Acquired von Willebrand syndrome in patients with a centrifugal or axial continuous flow left ventricular assist device," (in eng), *JACC Heart Fail,* vol. 2, no. 2, pp. 141-5, Apr 2014, doi: 10.1016/j.jchf.2013.10.008.

[221] S. Crow *et al.*, "Comparative analysis of von Willebrand factor profiles in pulsatile and continuous left ventricular assist device recipients," (in eng), *ASAIO J,* vol. 56, no. 5, pp. 441-5, Sep-Oct 2010, doi: 10.1097/MAT.0b013e3181e5de0a.

[222] T. A. Haglund *et al.*, "Evaluation of flow-modulation approaches in ventricular assist devices using an in-vitro endothelial cell culture model," *The Journal of Heart and Lung Transplantation,* vol. 38, no. 4, pp. 456-465, 2019, doi: 10.1016/j.healun.2018.10.007.

[223] H. A. Himburg, S. E. Dowd, and M. H. Friedman, "Frequency-dependent response of the vascular endothelium to pulsatile shear stress," (in eng), *Am J Physiol Heart Circ Physiol,* vol. 293, no. 1, pp. H645-53, Jul 2007, doi: 10.1152/ajpheart.01087.2006.

[224] J. Zhou *et al.*, "Regulation of vascular smooth muscle cell turnover by endothelial cell-secreted microRNA-126: role of shear stress," (in eng), *Circ Res,* vol. 113, no. 1, pp. 40-51, Jun 21 2013, doi: 10.1161/circresaha.113.280883.

[225] T. Pirbodaghi, S. Axiak, A. Weber, T. Gempp, and S. Vandenberghe, "Pulsatile control of rotary blood pumps: Does the modulation waveform matter?," *The Journal of thoracic and cardiovascular surgery,* vol. 144, no. 4, pp. 970-977, 2012/10/01/ 2012, doi: https://doi.org/10.1016/j.jtcvs.2012.02.015.

[226] R. Estrada *et al.*, "Endothelial Cell Culture Model for Replication of Physiological Profiles of Pressure, Flow, Stretch, and Shear Stress in Vitro," *Analytical Chemistry,* vol. 83, no. 8, pp. 3170-3177, 2011/04/15 2011, doi: 10.1021/ac2002998.

[227] P. K. Patibandla, A. J. Rogers, G. A. Giridharan, M. A. Pallero, J. E. Murphy-Ullrich, and P. Sethu, "Hyperglycemic arterial disturbed flow niche as an in vitro model of atherosclerosis," (in eng), *Anal Chem,* vol. 86, no. 21, pp. 10948-54, Nov 4 2014, doi: 10.1021/ac503294p.

[228] P. K. Patibandla, N. S. Rajasekaran, S. B. Shelar, G. A. Giridharan, S. H. Litovsky, and P. Sethu, "Evaluation of the effect of diminished pulsatility as seen in continuous flow ventricular assist devices on arterial endothelial cell phenotype and function," (in eng), *The Journal of heart and lung transplantation : the official publication of the International Society for Heart Transplantation,* vol. 35, no. 7, pp. 930-2, Jul 2016, doi: 10.1016/j.healun.2016.03.008.

[229] W. Casscells, "Migration of smooth muscle and endothelial cells. Critical events in restenosis," *Circulation,* vol. 86, no. 3, pp. 723-729, 1992, doi: doi:10.1161/01.CIR.86.3.723.

[230] P. N. Waybill and L. J. Hopkins, "Arterial and venous smooth muscle cell proliferation in response to co-culture with arterial and venous endothelial cells," (in eng), *J Vasc Interv Radiol,* vol. 10, no. 8, pp. 1051-7, Sep 1999, doi: 10.1016/s1051-0443(99)70191-0.

[231] A. R. Travis *et al.*, "Vascular pulsatility in patients with a pulsatile- or continuous-flow ventricular assist device," *The Journal of thoracic and cardiovascular surgery,* vol. 133, no. 2, pp. 517-524, 2007/02/01/ 2007, doi: https://doi.org/10.1016/j.jtcvs.2006.09.057.

[232] E. P. Efstathopoulos, G. Patatoukas, I. Pantos, O. Benekos, D. Katritsis, and N. L. Kelekis, "Wall shear stress calculation in ascending aorta using phase contrast magnetic resonance imaging. Investigating effective ways to calculate it in clinical practice," (in eng), *Physica medica : PM : an international journal devoted to the applications of physics to medicine and*

biology : official journal of the Italian Association of Biomedical Physics (AIFB), vol. 24, no. 4, pp. 175-81, Dec 2008, doi: 10.1016/j.ejmp.2008.01.004.

[233] A. R. Travis *et al.*, "Vascular pulsatility in patients with a pulsatile- or continuous-flow ventricular assist device," (in eng), *J Thorac Cardiovasc Surg,* vol. 133, no. 2, pp. 517-24, Feb 2007, doi: 10.1016/j.jtcvs.2006.09.057.

[234] T. Pirbodaghi, S. Axiak, A. Weber, T. Gempp, and S. Vandenberghe, "Pulsatile control of rotary blood pumps: Does the modulation waveform matter?," (in eng), *The Journal of thoracic and cardiovascular surgery,* vol. 144, no. 4, pp. 970-7, Oct 2012, doi: 10.1016/j.jtcvs.2012.02.015.

[235] T. Pirbodaghi, A. Weber, S. Axiak, T. Carrel, and S. Vandenberghe, "Asymmetric speed modulation of a rotary blood pump affects ventricular unloading," (in eng), *European journal of cardio-thoracic surgery : official journal of the European Association for Cardio-thoracic Surgery,* vol. 43, no. 2, pp. 383-8, Feb 2013, doi: 10.1093/ejcts/ezs299.

[236] L. G. Cox, S. Loerakker, M. C. Rutten, B. A. de Mol, and F. N. van de Vosse, "A mathematical model to evaluate control strategies for mechanical circulatory support," (in eng), *Artificial organs,* vol. 33, no. 8, pp. 593-603, Aug 2009, doi: 10.1111/j.1525-1594.2009.00755.x.

[237] G. V. Letsou *et al.*, "Improved left ventricular unloading and circulatory support with synchronized pulsatile left ventricular assistance compared with continuous-flow left ventricular assistance in an acute porcine left ventricular failure model," (in eng), *The Journal of thoracic and cardiovascular surgery,* vol. 140, no. 5, pp. 1181-8, Nov 2010, doi: 10.1016/j.jtcvs.2010.03.043.

[238] Y. Shi, P. V. Lawford, and D. R. Hose, "Numerical modeling of hemodynamics with pulsatile impeller pump support," (in eng), *Ann Biomed Eng,* vol. 38, no. 8, pp. 2621-34, Aug 2010, doi: 10.1007/s10439-010-0001-y.

[239] G. B. Bearnson, D. B. Olsen, P. S. Khanwilkar, J. W. Long, P. E. Allaire, and E. H. Maslen, "Pulsatile operation of a centrifugal ventricular assist device with magnetic bearings," (in eng), *ASAIO J,* vol. 42, no. 5, pp. M620-4, Sep-Oct 1996.

[240] K. X. Qian, "Pulsatile impeller heart: a viable alternative to a problematic diaphragm heart," (in eng), *Medical engineering & physics,* vol. 18, no. 1, pp. 57-66, Jan 1996.

[241] C. E. Tabit *et al.*, "Elevated Angiopoietin-2 Level in Patients With Continuous-Flow Left Ventricular Assist Devices Leads to Altered Angiogenesis and Is Associated

With Higher Nonsurgical BleedingClinical Perspective," *Circulation,* vol. 134, no. 2, pp. 141-152, 2016, doi: 10.1161/circulationaha.115.019692.

[242] S. R. Patel, S. Vukelic, and U. P. Jorde, "Bleeding in continuous flow left ventricular assist device recipients: an acquired vasculopathy?," *J Thorac Dis,* vol. 8, no. 10, pp. E1321-E1327, 09/19/received

09/23/accepted 2016, doi: 10.21037/jtd.2016.10.81.

[243] L. K. Truby and V. K. Topkara, "Angiopoietin-2: marker or mediator of angiogenesis in continuous-flow left ventricular assist device patients?," *J Thorac Dis,* vol. 8, no. 11, pp. 3042-3045, 08/19/received

08/26/accepted 2016, doi: 10.21037/jtd.2016.11.04.

[244] W. Jeske, D. Syed, V. Escalante, E. Coglianese, J. Schwartz, and J. M. Walenga, "Inflammatory Cytokines Are Upregulated in Patients with Implanted Ventricular Assist Devices," *Blood,* vol. 124, no. 21, pp. 5049-5049, 2014.

[245] Y. Chen *et al.,* "Interleukin-6 involvement in brain arteriovenous malformations," (in eng), *Annals of neurology,* vol. 59, no. 1, pp. 72-80, Jan 2006, doi: 10.1002/ana.20697.

[246] A. A. Ardelt, L. D. McCullough, K. S. Korach, M. M. Wang, D. H. Munzenmaier, and P. D. Hurn, "Estradiol regulates angiopoietin-1 mRNA expression through estrogen receptor-alpha in a rodent experimental stroke model," (in eng), *Stroke,* vol. 36, no. 2, pp. 337-41, Feb 2005, doi: 10.1161/01.str.0000153795.38388.72.

[247] A. Li, S. Dubey, M. L. Varney, B. J. Dave, and R. K. Singh, "IL-8 directly enhanced endothelial cell survival, proliferation, and matrix metalloproteinases production and regulated angiogenesis," (in eng), *Journal of immunology (Baltimore, Md. : 1950),* vol. 170, no. 6, pp. 3369-76, Mar 15 2003.

[248] J. S. Yao *et al.,* "Interleukin-6 upregulates expression of KDR and stimulates proliferation of human cerebrovascular smooth muscle cells," (in eng), *Journal of cerebral blood flow and metabolism : official journal of the International Society of Cerebral Blood Flow and Metabolism,* vol. 27, no. 3, pp. 510-20, Mar 2007, doi: 10.1038/sj.jcbfm.9600365.

[249] G. Chen *et al.,* "Macrophage migration inhibitory factor reduces apoptosis in cerebral arteriovenous malformations," (in eng), *Neuroscience letters,* vol. 508, no. 2, pp. 84-8, Feb 6 2012, doi: 10.1016/j.neulet.2011.12.024.

[250] H. Noels, J. Bernhagen, and C. Weber, "Macrophage migration inhibitory factor: a noncanonical chemokine important in atherosclerosis," (in eng),

Trends in cardiovascular medicine, vol. 19, no. 3, pp. 76-86, Apr 2009, doi: 10.1016/j.tcm.2009.05.002.

[251] D. R. Senger, S. J. Galli, A. M. Dvorak, C. A. Perruzzi, V. S. Harvey, and H. F. Dvorak, "Tumor cells secrete a vascular permeability factor that promotes accumulation of ascites fluid," (in eng), *Science (New York, N.Y.),* vol. 219, no. 4587, pp. 983-5, Feb 25 1983.

[252] T. Hashimoto *et al.*, "Abnormal expression of matrix metalloproteinases and tissue inhibitors of metalloproteinases in brain arteriovenous malformations," (in eng), *Stroke,* vol. 34, no. 4, pp. 925-31, Apr 2003, doi: 10.1161/01.str.0000061888.71524.df.

[253] T. A. Haglund *et al.*, "Evaluation of Flow Modulation Approaches In Ventricular Assist Devices (VADs) Using an In-Vitro Endothelial Cell Culture Model (ECCM)," *The Journal of Heart and Lung Transplantation,* 2018.

[254] D. Scott, Y. Tan, R. Shandas, K. R. Stenmark, and W. Tan, "High pulsatility flow stimulates smooth muscle cell hypertrophy and contractile protein expression," (in eng), *American journal of physiology. Lung cellular and molecular physiology,* vol. 304, no. 1, pp. L70-81, Jan 1 2013, doi: 10.1152/ajplung.00342.2012.

[255] R. Gilsbach *et al.*, "Dynamic DNA methylation orchestrates cardiomyocyte development, maturation and disease," *Nature Communications,* vol. 5, no. 1, p. 5288, 2014/10/22 2014, doi: 10.1038/ncomms6288.

[256] R. E. Ahmed, T. Anzai, N. Chanthra, and H. Uosaki, "A Brief Review of Current Maturation Methods for Human Induced Pluripotent Stem Cells-Derived Cardiomyocytes," (in English), *Frontiers in Cell and Developmental Biology,* Mini Review vol. 8, no. 178, 2020-March-19 2020, doi: 10.3389/fcell.2020.00178.

[257] M. Brandenburger *et al.*, "Organotypic slice culture from human adult ventricular myocardium," *Cardiovascular Research,* vol. 93, no. 1, pp. 50-59, 2011, doi: 10.1093/cvr/cvr259.

[258] S. A. Watson *et al.*, "Biomimetic electromechanical stimulation to maintain adult myocardial slices in vitro," *Nature Communications,* vol. 10, no. 1, p. 2168, 2019/05/15 2019, doi: 10.1038/s41467-019-10175-3.

[259] C. Kang *et al.*, "Human Organotypic Cultured Cardiac Slices: New Platform For High Throughput Preclinical Human Trials," *Scientific Reports,* vol. 6, no. 1, p. 28798, 2016/06/30 2016, doi: 10.1038/srep28798.

[260] J. E. Herrmann, J. Heale, M. Bieraugel, M. Ramos, R. L. Fisher, and A. E. M. Vickers, "Isoproterenol effects evaluated in heart slices of human and rat in comparison to rat heart in vivo," *Toxicology and Applied Pharmacology,* vol. 274, no. 2, pp. 302-312, 2014, doi: 10.1016/j.taap.2013.11.011.

[261] C. Fischer *et al.*, "Long-term functional and structural preservation of precision-cut human myocardium under continuous electromechanical stimulation in vitro," *Nature Communications,* vol. 10, no. 1, p. 117, 2019/01/10 2019, doi: 10.1038/s41467-018-08003-1.

[262] F. G. Pitoulis *et al.*, "Remodelling of adult cardiac tissue subjected to physiological and pathological mechanical load in vitro," *Cardiovascular Research,* 2021, doi: 10.1093/cvr/cvab084.

[263] I. Klein and K. Ojamaa, "Thyroid Hormone and the Cardiovascular System," *New England Journal of Medicine,* vol. 344, no. 7, pp. 501-509, 2001, doi: 10.1056/nejm200102153440707.

[264] X. Yang *et al.*, "Tri-iodo-l-thyronine promotes the maturation of human cardiomyocytes-derived from induced pluripotent stem cells," *Journal of molecular and cellular cardiology,* vol. 72, pp. 296-304, 2014.

[265] S. S. Parikh *et al.*, "Thyroid and Glucocorticoid Hormones Promote Functional T-Tubule Development in Human-Induced Pluripotent Stem Cell–Derived Cardiomyocytes," *Circulation Research,* vol. 121, no. 12, pp. 1323-1330, 2017, doi: doi:10.1161/CIRCRESAHA.117.311920.

[266] L. Sala *et al.*, "MUSCLEMOTION: A Versatile Open Software Tool to Quantify Cardiomyocyte and Cardiac Muscle Contraction In Vitro and In Vivo," (in eng), *Circ Res,* vol. 122, no. 3, pp. e5-e16, Feb 2 2018, doi: 10.1161/circresaha.117.312067.

[267] S. A. Watson *et al.*, "Biomimetic electromechanical stimulation to maintain adult myocardial slices in vitro," *Nature Communications,* vol. 10, no. 1, 2019, doi: 10.1038/s41467-019-10175-3.

[268] P. P. de Tombe and H. E. D. J. ter Keurs, "The velocity of cardiac sarcomere shortening: mechanisms and implications," (in eng), *J Muscle Res Cell Motil,* vol. 33, no. 6, pp. 431-437, 2012, doi: 10.1007/s10974-012-9310-0.

[269] E. H. Sonnenblick, "Force-velocity relations in mammalian heart muscle," *American Journal of Physiology-Legacy Content,* vol. 202, no. 5, pp. 931-939, 1962, doi: 10.1152/ajplegacy.1962.202.5.931.

[270] T. Yingchoncharoen, S. Agarwal, Z. B. Popović, and T. H. Marwick, "Normal Ranges of Left Ventricular Strain: A Meta-Analysis," *Journal of the American Society of Echocardiography,* vol. 26, no. 2, pp. 185-191, 2013/02/01/ 2013, doi: https://doi.org/10.1016/j.echo.2012.10.008.

[271] Q. Au - Ou *et al.*, "Slicing and Culturing Pig Hearts under Physiological Conditions," *JoVE,* no. 157, p. e60913, 2020/03/20/ 2020, doi: doi:10.3791/60913.

[272] R. Fukuda *et al.*, "Stimulation of glycolysis promotes cardiomyocyte proliferation after injury in adult zebrafish," (in eng), *EMBO Rep,* vol. 21, no. 8, pp. e49752-e49752, 2020, doi: 10.15252/embr.201949752.

[273] J. Sadoshima, L. Jahn, T. Takahashi, T. J. Kulik, and S. Izumo, "Molecular characterization of the stretch-induced adaptation of cultured cardiac cells. An in vitro model of load-induced cardiac hypertrophy," (in eng), *J Biol Chem,* vol. 267, no. 15, pp. 10551-60, May 25 1992.

[274] C. Ruwhof and A. van der Laarse, "Mechanical stress-induced cardiac hypertrophy: mechanisms and signal transduction pathways," (in eng), *Cardiovasc Res,* vol. 47, no. 1, pp. 23-37, Jul 2000, doi: 10.1016/s0008-6363(00)00076-6.

[275] A. J. Shanker, K. Yamada, K. G. Green, K. A. Yamada, and J. E. Saffitz, "Matrix-protein-specific regulation of Cx43 expression in cardiac myocytes subjected to mechanical load," (in eng), *Circ Res,* vol. 96, no. 5, pp. 558-66, Mar 18 2005, doi: 10.1161/01.RES.0000158964.42008.a2.

[276] A. Salameh *et al.*, "Cyclic Mechanical Stretch Induces Cardiomyocyte Orientation and Polarization of the Gap Junction Protein Connexin43," *Circulation Research,* vol. 106, no. 10, pp. 1592-1602, 2010, doi: doi:10.1161/CIRCRESAHA.109.214429.

[277] W. Roell *et al.*, "Overexpression of Cx43 in cells of the myocardial scar: Correction of post-infarct arrhythmias through heterotypic cell-cell coupling," *Scientific Reports,* vol. 8, no. 1, p. 7145, 2018/05/08 2018, doi: 10.1038/s41598-018-25147-8.

[278] H. Abdeltawab *et al.*, "Artificial Intelligence Based Framework to Quantify the Cardiomyocyte Structural Integrity in Heart Slices," *Cardiovascular Engineering and Technology,* 2021/08/16 2021, doi: 10.1007/s13239-021-00571-6.

[279] M. Eghbali *et al.*, "Localization of types I, III and IV collagen mRNAs in rat heart cells by in situ hybridization," (in eng), *J Mol Cell Cardiol,* vol. 21, no. 1, pp. 103-13, Jan 1989, doi: 10.1016/0022-2828(89)91498-3.

[280] G. Nicolini, F. Forini, C. Kusmic, L. Pitto, L. Mariani, and G. Iervasi, "Early and Short-term Triiodothyronine Supplementation Prevents Adverse Postischemic Cardiac Remodeling: Role of Transforming Growth Factor0²1 and Antifibrotic miRNA Signaling," *Molecular Medicine,* vol. 21, pp. 900-911, 2016.

[281] F. G. Pitoulis and C. M. Terracciano, "Heart Plasticity in Response to Pressure- and Volume-Overload: A Review of Findings in Compensated and Decompensated Phenotypes," (in English), *Frontiers in Physiology,* Review vol. 11, no. 92, 2020-February-13 2020, doi: 10.3389/fphys.2020.00092.

[282] G. J. Scuderi and J. Butcher, "Naturally Engineered Maturation of Cardiomyocytes," (in English), *Frontiers in Cell and Developmental Biology,* Review vol. 5, no. 50, 2017-May-05 2017, doi: 10.3389/fcell.2017.00050.

[283] J.-L. Ruan *et al.*, "Mechanical Stress Conditioning and Electrical Stimulation Promote Contractility and Force Maturation of Induced Pluripotent Stem Cell-Derived Human Cardiac Tissue," *Circulation,* vol. 134, no. 20, pp. 1557-1567, 2016, doi: doi:10.1161/CIRCULATIONAHA.114.014998.

[284] M. Govoni, C. Muscari, C. Guarnieri, and E. Giordano, "Mechanostimulation Protocols for Cardiac Tissue Engineering," *BioMed Research International,* vol. 2013, p. 918640, 2013/07/08 2013, doi: 10.1155/2013/918640.

[285] S. Mohr-Kahaly, G. Kahaly, and J. Meyer, "[Cardiovascular effects of thyroid hormones]," (in ger), *Z Kardiol,* vol. 85 Suppl 6, pp. 219-31, 1996. Kardiovaskuläre Wirkungen von Schilddrüsenhormonen.

[286] Q. Xue, A. J. Patterson, D. Xiao, and L. Zhang, "Glucocorticoid modulates angiotensin II receptor expression patterns and protects the heart from ischemia and reperfusion injury," (in eng), *PLoS One,* vol. 9, no. 9, p. e106827, 2014, doi: 10.1371/journal.pone.0106827.

[287] M. Wester, A. Heller, M. Gruber, L. S. Maier, C. Schach, and S. Wagner, "Glucocorticoid stimulation increases cardiac contractility by SGK1-dependent SOCE-activation in rat cardiac myocytes," *PLOS ONE,* vol. 14, no. 9, p. e0222341, 2019, doi: 10.1371/journal.pone.0222341.

[288] K. Itagaki *et al.*, "Dexamethasone stimulates store-operated calcium entry and protein degradation in cultured L6 myotubes through a phospholipase A2-dependent mechanism," *American Journal of Physiology-Cell Physiology,* vol. 298, no. 5, pp. C1127-C1139, 2010, doi: 10.1152/ajpcell.00309.2009.

[289] S. S. Parikh *et al.*, "Thyroid and Glucocorticoid Hormones Promote Functional T-Tubule Development in Human-Induced Pluripotent Stem Cell-Derived Cardiomyocytes," (in eng), *Circ Res,* vol. 121, no. 12, pp. 1323-1330, Dec 8 2017, doi: 10.1161/circresaha.117.311920.

[290] N. Nam-Trung, W. Steven, and S. Seyed Ali Mousavi, *Fundamentals and Applications of Microfluidics, Third Edition*. Artech, 2019, p. 1.

CURRICULUM VITAE

Name:	Moustafa Meki
DEPARTMENT:	Bioengineering Department, University of Louisville
ADDRESS:	2210 S Brook St, Louisville, KY 40208 – Shumaker Research Building, Room 359
DOB:	Behiera, Egypt – August 17, 1991

January 2017-November 2021 (Expected)	PhD, Bioengineering (Biomedical Devices concentration)
	University of Louisville, KY GPA: 4.0
	Advisor: Dr. G A Giridharan – Bioengineering.
	Dissertation title: "Development and Applications of In-vitro and In-silico Models of the Cardiovascular System for The Development of Continuous Flow Left Ventricular Assist Devices"
June 2014	B.Sc. , Electromechanical Engineering
	Alexandria University, Egypt GPA: 3.8

EXPERIENCE

- **Research Assistant** Institute of Molecular cardiology (IMC), University of Louisville, KY,

  (June 2019 – Present)

  Working in Dr, Tamer Mohamed's Lab. As lead researcher, developed an ultrathin biomimetic cardiac slice culture system that provides an organotypic platform for subacute and long-term drug testing under physiological conditions with both electrical and mechanical stimulation.

- **Research Assistant** Cardiovascular Innovation Institute (CII), University of Louisville, KY,

  (April 2017 – Present)

  Lead researcher on two different projects in Dr. Giridharan's Biomedical Devices lab.

a- Applications using an endothelial cell- smooth muscle cell coculture model of the normal vasculature that can mimic physiological and pathological stretch, shear stress and arterial pressures.

b- Developed and tested in-silico a novel control algorithm that enables mechanical heart pumps (LVADs) to safely adjust their flow based on tissue and hold a US patent for the developed technology. **Graduate Teaching Assistant,**

- (May 2018- August 2018) *University of Louisville*
  - BE611 Cardiovascular Mechanics. (Instructor: Prof. G. Giridharan)
    - Performed grading and held office hours. Created new assignments and created and presented 4 guest lectures.
- (January 2018-May 2018) *University of Louisville*
  - BE310 Bio transport phenomenon. (Instructor: Prof. G. Giridharan)
    - Performed grading and held office hours. presented 2 guest lectures.
- (March 2016- December 2016) , *Alexandria University, Egypt*
  - EME206 Fluid Mechanics I
  - EME416 Turbo Machinery
    - Assisted in teaching 2 different courses, gave tutorials and labs, held office hours and did grading.

INTELLUCTUAL PROPERTY

1. **MH Meki**, GA Giridharan, P Sethu, AS El-Baz, Y Wang. Methods, system, and computer readable media for a rotational speed-based control system for ventricular assist devices. 2020/5/14, *US 16678897*

2. **M. Meki**, GA Giridharan, Tamer Mohamed. Efficient Biomimetic Human Heart Slice Culture System. Inventorship Disclosure ULRF#20049, University of Louisville, Louisville, KY. (submitted as provisional patent)

3. GA Giridharan, **M. Meki**, F. Kehdy, L.M. Fernandez, L Workman, H.W. Shoff. Cap locking mechanism to minimize unauthorized utilization of peripherally inserted central catheter. US 62/699,965 (provisional).

4. **M. Meki**, GA Giridharan, F Kehdy. Locking mechanism to minimize disconnection of medical connectors. ULRF#19024, University of Louisville, Louisville, KY.

Publications[4]:

---

[4] * First author, equal contribution

1. **M. Meki**, Y. Wang, P. Sethu, M. Ghazal, A. El-Baz and G. Giridharan, A Sensorless Rotational Speed-Based Control System for Continuous Flow Left Ventricular Assist Devices, in *IEEE Transactions on Biomedical Engineering*, vol. 67, no. 4, pp. 1050-1060, April 2020

2. Liang L, **Meki M***, Wang W, Sethu P, El-Baz A, Giridharan GA and Wang Y. A suction index based control system for rotary blood pumps. *Biomedical Signal Processing and Control*. 2020;62:102057.

3. Miller JM, **Meki MH***, Ou Q, George SA, Gams A, Abouleisa RRE, Tang X-L, Ahern BM, Giridharan GA, El-Baz A, Hill BG, Satin J, Conklin DJ, Moslehi J, Bolli R, Ribeiro AJS, Efimov IR and Mohamed TMA. Heart slice culture system reliably demonstrates clinical drug-related cardiotoxicity. *Toxicology and Applied Pharmacology*. 2020;406:115213.

4. (Submitted): **M. Meki**, A. El-Baz, P Sethu, and G Giridharan. Effects of pulsatility on arterial endothelial and smooth muscle cells. *Cells Tissues and Organs*

5. **Meki MH,** Miller JM and Mohamed TMA. Heart Slices to Model Cardiac Physiology. Frontiers in Pharmacology. 2021;12:23

6. Ou, Q., Abouleisa, R. R. E., Tang, X. L., Juhardeen, H. R., **Meki, M. H**., Miller, J. M., Giridharan, G., El-Baz, A., Bolli, R., Mohamed, T. M. A. Slicing and Culturing Pig Hearts under Physiological Conditions. *J. Vis. Exp.* (157), e60913, doi:10.3791/60913 (2020).

7. Hisham Abdeltawab, Fahmi Khalifa, Kamal Hammouda, Jessica M. Miller, **Moustafa M. Meki**, Qinghui Ou, Ayman El-Baz , and Tamer M. A. Mohamed Artificial Intelligence Based Framework to Quantify the Cardiomyocyte Structural Integrity in Heart Slices. Cardiovasc Eng Tech (2021).

8. **M. Meki**, Y. Wang, P. Sethu, M. Ghazal, A. El-Baz and G. Giridharan, "A Sensorless non-linear Control algorithm for Continuous Flow Right Ventricular Assist Devices," *2018 IEEE International Symposium on Signal Processing and Information Technology (ISSPIT)*, 2018, pp. 147-152, doi: 10.1109/ISSPIT.2018.8642730

Conference Presentations:

1. (*Podium Presentation*) **Moustafa Meki**, Jessica Miller, Qinghui Ou, Ahmad Gebreil, AbouBakr Salama, Xian-Liang Tang, Riham R E Abouleisa, Ayman S El-Baz, Guruprasad Giridharan, and Tamer M A Mohamed, "Emulating the Cardiac Mechanical and Humoral Cues to Prolong Human Heart Slice Culture" AHA Scientific Sessions, Boston, MA, 2021

2. (*Podium Presentation*) **M. Meki**, Palaniappan Sethu Ayman El-Baz, and G.A Giridharan. An In-vitro Human Endothelial Cell-Smooth Muscle Cell Co-Culture Model to Study The Effects of Pulsatility*; 2019 June; San Francisco, CA.*

3. *(Podium presentation)* **M. Meki** et al. A Sensorless non-linear Control algorithm for Continuous Flow Right Ventricular Assist Devices. *IEEE International Symposium on Information Technology and Signal Processing*

Conference Abstracts:

1. **M. Meki** et al. Development of an Efficient Biomimetic Human Heart Slice Culture System, *Biomedical Engineering Society Meeting; 2019 October; Philadelphia, PA.*

2. **M. Meki** et al. A Physiologic Cancer-Endothelial Cell Co-culture Model for High Throughput Drug Testing, *Biomedical Engineering Society Meeting; 2019 October; Philadelphia, PA.*

3. G.A. Giridharan and **M Meki**. A Long-term Cavo-pulmonary Assist Device to Reverse the Fontan: In-silico and In-Vitro Studies. *American Society of Artificial Internal Organs Meeting; 2019 June; San Francisco, CA.*

4. Y Wang and **M. Meki**. Rotary Blood Pump Control Strategy for Physiologic Perfusion, Suction Prevention, and Augmentation of Vascular Pulsatility. *American Society of Artificial Internal Organs Meeting; 2019 June; San Francisco, CA.*

5. "A Sensorless Rotational Speed-based Control System for Continuous Flow Left Ventricular Assist Devices, *Biomedical Engineering Society Meeting; 2018 October; Atlanta, GA.*

PEER REVIEWER:

- Peer reviewer for IEEE Journal of Biomedical and Health Informatics, 2021.
- Served as a peer reviewer on the IEE American Control Conference (ACC), Denver, CO,2020

HONORS AND AWARDS

2019   Doctoral Student Inventorship Award, Speed School of Engineering, University of Louisville

2019	3-minute thesis finalist, Research! Louisville, University of Louisville
2019	Graduate Student Council Travel Funding Award
2018 - 2019	University Fellow, University of Louisville
2010-2014	Excellence Award for the grade of distinction, Alexandria University

PROFESSIONAL MEMBERSHIPS

2020 -	Member, American Heart Association, AHA
2018 -	Member, American Society of Artificial Internal Organs, ASAIO
2018-	Member, Biomedical Engineering Society, BMES
2010-	Member, Institute of Electrical and Electronics Engineers, IEEE

REFRENCES: Available upon request